Reconfigurable Pixel Antennas for Communications

Author:
Daniel Rodrigo

Thesis Advisor:
Prof. Lluís Jofre

A thesis submitted in partial fulfilment of the requirements
for the degree of DOCTOR OF PHILOSOPHY
at Universitat Politècnica de Catalunya (UPC)

PhD Program: Signal Theory and Communications

April 2013

Daniel Rodrigo
Reconfigurable Pixel Antennas for Communications

	Curs acadèmic: 2012/2013

Acta de qualificació de tesi doctoral

Nom i cognoms
DANIEL RODRIGO LOPEZ

Programa de doctorat
TEORIA DEL SENYAL I COMUNICACIONS

Unitat estructural responsable del programa
ANTENNALAB – TEORIA DEL SENYAL I COMUNICACIONS

Resolució del Tribunal

Reunit el Tribunal designat a l'efecte, el doctorand / la doctoranda exposa el tema de la seva tesi doctoral titulada

RECONFIGURABLE PIXEL ANTENNAS FOR COMMUNICATIONS.

Acabada la lectura i després de donar resposta a les qüestions formulades pels membres titulars del tribunal, aquest atorga la qualificació:

☐ APTA/E   ☐ NO APTA/E

(Nom, cognoms i signatura) President/a	(Nom, cognoms i signatura) Secretari/ària
(Nom, cognoms i signatura) Vocal	(Nom, cognoms i signatura) Vocal

(tercer vocal) (Nom, cognoms i signatura)

Vocal

_____, _____ d'/de _____ de _____

El resultat de l'escrutini dels vots emesos pels membres titulars del tribunal, efectuat per l'Escola de Doctorat, a instància de la Comissió de Doctorat de la UPC, atorga la MENCIÓ CUM LAUDE:

☐ SÍ   ☐ NO

(Nom, cognoms i signatura) Presidenta de la Comissió de Doctorat	(Nom, cognoms i signatura) Secretària de la Comissió de Doctorat

Barcelona, _____ d'/de _____ de _____

ABSTRACT

The explosive growth of wireless communications has brought new requirements in terms of compactness, mobility and multi-functionality that pushes antenna research. In this context, reconfigurable antennas have gained a lot of attention due to their ability to adjust dynamically their frequency and radiation properties, providing multiple functionalities and being able to adapt themselves to a changing environment.

A pixel antenna is a particular type of reconfigurable antenna composed of a grid of metallic patches interconnected by RF-switches which can dynamically reshape its active surface. This capability provides pixel antennas with a reconfiguration level much higher than in other reconfigurable architectures. Despite the outstanding reconfiguration capabilities of pixel antennas, there are important practical issues related to the performance-complexity balance that must be addressed before they can be implemented in commercial systems. This doctoral work focuses on the minimization of the pixel antenna complexity while maximizing its reconfiguration capabilities, contributing to the development of pixel antennas from a conceptual structure towards a practical reconfigurable antenna architecture.

First, the conceptualization of novel pixel geometries is addressed. It is shown that antenna complexity can be significantly reduced by using multiple-sized pixels. This multi-size technique allows to design pixel antennas with a number of switches one order of magnitude lower than in common pixel structures, while preserving high multi-parameter reconfigurability. A new conceptual architecture where the pixel surface acts as a parasitic layer is also proposed. The parasitic nature of the pixel layer leads to important advantages regarding the switch biasing and integration possibilities.

Secondly, new pixel reconfiguration technologies are explored. After investigating the capabilities of semiconductors and RF-MEMS switches, microfluidic technology is proposed as a new technology to create and remove liquid metal pixels rather than interconnecting them.

Thirdly, the full multi-parameter reconfiguration capabilities of pixel antennas is explored, which contrasts with the partial explorations available in the literature. The maximum achievable reconfiguration ranges (frequency range, beam-steering angular range and polarization modes) as well as the linkage between the different parameter under reconfiguration are studied.

Finally, the performance of reconfigurable antennas in beam-steering applications is analyzed. Figures-of-merit are derived to quantify radiation pattern reconfigurability, enabling the evaluation of the performance of reconfigurable antennas, pixel antennas and reconfiguration algorithms.

CONTENTS

INTRODUCTION

THIS introduction provides an initial description of the concept of antenna reconfiguration. An historical view of the evolution of reconfigurable antennas is presented with particular emphasis on the current trends and challenges. Based on the foregoing, the main objectives of this doctoral thesis are detailed and a description of the structure of this document is provided.

1.1 RECONFIGURABLE ANTENNA CONCEPT

1.1.1 Definition

An antenna is a part of a transmitting or receiving system which is designed to radiate or to receive electromagnetic waves (IEEE [1]). Antennas are generally considered radiating or receiving elements with time invariant properties. However, in the last decade there has been a growing interest in antennas with tunable characteristics that can adapt themselves to a changing scenario or to different operating requirements. These antennas are grouped under the term reconfigurable antenna (RA) [2,3].

The concept of reconfigurable antennas has been evolving over the years and a standard definition has not been yet established. Currently, the most widely accepted definition of reconfigurable antenna is the following. A reconfigurable antenna is an antenna that incorporates an internal mechanism to redistribute the RF-currents over its surface and produce reversible modifications over the antenna impedance and/or radiation properties. Under this definition it is required that the reconfiguration mechanism interacts directly with the antenna radiation mechanism. Therefore, tunable antennas based on external matching circuits and switched/phase-shifted antenna arrays are excluded from this definition.

A classical example of a reconfigurable antenna is presented in Fig. 1.1. It shows a reconfigurable dipole that uses two RF-switches to adjust its length and tune the operation frequency between a low-frequency mode (switches ON) and a high-frequency mode (switches OFF).

(a) Switched antenna   (b) Configuration #1   (c) Configuration #2
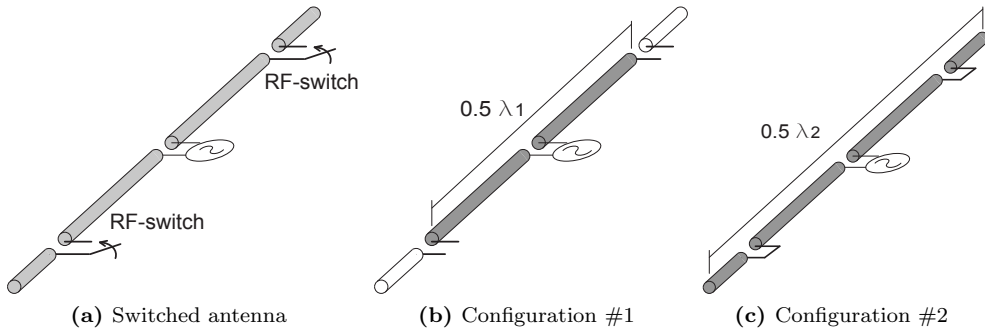
Fig. 1.1: Frequency reconfigurable dipole antenna with two configurations operating at two different frequencies.

(a) Frequency   (b) Radiation pattern

(c) Polarization
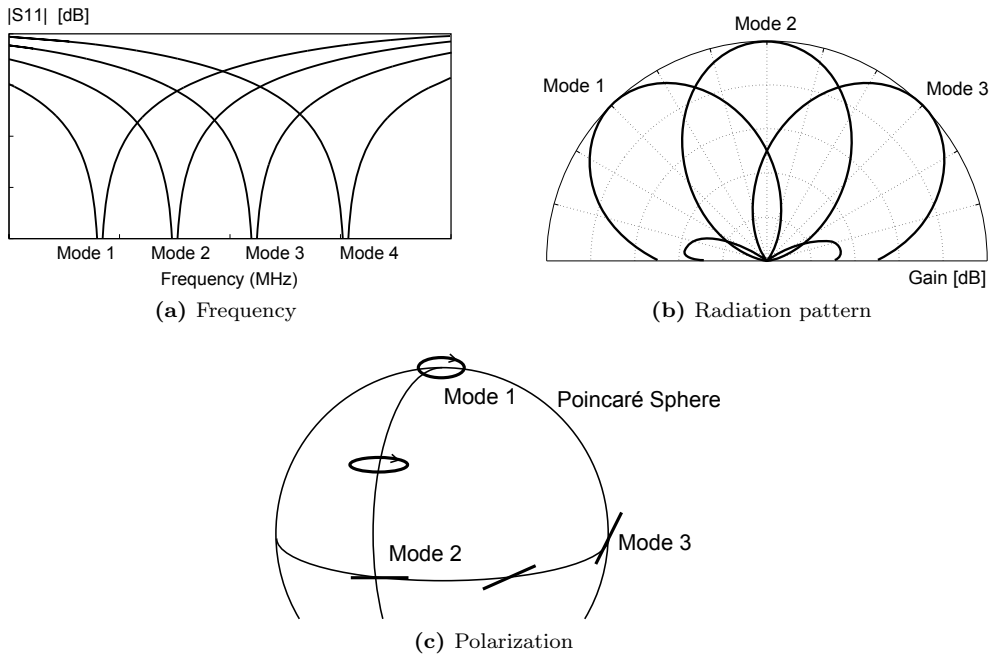
Fig. 1.2: Conceptual representation of reconfiguration capabilities provided by the different types of reconfigurable antennas.

1.1.2   Types of antenna reconfiguration

Reconfigurable antennas can be classified according to the antenna parameter that is intentionally tuned. Following this criterion RAs are divided in three groups: frequency, radiation pattern and polarization reconfigurable antennas. A descriptive view of these concepts is represented in Fig. 1.2.

Frequency reconfigurable antennas can adjust dynamically their frequency of operation. They are particularly useful in situations where several communications systems converge because the multiple antennas required can be replaced by a single RA. They are also an attractive solution to multiband applications where the existing wideband antenna can be replaced by a narrowband frequency RA with the consequential benefits in terms of size and interference filtering. Frequency reconfiguration is generally achieved by modifying physically or electrically the antenna dimensions using RF-switches, impedance loading or tunable materials.

Radiation pattern reconfigurability is based on the intentional modification of the spherical distribution of radiation. Beamsteering is the most extended application and consists in steering the direction of maximum radiation to maximize the antenna gain in a link with mobile devices. Pattern reconfigurable antennas are usually designed using movable/rotatable structures or including switchable and reactively-loaded parasitic elements.

Polarization reconfigurable antennas are capable of switching between different polarization modes. The capability of switching between horizontal, vertical and circular polarizations can be used to reduce polarization mismatch losses in portable devices. Polarization reconfigurability can be provided by applying symmetry transformations to the antenna shape or by changing the balance between the different modes of a multi-mode structure.

A more comprehensive description of reconfigurable antenna applications and a detailed analysis of the existing reconfiguration techniques and technologies is included in chapter 2.

1.2 RECONFIGURABLE ANTENNAS: HISTORY, TRENDS AND CHALLENGES

1.2.1 Historical perspective

A thorough analysis of antenna history reveals that the concept of antenna reconfigurability appears very early in the context of radio communications which dates back to 1893-1901 with the first wireless transmissions disputed by Tesla and Marconi. On the early years of radio broadcasting the main motivation for antenna reconfigurability was the requirement of antennas that could cover a large frequency range without degrading its performance. This was the very first form of frequency reconfigurability. One illustrative example of the initial works towards frequency reconfiguration corresponds to a patent by A.N. Goldsmith in 1926 where an antenna is tuned by using a variable inductive loading [4]. A second example of a frequency tunable antenna is found in a patent by E. Werndl in 1942 where it is proposed to adjust the length of dipole antenna by using a liquid metal [5].

Some years after the first frequency tunable antennas, the firsts designs of antennas with steerable radiation pattern appeared. The development of antennas with radiation pattern agility took place towards the 1940s, basically driven by World War II when beam-scanning antennas played a key role in radar applications [6]. The main techniques to achieve beam scanning were movable and multi-feed reflectors and

phased-arrays. However, one can argue that, strictly speaking, these designs are not reconfigurable antennas since there is not a clear interaction between the reconfiguration and the radiation mechanisms. One of the firsts radiation pattern reconfigurable antennas producing a clear interaction with the radiating mechanism was published by W. Rotman in 1959 [7]. It consisted on a radiating waveguide with a mechanically tuned leaky mode that allowed the antenna to perform beam-scanning.

1.2.2 Intensification of research in reconfigurable antennas

As we have seen, the concept of antenna reconfigurability can be traced back to the first half of the twentieth century, however it has been in the last decade when reconfigurable antennas have attracted a major interest from the wireless community. During these years drastic changes have reshaped wireless communications landscape and it is this new scenario that has boosted research on reconfigurable antennas.

The most significant impulse to reconfigurable antennas has been undoubtedly the explosive growth of wireless personal communications devices that started in the 1990s with the deployment of GSM cellular networks. Personal wireless devices brought new requirements in terms of compactness and mobility; properties that carried greater weight than in previous military applications and broadcasting systems. Also, during the subsequent years, additional wireless systems where developed to cover different needs. Wireless systems such as IEEE-802.11 WLAN, UMTS, *Bluetooth* and GPS were rapidly adopted and wireless devices became multifunctional, meaning that a single electronic device was able to operate in multiple communications. Additionally, the fast spread of personal wireless systems pushed an intense competition for wireless devices with superior performance in terms of transmission data rates, coverage and reliability.

In this context where compactness, multi-functionality and superior performance are the main requirements, reconfigurable antennas stand out as a promising approach for future wireless systems. On one hand, multi-functionality is generally provided by using multiple antennas, but due to the compactness requirements it is becoming more and more difficult to fit all the necessary antennas in the available space. Instead, the multiple required antennas could be replaced by a single reconfigurable antenna that could be tuned for each required functionality. On the other hand, reconfigurable antennas can clearly contribute to improve the system performance by dynamically adjusting their radiation pattern and polarization to maximize data rates, coverage and reliability.

The growing interest of the research community in reconfigurable antennas is evidenced by the rapidly increasing number of publications on the topic. In Fig. 1.3 it is represented the yearly evolution of the number of publications and patents containing the words *reconfigurable antennas* in the title. It is observed that it is in the years 1999-2000 when the development of reconfigurable antennas started. The following years showed an accelerated rising trend in number of publications which at the time of elaborating this document shows no signs of slowing down.
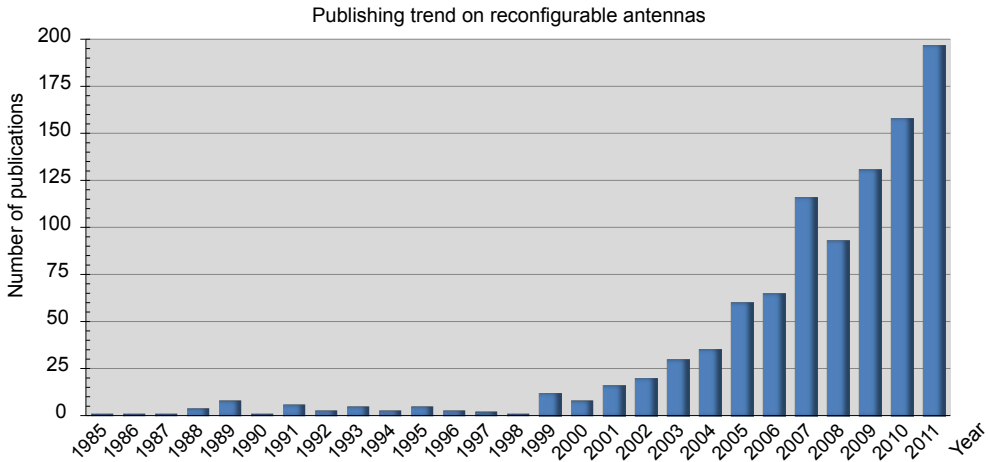
Fig. 1.3: Number of scientific paper and patents including the words *reconfigurable antenna* in the document title (data source: Google Scholar, October 2012).

1.2.3 Compound reconfigurability and pixel antennas

Reconfigurable antennas have been improving over these years, however the adoption in commercial system is extremely limited. This adoption will only occur when the system-level benefits of reconfigurable antennas widely outperform those of existing antennas. Additionally, new applications such as cognitive radio are demanding for a new level of reconfiguration. These are the reasons why some of the research in reconfigurable antennas is moving towards the design of RAs with a much higher level of reconfiguration. These new designs use a number of configurations one or two orders of magnitude higher than in typical RA designs to provide frequency reconfiguration over large frequency ranges while simultaneously, being able to adjust dynamically their radiation characteristics. This capability of simultaneously tuning several antenna parameters, for instance frequency and radiation pattern, is known as *compound reconfiguration*.

Compound reconfiguration is significantly more challenging to provide than classic one-dimensional reconfiguration. One of the most promising architectures achieving compound reconfigurability is the pixel antenna. Reconfigurable pixel antennas consist of a grid of electrically small metallic patches, where each pair of adjacent patches is interconnected by a RF-switch (Fig. 1.4). The activation or deactivation of these switches modifies the current distribution over the antenna surface, therefore providing reconfiguration capability to the antenna structure.

Pixel antennas have the capability to synthesize arbitrarily shaped surfaces by activating the appropriate switches. The synthesized surface is only limited by the overall size of the pixel surface and the individual pixel size. By way of example, Fig. 1.5 shows three out of the hundreds of configurations that a pixel antenna can produce. This surface reshaping capability is what allows pixel antennas to achieve a high degree of reconfigurability over frequency, radiation pattern and polarization.
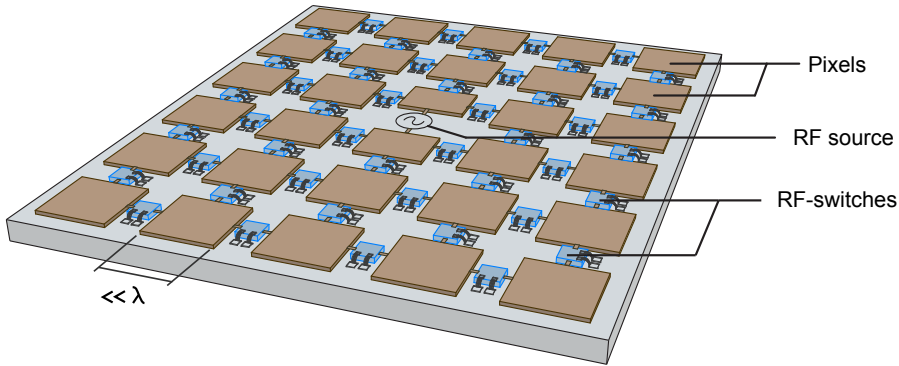
Fig. 1.4: Pixel antenna structure consisting of a grid with 5×6 pixels interconnected by RF-switches.

(a) Configuration #1   **(b)** Configuration #2   **(c)** Configuration #3
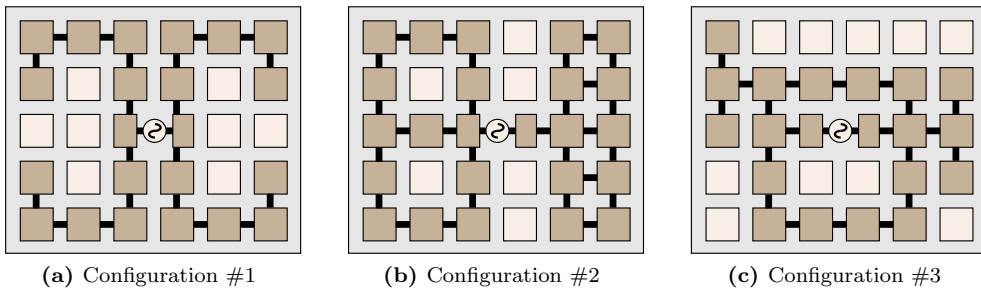
Fig. 1.5: Three different configurations of a pixel antenna. ON-state switches are represented by black segments, disconnected pixel are represented by white squares and connected pixels are represented by colored pixels.

The first proposal of a pixel reconfigurable antenna appears under the name *switched fragmented aperture* in [8] which applies the pixel concept to reconfigure dipole and monopole architectures. A similar design based on the same architectures is analyzed in [9] and their application to slot and patch architectures is presented in [10] and [11] respectively. A prototype of a fully-operational pixel antenna is first reported in [12]. Additional designs based on similar architectures can be also found under the terms self-structuring antenna [13–15], reconfigurable aperture (RECAP) [16] and evolving antenna [17].

Despite the outstanding reconfiguration capabilities of pixel structures suggested by the previous publications, there are important practical issues that must be addressed before pixel antennas can be implemented in commercial systems. These issues are basically related to the balance between complexity and performance in pixel antennas. From a practical perspective it is crucial that the antenna performance outweighs the additional complexity of a pixel structure. Therefore the objective of future research in pixel antennas is two-fold. On one hand, pixel antenna complexity must be reduced by minimizing the level of redundancy. Special focus is required on minimizing the

number of switches used by the pixel structure which is typically above one hundred and has a severe impact over the antenna radiation efficiency, over the biasing network and control circuitry complexity and consequently, over the antenna cost. On the other hand, it necessary to maximize the antenna reconfigurability being able to measure and quantify the reconfiguration level achieved by the antenna and its impact over the system-level performance.

1.3 OBJECTIVES

The encompassing objective of this doctoral work is to develop pixel antennas from their actual state as a conceptual structure into a practical reconfigurable antenna architecture.

The specific goals pursued in this work focus on defining new geometries to reduce the antenna complexity and also on the performance evaluation of the antenna reconfigurability. These goals range from the conceptualization of the pixel antenna geometry and new technological approaches, to experimental characterization techniques and the theoretical derivation of figures-of-merit, and are listed below:

- Propose novel pixel geometries and new conceptual architectures to improve the antenna reconfigurability while reducing the required number of switches and/or the overall complexity of the antenna. These geometries must remove the high level of redundancy of the existing pixel antennas which use uniform fully-switched pixel surfaces. Alternative conceptual architectures must explore new roles of pixel surfaces, for instance as parasitic elements.

- Explore switching and reconfiguration technologies for pixel antennas. Analyze the capabilities of existent semiconductor switches and develop new reconfiguration technologies to reduce insertion losses, increase isolation, decrease actuation power and in general to improve the switch and the pixel antenna performances.

- Enhance the knowledge about the maximum reconfiguration capabilities of pixel antennas. Existing publications explore specific optimized configurations, but leave unexplored the full reconfiguration properties of the antenna. The full frequency reconfiguration range and the complete diversity of radiation patterns must be characterized to properly judge the reconfiguration level of pixel antennas.

- Derive figures-of-merit to evaluate the reconfiguration level of pixel antennas and its impact over the system-level performance. Specific figures-of-merit to quantify antenna reconfigurability are not yet available in the current literature, even though being crucial to compare and determine which reconfigurable antenna designs provide higher performance.
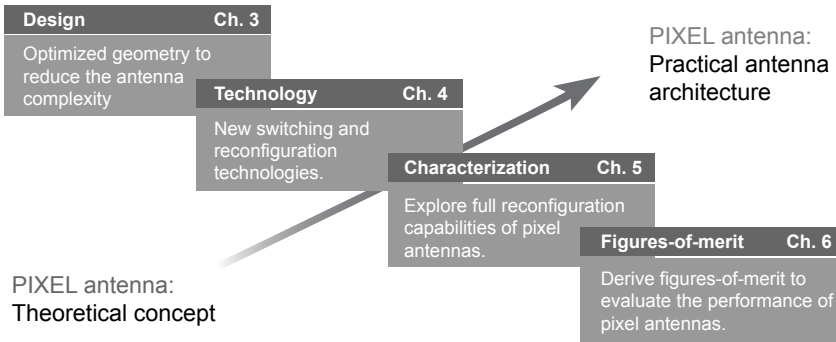
Fig. 1.6: Objectives and outline of the document.

1.4   OUTLINE OF THE DOCUMENT

This doctoral dissertation is organized in seven chapters, including this first chapter which introduces reconfigurable and pixel antennas and states the main goals of this work.

Chapter 2 presents a comprehensive and detailed analysis of the state-of-the art in antenna reconfigurability, covering applications, technologies and reconfiguration techniques. The information compiled in this chapter is essential to contextualize the ideas, designs, mechanisms and procedures presented in the following chapters.

The four subsequent chapters contain the main contributions of this doctoral research. Each of these four chapters focuses on one of the four objectives previously detailed as represented in Fig. 1.6.

- Chapter 3 addresses the conceptualization and design of pixel antennas and proposes novel geometries and conceptual architectures, such as multi-size pixel geometries and parasitic pixel layers, to reduce the complexity of pixel antennas.

- Chapter 4 focuses on the technological aspects of pixel antennas. It elaborates on the use of PIN diodes as switching elements with high reliability and explores new alternatives such as RF-MEMS and microfluidic technologies that can provide lower losses and higher reconfigurability.

- Chapter 5 presents the experimental characterization of pixel antenna prototypes based on the designs from chapter 3. Their full reconfiguration capabilities in frequency and radiation pattern is determined using both exhaustive and statistical characterization approaches.

- Chapter 6 covers the theoretical derivation of figures-of-merit to quantify radiation reconfigurability. Deterministic and statistic approaches are followed to derive figures-of-merit for RAs with a low number and a high number of configurations respectively.

The document is concluded in chapter 7 summarizing the main results presented along the document and commenting about the natural continuations of this research.

RECONFIGURABLE ANTENNAS

A detailed and up-to-date description of the most relevant works on the topic of reconfigurable antennas is provided in this chapter. The first section describes the main applications of the different types of reconfigurable antennas, covering from the most classical applications to the very recent developments. The second section focuses on the antenna reconfiguration technologies, understood as the most fundamental elements that provide tunability to the antenna structure. The third section addresses the design of reconfigurable antennas and describes the main techniques, architectures and structures used to achieve frequency, radiation pattern and/or polarization reconfigurability.

This structured compilation of applications, technologies and designs constitutes the current state-of-the-art of antenna reconfigurability, establishing the context of the work completed in this thesis and setting the foundations of the contributions that will be presented in subsequent chapters.

2.1 RECONFIGURABLE ANTENNA APPLICATIONS

In general we find applications of reconfigurable antennas in those situations where the operating requirements of a communication system change over time. The variation in the operating requirements may be produced by internal/user-driven factors, such as the required bandwidth and the user movement, or by external/environmental factors, such as interferences, spectrum occupancy and the presence of scatterers. In this section the different applications are described and classified according to the antenna parameter under reconfiguration.

2.1.1 Applications of frequency reconfiguration

The most representative application of frequency reconfigurability is the integration of multiple antennas in wireless equipment where several communication systems converge. Instead of using multiple single-function antennas, a single reconfigurable antenna can accommodate the multiple requirements. This is a very attractive approach for actual wireless equipment which integrate multiple communication systems, as depicted in Fig. 2.1a, and would lead to significant size reductions, which is of utmost

(a) Multi-antenna integration

(b) Out-band interference rejection

(c) Mitigation of close-body effects

(d) Cognitive Radio
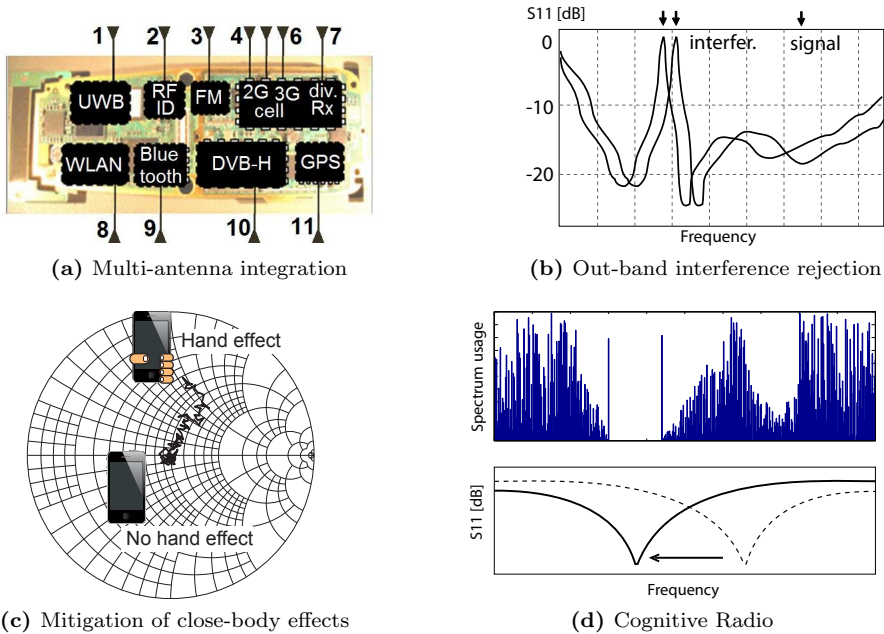
Fig. 2.1: Applications of frequency reconfiguration.

importance in portable and compact devices. In a similar way, it is possible to take advantage of frequency tunability in systems that use multiple frequency channels. In this case the main advantage is also the size reduction due to the fact that a wideband antenna covering simultaneously all channels is necessarily larger than a narrowband tunable antenna covering one channel at a time.

Frequency reconfigurability can be used also to reject out-band interferences. This is accomplished by synthesizing frequency responses with a band notch (high reflection coefficient) at the interference frequency while keeping a low reflection coefficient at the signal frequency as seen in Fig. 2.1b. Although the performance of this technique is limited, it can alleviate the specifications of the filters in the subsequent stages of the system [18].

Not only interference rejection is possible but also close-body effects can be mitigated. A well-known problem of portable wireless devices is that the antenna matching can be compromised due to the effect of surrounding artifacts, specially important are close-body and hand effects as shown in Fig. 2.1c. A reconfigurable antenna can monitor periodically the reflection coefficient and optimize the antenna response to compensate near-body effects [19, 20].

Finally, one of the applications recently capturing a lot of attention and where reconfigurable antennas play a key role is cognitive radio (CR). Cognitive radio transceivers sense the spectrum usage and the channel characteristics to dynamically select the operating frequency band according to specific performance metrics as illustrated in Fig. 2.1d. Cognitive radio can benefit from frequency reconfigurable antennas

(a) Beam-scanning

(b) In-band interference rejection

(c) Adaptive MIMO

(d) SAR level reduction
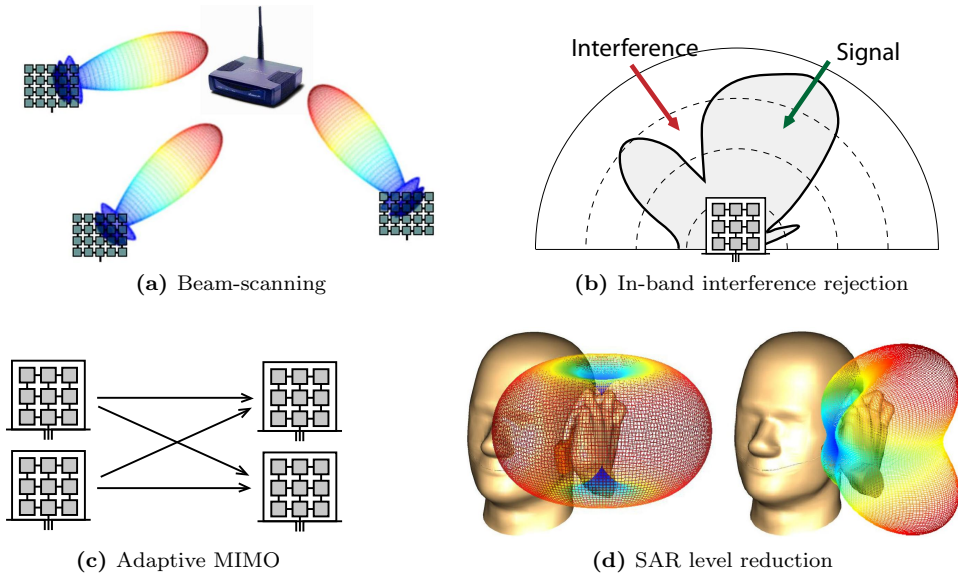
Fig. 2.2: Applications of radiation pattern reconfiguration.

because of the capability to tune the operating frequency over the required frequency range [21, 22].

2.1.2 Applications of radiation pattern reconfiguration

There is a great number of applications that can take advantage of the antenna capability to adjust its radiation pattern. The most classical application is beam-scanning or beam-steering. It consist in rotating automatically the antenna radiation pattern towards a certain direction of interest, as shown in Fig. 2.2a. This is useful in scenarios with mobile devices under line-of-sight (LOS) conditions because a high antenna gain can be obtained even when one or both communicating devices move and rotate. For these reason beam-scanning can provide improved coverage areas and higher data rates [23].

In a similar way as frequency reconfiguration can be used to reject out-band interferences, radiation pattern reconfiguration can reject interferences if their direction-of-arrival (DOA) is different than that of the signal. This is possible by adjusting the antenna radiation pattern in such a way that it presents high gain for the direction of interest and a null in the interference direction, as seen in Fig 2.2b. This means that it is possible to mitigate in-band interferences, which are much harder to filter by conventional ways than out-band interferences [24].

A much more recent application of radiation reconfigurability is adaptive MIMO which is roughly depicted in Fig. 2.2c. Adaptive MIMO replaces the multiple static antennas of standard MIMO systems by multiple reconfigurable antennas capable of synthesizing several different radiation patterns. By combining the spatial diversity of MIMO devices with the additional degrees of freedom provided by pattern recon-

figuration, the power and uncorrelation of the received signals can be improved and consequently, the channel capacity can be significantly increased [25–27], [JA10].

To complete the overview of radiation reconfigurability applications it is worth mentioning one of the most novel applications. Taking advantage of radiation pattern reconfiguration it is theoretically possible to reduce specific absorption rates (SAR) in personal wireless devices. The basic idea is to modify the antenna radiation pattern of the wireless device while it is being approached to the user's body favoring radiation towards non-blocked directions. This procedure would result in a improvement in the battery autonomy as well as a reduction of the power dissipated in the user's body.

2.1.3   Applications of polarization reconfiguration

Polarization reconfigurable antennas are typically exploited to reduce polarization mismatch losses in portable devices. The variable orientation of portable devices can degrade transmission performance if the polarization of the transmitter and receiver are not aligned. In these cases, the use of self-orientable antennas is recommended, especially in linearly polarized systems under LOS conditions [28, 29]. Under these conditions, a polarization reconfigurable antenna switching between two orthogonal polarizations can also be used to provide a double transmission channel suitable for frequency reuse.

If LOS conditions do not apply, the communications channel typically presents a high uncorrelation between horizontal and vertical polarizations. In this case, polarization reconfigurability can be used as a polarization diversity system or as a way to enhance the performance of MIMO systems in a similar way as pattern reconfiguration [30].

2.1.4   Applications of compound reconfiguration

There are multiple situations where it is desired to incorporate two or more of the previously presented capabilities. In these cases it is required to combine frequency, radiation pattern and/or polarization reconfigurability. Certain combinations of capabilities are particularly useful.

The most notorious application is the combination of frequency agility and beam-scanning to provide improved spectral efficiencies. By taking advantage of compound reconfigurability it is possible to dynamically shift the operating frequency band towards less crowded portions of the spectrum and simultaneously steer the radiation beam toward the position of the second element in the link [31]. This way the improvement of spectral efficiency is two-fold; first, noise and interferences are reduced due to the frequency band selection mechanism and second, the link power budget increases as a result of the higher antenna gains after performing the beam-steering procedure.

A second application is enhanced interference rejection. Since out-band interferences can be partially filtered using frequency reconfigurability and in-band interferences can be rejected by taking advantage of pattern reconfigurability, the combination of these two makes possible to obtain improved interference rejections. The result is a higher signal-to-interference ratio (SIR) and a more robust rejection capability [CA4].

There is another application that is worth mentioning. Using compound reconfigurable antennas it is possible to mitigate the undesirable close-body effects which damage the performance of most wireless personal devices. Thanks to impedance tunability it is possible to mitigate the degradation of the antenna matching due to hand or head effects, and simultaneously take advantage of pattern reconfigurability to reduce the SAR levels by redistributing the radiation towards non-blocked directions.

These are only some illustrative examples of applications showing the potential of compound reconfigurability. However it is expected that as soon as low-complexity cost-effective designs of compound reconfigurable antennas are available, novel applications will be rapidly developed to take advantage of compound reconfiguration capabilities.

2.2 RECONFIGURABLE ANTENNA TECHNOLOGIES

Having detailed the main applications of antenna reconfigurability, the next natural question is "how to provide reconfiguration capabilities to antenna structures?". Since a reconfigurable antenna is a radiating structure that can conveniently adjust its operating parameters, it is obvious that there must exist an element in the antenna structure with variable characteristics. This section focuses on this very basic element which is the ultimate responsible for the antenna reconfigurability. The present sections describes the key enabling technologies that make possible antenna reconfiguration.

2.2.1 Lumped components

Lumped components are the clear dominant reconfiguration elements used by reconfigurable antennas. Reconfigurable antennas using lumped components concentrate tunability in very specific positions of the antenna structure where a variable load is located. The two main types of tunable loads are RF-switches and variable capacitors. RF-switches are advantageous in terms of control circuitry, since they can be controlled by a simple digital circuit, and can also produce configurations with very different properties due to the large impedance variation between its two states. On the other hand, reconfiguration using RF-switches is limited to a discrete number of states. Instead, variable capacitors can provide continuous tunability which can be very convenient in certain applications. However, continuous tunability comes at the expense of a more complex control circuitry and higher similarity between different antenna configurations.

The most conventional technology used nowadays to implement switches and varactors is semiconductor technology. A PIN diode changing between forward and reverse biasing can behave as an excellent RF-switch. On the other hand, PIN diodes with a variable reverse bias voltage can behave as variable capacitors. PIN diodes are widely used due to their robustness, low cost and circuital parameters, basically insertion losses and/or isolation, which are excellent at lower frequencies (below 10 GHz). Their power consumption is of few milliwatts which can be excessive in designs requiring a large number of switches. In these cases, PIN diodes can be replaced by FET transis-

tors, which have power consumptions below a tenth of milliwatt, but at the expense of lower performance in terms of insertion losses and/or isolation.

One of the most promising technologies, clearly overcoming semiconductor elements in many aspects, is micro-electromechanical technology (RF-MEMS). RF-MEMS switches and varactors can provide a much lower insertion loss (in the order of 0.1 dB), almost zero power consumption and higher linearity. However, there exist practical issues which nowadays limit their use in reconfigurable antennas. The cost RF-MEMS is higher than semiconductor elements due to the expensive packaging processes and their reliability is lower, specially for RF-MEMS switches which suffer from severe stiction problems. Even considering these drawbacks, the use of RF-MEMS technology can enable reconfigurable systems with a much higher performance [32]. Many examples of MEMS-reconfigurable antennas are available in the literature, among them several of the RA designs that will be presented in section 2.3.

One of the main difficulties in designing reconfigurable antennas using lumped components is the design of the bias network required to modify the status of switches and varactors. The electromagnetic coupling between the biasing lines and the antenna structure can severely damage the antenna reconfiguration capabilities and its design is much more challenging than in non-radiating microwave devices where electromagnetic fields are confined. Some useful guidelines for the biasing of reconfigurable antennas are the minimization of the biasing lines length and take advantage of existing antenna parts for biasing whenever possible. Bias lines have to be located in regions with a less intense near-field, for instance behind ground planes, and its orientation must be orthogonal to the polarization of existing electric field. Another useful technique consists on loading the bias lines inductively or with high-resistive materials.

To conclude the review of lumped components it is worth mentioning some additional technologies based on semiconductors and RF-MEMS which have been proposed to avoid the use of bias lines. This is the case of optically controlled switches, whose status is controlled by an optical signal distributed using dielectric waveguides which produce a much lower degradation of the antenna properties than conventional metallic lines [33, 34]. Bias lines can be also avoided by using Reed switches whose status can be remotely controlled by an external magnetic field [35].

2.2.2   Tunable materials

Reconfiguration characteristics can be also provided by using materials with tunable electromagnetic properties. Unlike lumped components which concentrate tunability is specific locations, in the case of RAs using tunable materials the reconfiguration element is distributed over the antenna volume and is typically used as part of the substrate in printed antennas.

Tunable materials have interesting advantages, in particular continuous reconfigurability can be provided with a simple control circuitry. On the other hand, these type of materials tend to be lossy and the resulting reconfiguration capabilities are not as high as with other technologies. For these reasons, their use is not as widespread as lumped components.

One classical example of tunable material are ferrites, whose permeability can be

tuned by an external magnetic field. The controlled change in permeability can be used to implement reconfigurable antennas [36–38]. In a similar way, the electric permittivity of ferroelectric materials can be changed by applying an external electric field and this way can be used to tune the antenna properties [39], [40].

Liquid crystals are another type of material with tunable characteristics. The orientation of the molecules in a liquid crystal can be modified by a controlled static electric field and due to the material anisotropy this leads to changes in its electric permittivity tensor. There is extensive literature on the use of liquid crystals for implementing reconfigurable antennas [41,42], specially on the topic of beam-scanning reflectarrays [43–45].

Finally, it is worth mentioning two additional examples of less widespread tunable materials. These materials are optically tuned semiconductor materials [46] and colloidal dispersions, which are dielectric liquids with a variable density of particles that influence the resulting permittivity [47,48].

2.2.3 Movable antennas

The third technology in order of significance in antenna reconfiguration are movable and rotatable antennas. This is actually one of the most basic forms of reconfiguration and one of the very first to be implemented [49]. By actuating over the antenna structure it is possible to change its position, orientation and structure, and as a result the antenna properties are modified.

Several types of actuation mechanisms are used in movable and rotatable antennas. The most elemental mechanism is mechanical actuation using linear actuators, stepper motors or similar devices that can induce movement [50, 51]. More evolved mechanisms include electrostatic actuation over the whole antenna structure [52] or, more commonly, magnetic actuaction [53–55]. Recently, new reconfigurable designs start appearing in the literature using liquid metals to implement deformable antennas [56, 57] and reconfigurable antennas [JA6].

Although movable antenna technology have certain drawbacks, specially regarding the reconfiguration speed and the risk of wear-and-tear failure, it is a promising technology for antennas operating at higher frequencies, such as 60 GHz band, where antenna sizes are smaller and mechanical actuation becomes more effective.

2.3 RECONFIGURABLE ANTENNA DESIGNS

The present section describes the different techniques taking advantage of the previously presented technologies to obtain specific reconfiguration capabilities. Nowadays, there is available in the scientific literature a great number of reconfigurable antenna designs. A deep analysis of the existing work reveals that the existing designs use certain common reconfiguration techniques depending on the parameter to be tuned (frequency, pattern and/or polarization). This section examines and classifies the different reconfiguration techniques and provides illustrative examples in each case.

(a) Tunable matching network

(b) Multi-antenna switching

(c) Multi-port antenna switching

(d) Phased array
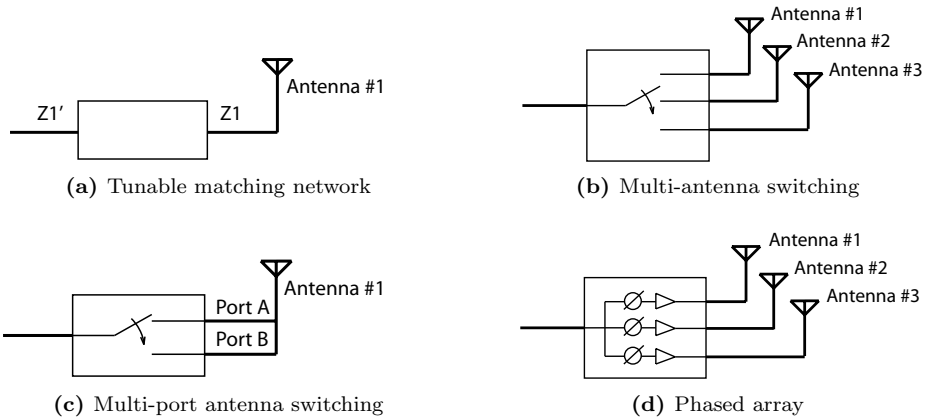
Fig. 2.3: Classification of externally RA designs.

2.3.1 State-of-the-art of externally reconfigurable antennas

The initial reconfiguration techniques relied on external feeding networks with tunable properties. These tunable external feeding networks where used to transform the antenna impedance, to modify the feeding position or to switch between different antennas. It must be mentioned that since the reconfiguration elements are external to the antenna surface and they do not interact directly with the radiation mechanism, strictly speaking, designs following this approach are not considered reconfigurable antennas. However, since tunable feeds are the first form of antenna tunability and are still being used nowadays, it is worth including them into the discussion.

The different types of reconfiguration techniques using external tunable feedings are represented in Fig. 2.3. The external feeding network can be an impedance transformer to dynamically tune the antenna; a switched network to switch between different feed antennas or feed positions; or a phase-shifting network to combine conveniently the radiation of multiple antennas.

Tunable matching networks (Fig. 2.3a) are used to modify the antenna input impedance, and may be used to provide frequency agility or to mitigate unmatching during the system operation [58]. These networks are composed of a tunable impedance transformer and a control unit. The most common architectures for the impedance transformer are LC series circuits, stub lines and distributed MEMS transmission lines. The impedance transformation ratio is determined by the control unit which monitors the reflected signal and takes decisions according to its value. Tunable matching networks can achieve frequency reconfiguration over frequency ranges up to one or two octaves [59], being the main limitation the narrow bandwidth obtained at frequencies where the existing antenna is initially highly reactive. A different application of tunable matching networks is the mitigation of undesired variations of the antenna impedance. This is especially interesting for cellular and mobile applications, where the presence of artifacts in the near-field region of the antenna, specially parts of the user's body, has a severe effect over the antenna impedance [19].

A different approach to achieve reconfiguration capabilities is to use switched networks to switch between several antennas with different frequency and radiation properties (Fig. 2.3b). In this case, a specifically designed antenna is used for each operating mode and a switched network selects dynamically the required antenna according to the active operating mode. Since each antenna mode is located in a different physical region, the main advantage of this approach is the design flexibility, but the main drawback is the large size occupied, especially when a high number of operating modes is required.

Switched multi-antenna systems can provide frequency reconfigurability by switching between antennas with different dimensions. By applying the appropriate scaling factor, each antenna can be designed to cover a different frequency band. For instance, in [60] four different sized dipoles are used to provide coverage over four independent frequency bands. On the other hand, pattern reconfiguration can be achieved by using multiple equally-sized antennas located in different orientations to steer the radiation beam towards different angular directions. Examples of switched antennas with pattern reconfigurability can be found in [61] and [62], where switched multi-antenna systems are presented using two printed Yagi antennas and three CPW slot-based antennas, respectively.

In some cases the multiple antennas required by the previous approach can be replaced by a single multi-port antenna (Fig. 2.3c). The basic idea is to use an antenna structure that supports multiple resonant modes and excite them independently by changing the feed position. These multi-port prototypes lack of the design flexibility of switched multi-antenna systems but can achieve similar performance with smaller sizes, being the main difficulty in the antenna design the procurement of high isolations between the different input ports. This technique is well suited for polarization diversity applications as is illustrated in [29, 63] where microstrip patch antennas are used to produce different linear and circular polarizations.

A final approach to achieve pattern reconfiguration capabilities with multi-antenna systems is to combine the radiation from the multiple antennas instead of switching between them. The most common structures based on this approach are phased arrays (Fig. 2.3d), which consist of an antenna array where the phases of the feeding signals can be individually adjusted [64,65]. By synthesizing an appropriate phase distribution the array pattern can be effectively steered towards specific directions. Although this structure requires a more complex feeding network than the previous approaches, the potential reconfiguration capabilities are enhanced and a better control of the radiation pattern is obtained.

2.3.2   State-of-the-art of frequency RAs

The underlying principle of operation of frequency reconfiguration is the variation of the effective length of a resonant antenna. The variations in the antenna dimensions produce shifts in the resonant frequency and, as long as the current distribution is scaled with the antenna size, the radiation pattern remains unchanged.

Although there is a common principle of operation for frequency reconfiguration, there exist different mechanisms that can be used to modify the antenna length. These mechanisms are illustrated in Fig. 2.4.

(a) Physical length modification

(b) Electrical length modification

(c) Variable reactive loading
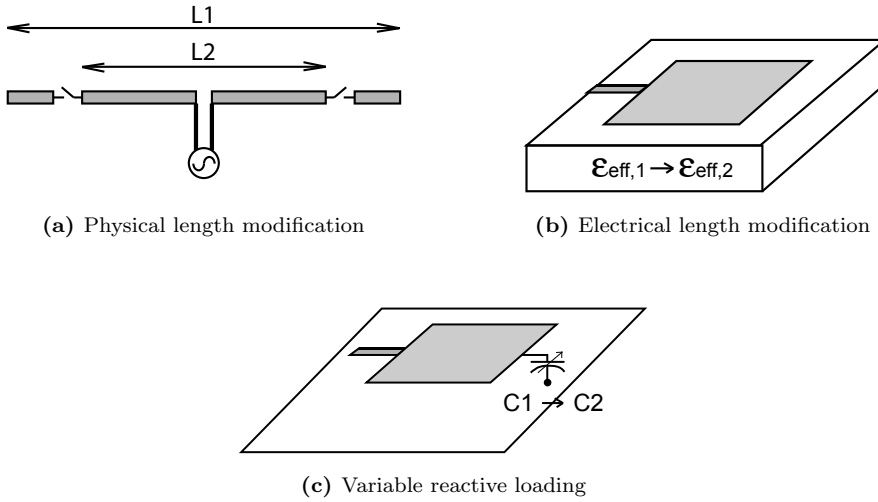
Fig. 2.4: Classification of frequency RA designs.

The first technique tunes the antenna frequency by increasing or decreasing the antenna physical length (Fig. 2.4a). This is typically achieved by using RF-switches to connect or disconnect metallic sections to the main antenna body so its length gets modified. In wire antennas, when switches change to ON-state the antenna length increases and low-frequency modes are obtained. On the other hand, OFF-state configurations reduce the antenna length and result in high-frequency modes. For slot-type architectures this behavior get reversed. This technique has been successfully applied to reconfigure the resonant frequency of dipoles [34], slots [66–68], fractal antennas [69], and even dielectric resonator antennas [70]. In all these examples the antenna is tuned by means of RF-switches, except for the DRA, which is tuned by altering the level of the dielectric liquid composing the antenna.

Frequency reconfiguration can also be provided by keeping constant the antenna physical length but modifying its electrical length (Fig. 2.4b). This can be done by altering the propagation constant in the antenna structure. The most conventional approach in this case is to change the electrical permittivity of the antenna substrate by using tunable materials. A higher electrical permittivity reduces the effective wavelength, which makes the antenna larger in terms of this effective wavelength and as a result, shifts the antenna resonance to a lower frequency. In general, this technique is used in printed antennas where the electromagnetic fields are confined in the dielectric [42, 46]. A different technique to modify the propagation constant in the antenna structure consist in changing the geometry of the region where the fields are confined. This is effective in microstrip antennas where the propagation constant can be adjusted by modifying the height of the microstrip antenna [52] or by tilting an out-of-plane microstrip radiator [53].

The third technique used by frequency-agile antennas is based on loading the antenna with a variable reactive load (Fig. 2.4c). The reactive load compensates the

(a) Movable and rotatable antennas

(b) Tunable parasitics (in the near-field region)

(c) Tunable parasitics (in the far-field region)
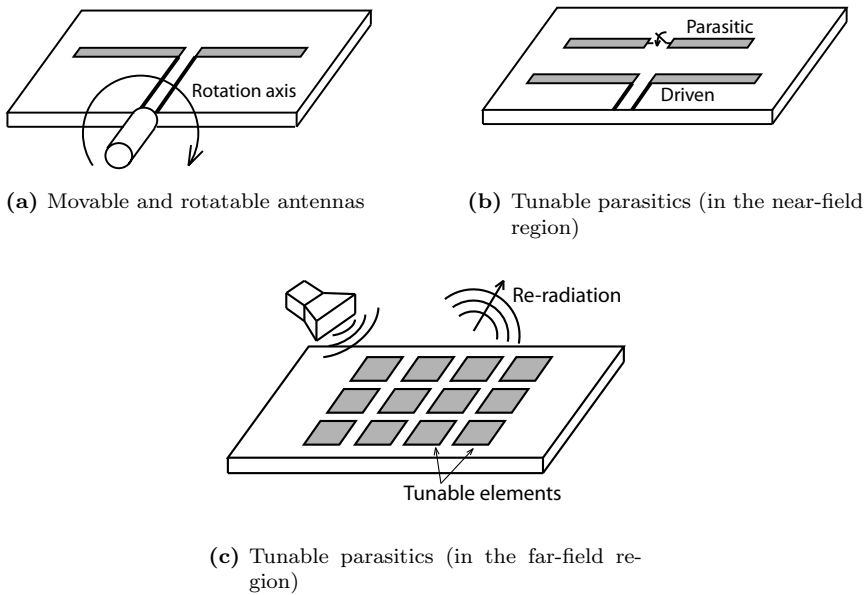
Fig. 2.5: Classification of pattern RA designs.

reactive part that appears in the antenna input impedance when the frequency is shifted away from its natural resonance frequency [71]. Therefore, different values of the reactive load, typically a varactor, result in variations of the antenna resonance frequency. This technique has the advantage of continuously shifting the antenna resonance frequency and therefore, surpassing switched-reconfiguration techniques in fine tuning capability. On the other hand the frequency reconfiguration range is not as large as the one obtained by the other mentioned techniques. It has been recently showed that impedance loading is compatible with switching techniques, allowing to produce configurations with distant resonance frequencies, each one of them finely tunable due to impedance loading [72].

2.3.3 State-of-the-art of radiation pattern RAs

The radiation pattern of an antenna is related to its current distribution by a Fourier transform. Therefore, radiation pattern reconfiguration can only be achieved by altering the global current distribution. The main challenge in pattern reconfiguration is to keep the input impedance constant while the main currents over the antenna are modified. The basic pattern reconfiguration techniques are illustrated in Fig. 2.5.

The most conceptually simpler technique to reconfigure the antenna pattern is to rotate the complete antenna structure by using movable antennas (Fig. 2.5a). The rotation of the antenna rotates its radiation pattern and leaves its reflection coefficient

unaffected. In spite of the conceptual simplicity of this technique, its application often leads to bulky mechanical actuators that result in significant drawbacks in terms of reconfiguration speed and power consumption. These disadvantages are strongly mitigated when the antennas are fabricated at microscale. At this point, RF-MEMS technology is ideal to fabricate movable antennas with the required micro-actuators. One classical example corresponds to reference [49] where the arms of a dipole antenna are simultaneously rotated by push-pull actuators to steer its radiation pattern. In [55] it is presented a rotatable 2x2 patch array where magnetic actuation is used to rotate the antenna around two orthogonal axes and steer the radiation beam in E-plane and H-plane.

A different strategy to reconfigure the antenna pattern consists in using switched or tunable parasitic sections. The coupled currents over these parasitic elements have a significant effect over the radiation pattern without producing drastic perturbations over its input impedance. This is by far the most widely used technique to reconfigure the antenna radiation pattern.

In antennas with a low number of parasitic elements, the parasitic elements need to be located into the near-field of the driven element in order to couple strong currents, which are necessary to modify the antenna pattern (Fig. 2.5b). Typical distances between the driven and parasitic elements are between 0.1 and 0.5 wavelengths; this ensures strong currents on the parasitics without damaging severely the well-matching of the driven antenna. Pattern reconfigurable antennas using switched parasitic have been implemented for the main antenna architectures such as monopoles [73, 74], microstrip elements [75–77] and slot antennas [78]. A higher degree of reconfigurability can be achieved by using reactively loaded parasitics instead of switched parasitics. The underlaying theory of reactively controlled arrays was established in a classical paper by R.F. Harrington [79] and its capabilities are still under continuous study [80].

Parasitic elements can also be located at a higher electrical distance of the driven antenna. However, the required number of parasitic elements is much higher than in the previous case. This is the approach followed by reconfigurable reflectarrays and lens arrays. In these cases, the operation of the parasitic elements follows the same rules as in conventional arrays. By controlling the phase of the re-radiated field by each element of the array, the direction of the antenna beam can be precisely controlled. It is important to notice that despite the evident similarities with phased array antennas, this method is very different from a conceptual perspective. The re-radiated field by each element of the array is not controlled by an external feeding network but by the tunable architecture of the element itself. Practical implementations of reconfigurable reflectarrays can be found in [81–84] and an example of a reconfigurable lens-array is presented in [85].

Two additional structures are also used to provide radiation pattern reconfiguration capabilities which are multi-mode and leaky-wave antennas. By using several switches strategically located in a multi-mode antenna, the different modes can be individually activated. Since the radiation patterns associated to the different modes are different from each other, radiation pattern reconfiguration is accomplished. This concept has been applied to design a reconfigurable spiral antenna in [86]. On the other hand, leaky-wave antennas can be provided with reconfiguration capabilities by controlling

(a) Symmetry transformations   (b) Combination of multiple modes
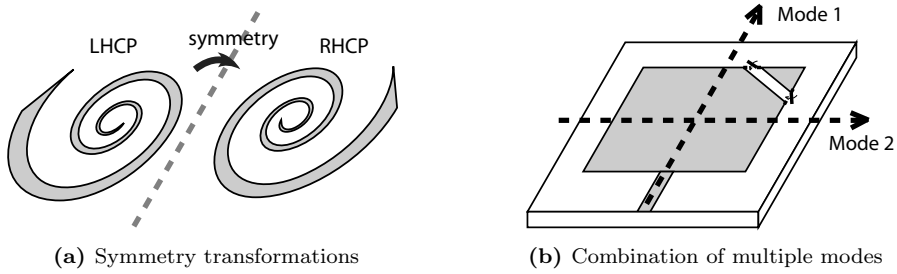
Fig. 2.6: Classification of polarization RA designs.

the phase velocity of the radiating leaky mode. This can be effectively accomplished using tunable periodic structures [87, 88].

2.3.4 State-of-the-art of polarization RAs

The polarization of an antenna is determined by the direction of its electrical currents. There are two basic techniques for modifying the direction of the antenna currents (and its polarization, as a consequence) preserving its frequency of operation and radiation pattern. These techniques are illustrated in Fig. 2.6.

The first technique uses RF-switches to modify the antenna structure in such a way that the resulting configuration is a symmetric version of the original configuration. In [30] this technique is applied to a spiral antenna producing two different configurations where the second is a symmetric version of the first. This transformation preserves the frequency response, produces minor perturbations to the radiation pattern and transforms left-hand circular polarization (LHCP) into right-hand circular polarization (RHCP). The main drawback of this technique is that RF-switches have to be distributed over the whole antenna surface and complex biasing networks are required.

Polarization agility can also be achieved without locating switches over the whole antenna structure by taking advantage of multi-mode antennas. In this case, the different modes of the antenna are simultaneously excited and reconfiguration is obtained by introducing minor perturbations that affect the way these modes are combined. In [89] a nearly-square patch antenna achieves polarization reconfigurability by combining a horizontal and a vertical mode. When the switch is in OFF-state the two modes are combined with equal amplitude and 90 degrees phase difference, producing circular polarization. However, switching the MEMS device to ON-state breaks the balance between the two modes and creates linear polarization. A CPW antenna based on the same principle is presented in [90] to switch between linear polarization, right-hand and left-hand circular polarizations. The combination between different modes is very sensitive to frequency shifts and for this reason, a narrow bandwidth regarding polarization is a typical disadvantage of multi-mode polarization-agile antennas. However, this drawback is often overcome by the simplicity of the antenna structure.

(a) Combination of single-parameter reconfigura-
tion techniques

(b) Reconfigurable PIXEL apertures
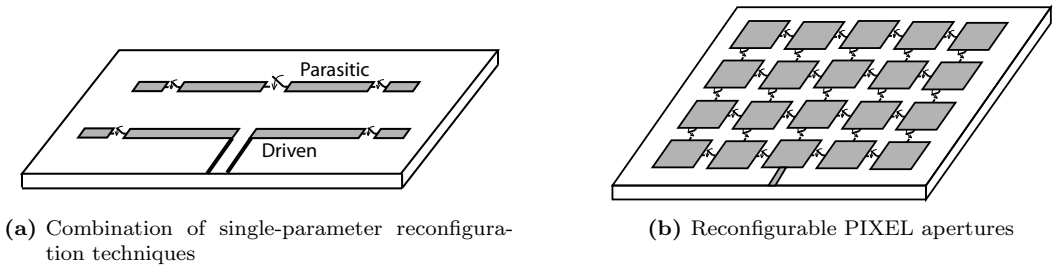
Fig. 2.7: Classification of compound RA designs.

2.3.5   State-of-the-art of compound RAs

The ultimate goal of reconfigurable antennas is to be able to independently adjust the frequency of operation, the antenna pattern and the polarization. The simultaneous tuning of frequency and radiation properties is known as compound reconfiguration. However, while single-parameter reconfiguration is a deeply studied problem, the situation is quite different when considering compound reconfiguration. In this case, the interdependence between the different antenna parameters constitutes a much greater obstacle than in the single-parameter reconfiguration. At the time of writing this document very few publications attempt the simultaneous reconfiguration of two antenna parameters and, to the best of the author knowledge, the simultaneous reconfiguration of frequency, pattern and polarization has not been yet achieved, at least in the open literature.

The main progresses towards compound reconfiguration have followed two basic approaches, which are depicted in Fig. 2.7.

The first approach consists on combining in the same structure different single-parameter reconfiguration techniques (Fig. 2.7a). For instance, an antenna can combine a driven element with tunable length with a switched parasitic to simultaneously reconfigure its operating frequency and radiation pattern. Compound reconfigurable antennas following this approach are relatively simple in structure but their reconfiguration capabilities are very limited, due to compatibility problems between different one-dimensional techniques. The number of operation modes is relatively low, usually between four and six modes, which results in a low number of possible operating frequencies, radiation patterns and polarizations.

One of the most representative implementations following this approach is presented in [91], which presents a frequency and pattern reconfigurable patch antenna. The radiation pattern of the microstrip patch is tilted by adding switchable patch parasitics. The same antenna is able to tune the frequency of operation by loading the parasitic elements with switchable slots, thus tuning the resonance frequency of these parasitics. A different implementation of a frequency and pattern reconfigurable antenna is presented in [92], where a pattern reconfigurable ring slot is combined with a tunable matching network to achieve frequency reconfigurability. A similar design based in a ring slot antenna can be found in [93], but in this case it is frequency

reconfigurability what is provided by the tunable ring slot while polarization diversity is obtained by using a tunable multiport feeding. Other designs worth mentioning are presented in [34, 94] which present frequency and radiation pattern reconfigurable antennas using spiral and dipole architectures respectively.

Recently there has been a growing interest for high-gain beam-scannable antennas with additional degrees of reconfigurability due to satellite communications and remote sensing applications. Some promising results have been obtained using reflectarray architectures to achieve beam-scannable antennas with polarization reconfigurability [95–97] and frequency tunability [98, 99].

The second approach to provide compound reconfigurability takes advantage of structures with an inherent capability of modifying simultaneously both frequency and radiation properties. These structures consists of a dense distribution of electrically small metallic sections interconnected by switches. These small metallic patches are called pixels, and the resulting antenna architectures are known as reconfigurable apertures or pixel antennas (Fig. 2.7b). Instead of introducing specific perturbations over the antenna surface, as done by other reconfiguration methods, pixel antennas reshape the complete antenna surface by activating specific switch configurations. Optimal configurations are determined by discrete optimization algorithms such as particle swarm optimization (PSO) or genetic algorithms (GA).

The precursor of current pixel antennas are fragmented apertures [100, 101], which are a type of non-reconfigurable antenna composed of small metallic pixels whose global shape was determined by optimization algorithms to synthesize specific properties, typically broadband capabilities. Pixel antennas were derived from these structures when it was observed that by locating switches between its pixels it was possible to provide unique reconfiguration capabilities [8, 9]. These initial works paid special attention to the achievable gain of pixel antennas based on the discretization level (pixel size), the aperture size and the non-ideal characteristics of the switching element [102]. The next remarkable accomplishment in the evolution of pixel antennas was the implementation of a fully operational prototype which used a monopole architecture and FET transistors as switching elements [12]. Nowadays, the pixel antenna concept has been extended to different architectures such slot [10] and microstrip patch [103].

Compared against any other reconfigurable antennas presented in this chapter, pixel antennas provide a new level of reconfiguration. They are extremely flexible structures due to the possibility of synthesizing a rich variety of antenna shapes. The resulting number of operation modes is much higher than in conventional reconfigurable antennas, leading to multi-parameter reconfiguration covering broad frequency ranges and being capable of synthesizing multiple radiation patterns and polarizations. On the other hand, pixel antennas involve a large complexity, typically requiring beyond a hundred switches, which produces severe impacts over the antenna cost and efficiency.

Pixel antennas are the central topic of this doctoral dissertation, which focuses on the development of pixel antennas with a very reduced number of switches [JA7], [CA8], introducing novel conceptual architectures [JA8], [JA4], [CA5], developing new enabling technologies [JA6] and establishing figures-of-merit to evaluate their performance [JA3].

PIXEL ANTENNA CONCEPTUALIZATION AND DESIGN

T HE design of improved pixel antennas is the central topic of this section. First, the basic architecture of pixel antennas is described and the most fundamental design guidelines are provided. Then, the main approaches followed to perform the electromagnetical simulation and optimization of pixel antennas are detailed. After these general concepts of pixel antennas two novel pixel geometries and conceptual architectures are presented, the multi-size pixel antenna and the parasitic pixel layer.

3.1 PIXEL ANTENNA ARCHITECTURE

The main architecture and the basic components of a pixel antenna are depicted in Fig. 3.1.

Pixels

The most basic components of a pixel antenna are the pixels which compose the antenna structure. These pixels are sub-wavelength metallic sections that when inter-

Fig. 3.1: Pixel antenna architecture

(a) Square tessellation

(b) Triangular tessellation

(c) Hexagonal tessellation

(d) Semiregular tessellation
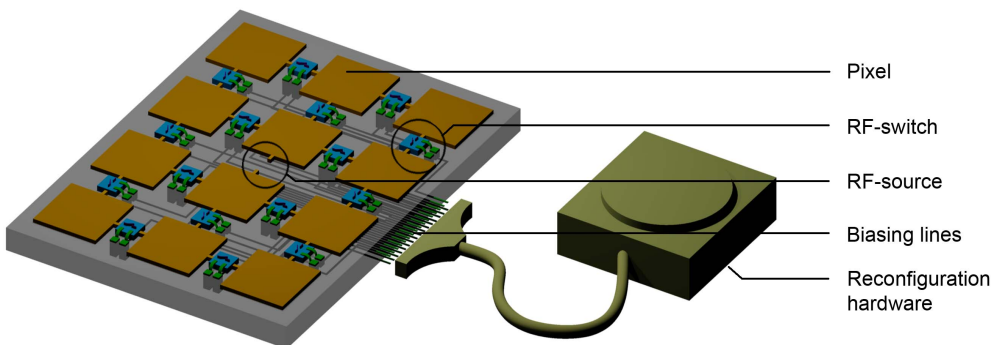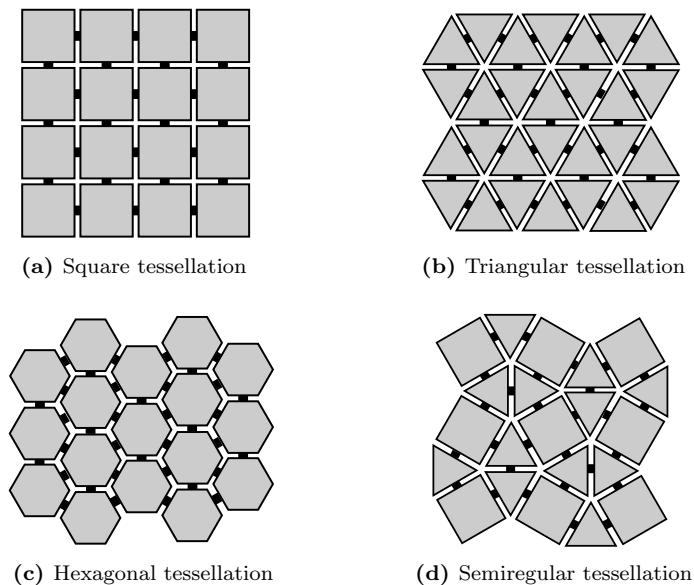
Fig. 3.2: Different types of tessellation for pixel antennas.

connected between them produce the required impedance and radiation properties of the antenna. The most conventional pixel shape is a square and in fact, to the best of the author's knowledge, this is the shape used by all the existing implementations of pixel antennas. However the geometrical shape of the pixel can be different than a square as long as it makes possible to produce a plane tessellation by replicating the basic shape. Specially interesting are the three possible regular tessellations which are depicted in Fig. 3.2 and correspond to pixels with square, triangular and hexagonal shapes. These three are the only possible tessellations using replications of a single regular polygon [104], however many more alternatives are available when different pixel shapes are combined as shown in Fig. 3.2d. The pixel antenna concept could be in fact extended to three-dimensional structures by using volumetric pixels together with switches interconnecting their faces. Some of these less conventional geometries have been analyzed in [17].

RF-switch

The second essential component in pixel antennas is the RF-switch interconnecting adjacent pixels. The main technologies to implement RF-switches are semiconductor and RF-MEMS technologies which will be discussed in chapter 4. It has been observed that the influence of the switch isolation over the pixel antenna reconfigurability is relatively low as long as the isolation is above 12 or 14 dB. On the other hand, the switch insertion loss has a drastic effect over the antenna efficiency. Due to the large number of serially concatenated switches, the equivalent ohmic resistance of the pixel

antenna can be several times that of the switch. Some interesting results regarding the gain of reconfigurable apertures depending of the switch insertion loss are presented in [102].

Biasing lines

In order to operate the switches they must be controlled by an external source signal which is transported by biasing lines. Ensuring a low coupling between the biasing lines and the pixel structure is essential to preserve the antenna reconfiguration capabilities. This undesired coupling, which has important effects in most reconfigurable antenna designs, is particularly severe in pixel antennas due to the large number of switches and biasing lines. Some techniques to mitigate the coupling of the biasing lines consist in locating the biasing circuitry behind the ground plane of microstrip pixel antennas [103], use inductively loaded lines [JA7] or, in the case of RF-MEMS, to use high-resistivity lines.

Reconfiguration hardware

The status of the switches is determined by a control hardware that implements the reconfiguration scheme. There are two main approaches followed by the reconfiguration procedure. The first approach consist on performing a prior characterization of the pixel antenna characteristics by analyzing the properties of the different configurations and selecting those of them which provide certain performances, for instance a specific operation band. These configurations are stored in a static look-up table and the reconfiguration scheme basically selects the best configuration from this table according to the operational requirements. The second approach implements an optimization algorithm directly in the reconfiguration hardware. The optimization algorithm tests and optimizes the switch configuration in real-time. Unlike the previous approach, this real-time optimization can deal with changing environments, for instance it allows to preserve the antenna matching even in the presence of close-artifacts, such as the hand of the user. This additional capability comes at the expense of a higher training time. It is also possible to combine the two previous approaches by doing a prior selection of configurations to remove a certain degree of redundance in the configurations space and perform a real-time optimization over this selected group of configurations. This mixed approach can be used to balance the system adaptability and the reconfiguration speed.

3.2   PIXEL ANTENNA DESIGN AND OPTIMIZATION

Having described the main components of a pixel antenna we present now the main guidelines in pixel antenna design as well as the different simulation and optimization techniques.
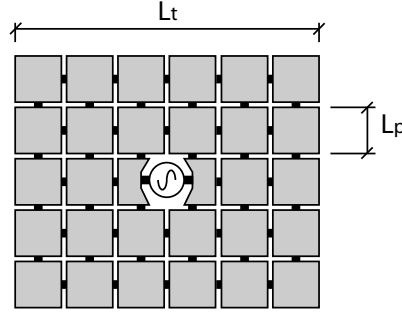
Fig. 3.3: Basic dimensions of a pixel antenna

3.2.1   Design guidelines

The ultimate goal in pixel antenna design is the determination of a clear relation between the pixel antenna geometry and its reconfiguration capabilities. Such relation would allow to design a certain pixel surface to provide the required reconfiguration capabilities. Although this goal has not been yet achieved, certain rules-of-thumb can be applied to the design of pixel antennas. The total size (L_t) of the pixel surface is basically determined by the required gain of the pixel antenna. Therefore the antenna size can be designed using the equations that relate the antenna size with its maximum gain [105]. This evaluation has to be done for the most restrictive frequency, which in this case corresponds to the lowest frequency. Therefore, the minimum pixel antenna size can be found from the following equation

$$(\pi L_t/\lambda_{\text{low}})^2 + (\pi L_t/\lambda_{\text{low}}) > G \tag{3.1}$$

$$L_t > \tfrac{1}{2\pi}\lambda_{\text{low}}\left(\sqrt{4G+1}-1\right) \tag{3.2}$$

where λ_{low} is the free-space wavelength at the lowest frequency of operation. Notice that the resulting value is an lower bound for the antenna size and the actual size should be larger in order to account for the illumination efficiency of the pixel aperture and the losses produced by the switches.

In certain applications, specially in mobile and portable communications, radiation pattern directionality is not required. In these cases a minimum pixel surface size is still required. This is due to the fact that the pixel antenna has to accommodate resonant modes over the whole frequency range. In general the length of the resonant paths have to be half the effective wavelength for the most restrictive frequency, which is again the lower frequency. Therefore,

$$L_t > \lambda_{\text{low}}/(2\sqrt{\epsilon_{\text{eff}}}) \tag{3.3}$$

where ϵ_{eff} is the effective permittivity of the printed pixel antenna. In any case, the antenna size should be larger than the most limiting value obtained by equations (3.2) and (3.3).

While the total size has to be large enough to meet radiation pattern and frequency requirements, the individual pixel size (L_p) has to be small enough to be able to finely

tune the antenna properties. The main design decision in this case is how small the pixel has to be in order to provide enough control over the synthesized shapes. The pixel size is usually smaller than a tenth of a wavelength for the most limiting frequency, this is

$$L_p < \lambda_{\mathrm{up}}/(10\sqrt{\epsilon_{\mathrm{eff}}}) \tag{3.4}$$

where λ_{up} is the free-space wavelength at the highest frequency of operation. This value results from the analogy between pixel surfaces and space meshes used by electromagnetic simulation methods such are method-of-moments (MoM) or finite-difference time-domain (FDTD). In pixel antennas and surface meshes, the pixel or mesh size has to be small enough so a small perturbation in an individual pixel/cell does not change radically the resulting properties of the antenna. It is well-known that in the previously mentioned methods the maximum size of the mesh is typically between $\lambda/20$ and $\lambda/10$, and as a result this is also the maximum pixel size in antennas. A different approach to decide the pixel size consist on taking the typical thresholds for negligible phase variation and use a pixel size equal to the electrical length corresponding to this phase variation. For instance, when the Fraunhofer distance for far-field is derived a phase variation of $\pi/8$ is considered, which in fact corresponds to an electrical distance of $\lambda/16$ and is in clear agreement with the previously specified pixel size.

Since the minimum total size (L_t) of the pixel antenna is half a wavelength (for the lowest frequency) and the maximum individual pixel size (L_p) is a tenth of a wavelength, it can be directly concluded that pixel antenna require in general at least 5×5 pixels.

It is important to emphasize that all the mentioned dimensions should be taken as a starting point for pixel antenna design and not as physical bounds or definitive dimensions. The optimal dimensions of a pixel antenna can vary significantly depending on the required reconfiguration capabilities and must be determined by a numerical optimization process as is described in the following sections.

3.2.2   Electromagnetic simulation

The electromagnetic simulation of pixel antennas can be performed with the numerical methods typically used for antenna simulation such as method-of-moments (MoM), finite-difference time-domain (FDTD) or finite element method (FEM). Two of the most widespread commercial simulators have been used in this work: Ansys HFSS (High Frequency Structure Simulator) and CST Microwave Studio (Computer Simulation Technology).

From a simulation perspective, the most significant difference between pixel antennas and non-reconfigurable antennas is the presence of RF-switches. Modeling correctly the lumped components is critical for the accuracy of the electromagnetic simulation. In this work four different methods have been followed to include the RF-switches in the electromagnetic simulation.

The first method models the RF-switches as perfect switches by using metal strip or gaps for the ON and OFF state, respectively. This method is only valid for preliminary analysis of the antenna reconfigurability and the accuracy is not acceptable for implementations using real switches. It has been observed that the typical isola-

tion levels of commercially available switches has a severe impact over the antenna properties compared to perfect switches.

The second method applies only to electromechanical switches and consists in modeling the exact geometry of the switch for the ON and OFF states. This technique is time-consuming but provides a good accuracy. It is important to mention that the contact resistance of the switch may be undervalued using this method due to the inability of the mentioned simulators to model the microscopic metal contact physics that determine the contact resistance. Since this method only applies to electromechanical switches, any of the two following methods has to be used for pixel antennas with semiconductor switches.

The third method has been used in the HFSS software and consist in replacing the RF-switches by RLC boundaries. These boundaries simulate a lumped component with a circuit model given by the parallel combination of a resistance, inductance and capacitance. Therefore, this method can be applied regardless of the switch technology as long as an accurate circuit model is extracted for the ON and OFF state of the switch. The accuracy of the circuit model extraction is critical for the overall accuracy of the simulation [106].

The fourth method is based on co-simulation and consists in replacing the RF-switches by internal ports and perform a full-wave simulation to extract the full S-parameter matrix. The pixel antenna properties are computed in a post-processing step by loading the S-parameter matrix with the equivalent impedance of each switch. This method is very accurate and much faster than the other methods when multiple switch configurations have to be simulated for the same structure, as is the case of pixel antennas. A more specific description of this method is presented in section 3.2.5.

3.2.3   Optimization algorithms

Antenna optimization usually refers to the systematic determination of the antenna geometry to suit certain functionalities. In the context of pixel antennas the concept of optimization acquires a new dimension. Optimization is also required to explore the reconfiguration capabilities of the pixel antenna in order to determine the optimal switch configurations for each mode of operation. Due to the large number of switches it is not possible to perform a full exploration of all the configurations, therefore, optimization algorithms are also required to explore in a more or less intelligent manner the space of configurations and determine the optimal ones. Since this is a time-consuming process, the optimization of the pixel antenna geometry is typically based on the design guidelines previously detailed with a few additional optimization steps. From this point forward we will use the expression *optimization* to the process of determining the optimal configurations for each antenna operation mode and as a consequence, the evaluation of the antenna reconfiguration capabilities.

Since the goal of the optimization algorithm is to determine the optimal configurations it is necessary to define the concept of optimality. The optimal configurations are those that maximize a certain *fitness function* which quantifies the antenna performance. The usage of a suitable fitness function is as important as the optimization algorithm itself and depends basically on the target functionality of the pixel antenna. Some examples of useful fitness functions are presented in Table 3.1 for different types

Frequency	Rad. Pattern	Polariz.	Fitness function
✓ (narrowband)			$\left(1-|s_{11}(f_0)|^2\right)$
✓ (narrowband)	✓		$G(\theta_0,\phi_0)\left(1-|s_{11}(f_0)|^2\right)$
✓ (narrowband)	✓	✓	$G(\theta_0,\phi_0)\left(1-|s_{11}(f_0)|^2\right)|\hat{e}\cdot\hat{e}_0^*|^2$
✓ (wideband)			$\min\limits_{|f-f_0|<\mathrm{BW}}\left(1-|s_{11}(f)|^2\right)$
✓ (wideband)	✓		$\min\limits_{|f-f_0|<\mathrm{BW}}G(\theta_0,\phi_0)\left(1-|s_{11}(f_0)|^2\right)$
✓ (wideband)	✓	✓	$\min\limits_{|f-f_0|<\mathrm{BW}}G(\theta_0,\phi_0)\left(1-|s_{11}(f_0)|^2\right)|\hat{e}\cdot\hat{e}_0^*|^2$

Tab. 3.1: Fitness functions used for different types of antenna reconfigurability

of reconfiguration. For frequency reconfigurability a suitable fitness function is the power transmission factor at the central frequency because after the optimization the reflection coefficient will be minimized. For radiation pattern reconfigurability (plus optionally frequency reconfigurability) the realized gain is a good fitness function. Since the realized gain is defined as the antenna gain minus the loss due to mismatch [1], this fitness function leads to maximum gain and minimum reflection coefficient. In the cases where polarization reconfigurability is also considered, the fitness function is the partial realized gain, which is identical to the previous fitness function but including an additional term to account for the polarization mismatch losses. These three fitness functions can be easily extended to antennas operating in wideband conditions by modifying the fitness function to consider the worst in-band transmission coefficient, realized gain and partial realized gain, respectively. The use of multiple fitness functions is also possible by using multi-objective optimization algorithms leading to Pareto optimal solutions, however this multi-objective approach is not covered in this document.

Having defined the optimality criteria, the next step is to decide the optimization algorithm to be used. The optimization space corresponds to the switch configurations and thus only discrete optimization algorithms can be used. These methods have a slower convergence rate that local methods because they can not take advantage of the solution space regularity. On the other hand, they present a better avoidance of local extremes in favor of the global maximum/minimum.

The main discrete optimization algorithms are Random Walk (RW), Simulated Annealing (SA), Genetic Algorithm (GA), Particle Swarm Optimization (PSO) and Ant Colony Optimization (ACO). These algorithms mimic optimization processes found in nature. Random Walk is the simplest, has no memory and consist on exploring randomly the configuration space. The other four methods are of course more complex and present a certain balance between the preservation of the acquired knowledge and the exploration capability. Simulated Annealing emulates heating and cooling
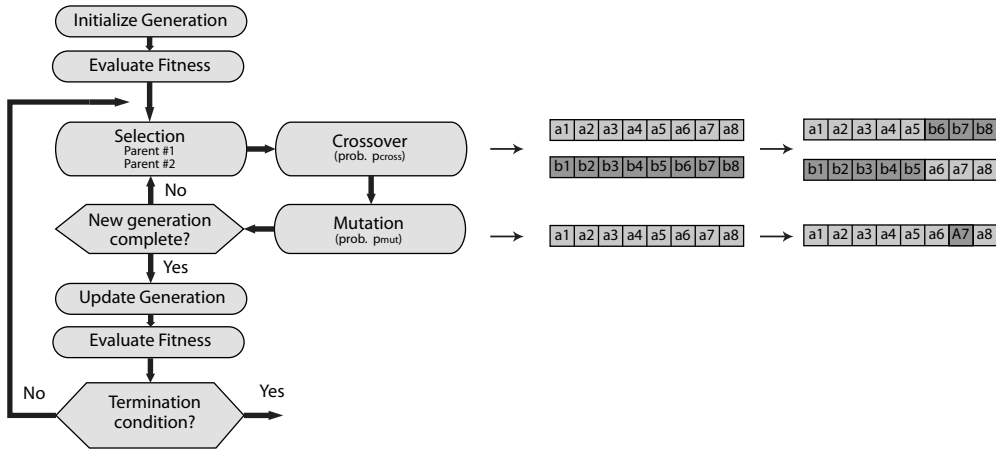
Fig. 3.4: Flow diagram of a Genetic Algorithm and conceptual representation of the crossover/mutation processes.

processes, Genetic Algorithms imitates the natural evolution of species, Particle Swarm Optimization and Ant Colony Optimization mimic the movement of particle swarms and ant colonies, respectively.

All these methods have been successfully used in electromagnetic optimization problems [107]. Genetic algorithm is the most extensively used among them and has been applied for a wide variety of EM problems providing a good trade-off between convergence speed and avoidance of local maximums [108] and is the one that has been used in this work. The flow diagram of the algorithm is represented in Fig. 3.4. The algorithm is initialized with a set of random switch configurations, called generation 1. The next generations are created by iterating the processes of selection, crossover and mutation. The selection process picks a pair of configurations from generation 1 giving a higher selection probability to those configurations with higher fitness. The crossover process combines with a certain probability the two configurations and the mutation process introduces minor perturbations to the two new configurations. Since generation 2 is created by selecting with higher probability those configurations from generation 1 with higher fitness, a certain increase in the overall fitness of the generation is expected. Iterating this process produces evolved generations with an increasing fitness level. The probabilities controlling the selection, crossover and mutation are used to balance the preservation of the acquired knowledge and the exploration of new configurations.

It is important to notice that the genetic optimization of pixel antennas requires the evaluation of the configuration fitness for all the configurations in each generation. Therefore, the genetic optimization is combined with electromagnetic simulations. In this doctoral work two different approaches have been followed to combine the optimization and simulations process and are described in the subsequent sections.
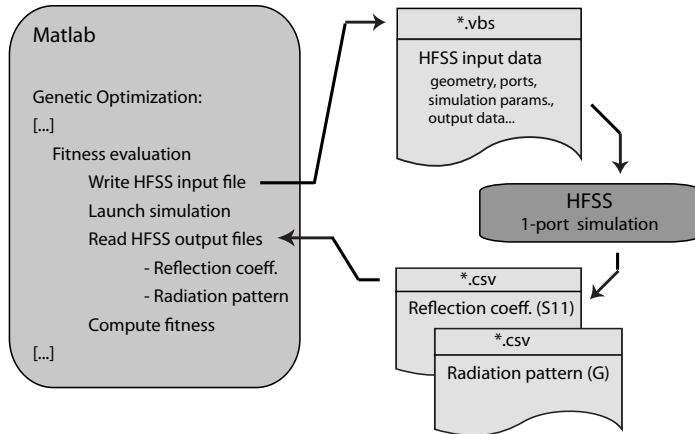
Fig. 3.5: Genetic algorithm implementation combining Matlab and HFSS based on multiple fullwave simulations.

3.2.4 Full-wave optimization

The first implementation of the genetic optimization combines Matlab and HFSS and is based on the scripting tools of HFSS. The flow of the optimization implementation is represented in Fig. 3.5. The genetic algorithm is implemented in Matlab and every time that a fitness calculation is required, a full-wave simulation is launched in HFSS. To perform this simulation, the Matlab program creates a Visual Basic Script (VBS) including all the instructions to create the antenna geometry, feeding ports, simulation parameters and output reports, which serves as an input file for the full-wave simulation. In particular, these instructions include all the physical or electrical modifications required to model the specific switch configuration. Once the simulation is completed two files with Comma-Separated Value (CSV) format are generated with the reflection coefficient and radiation pattern data. These files are read by the Matlab program and the optimization is resumed.

This implementation is relatively simple and very flexible. Since the antenna simulation model is created by the Matlab code it is even possible to dynamically optimize the antenna dimensions depending on the results of the optimization. The main disadvantage is the time consumption. Since an independent full-wave simulation is required for each fitness evaluation, the optimization process usually takes several tents of hours.

3.2.5 Port-Loading Optimization

The key in reducing the optimization time is the avoidance of performing a full-wave simulation for each fitness evaluation. This can be done by using the port loading technique, which requires an initial full-wave simulation and all the subsequent fitness evaluations can be performed by a much faster post-processing step [16, 109].

The flow of the port-loading implementation is represented in Fig. 3.6. The pro-
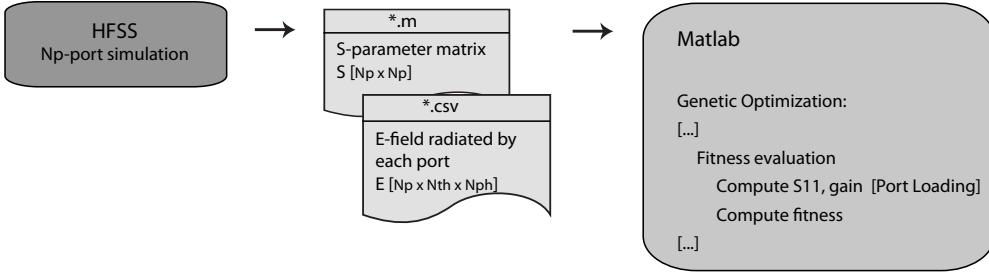
Fig. 3.6: Genetic algorithm implementation combining Matlab and HFSS based on port-loading.

cess starts with a single full-wave simulation of the pixel antenna. In this case, all the switches in the simulation model have been replaced by internal ports. Therefore, the number of ports in this simulation is equal to number of switches plus one. The full S-parameter matrix and the electric field radiated by each port is extracted after completing the simulation. Then, the Matlab optimization code runs the genetic optimization. Every time that a fitness evaluation is required, the reflection coefficient and radiation pattern of the antenna is computed numerically by loading the switch internal ports with the required ON/OFF switch impedances. Since this post-processing step only require low-complexity computations, the total optimization time is usually less than one hour including the initial full-wave simulation.

The post-processing equations are now derived for a general case with an arbitrary number of antenna ports and switches. Let N_A be the number of antenna ports, usually equal to one for single antenna and greater than one for multi-antenna systems. Let N_B be the number of internal ports corresponding to switches. Following the standard notation we represent the incident and reflected power waves by a and b, respectively. The incident and reflected power waves are related by the S-parameter matrix, which can be split in antenna ports and switch ports as follows

$$\begin{bmatrix} b_A \\ b_B \end{bmatrix} = \begin{bmatrix} S_{AA} & S_{AB} \\ S_{BA} & S_{BB} \end{bmatrix} \begin{bmatrix} a_A \\ a_B \end{bmatrix}. \tag{3.5}$$

Let Γ_B be a diagonal matrix whose diagonal elements are equal to the reflection coefficient at each switch port, which would be different for each switch configuration and can be computed taking into account the ON/OFF impedance of each switch. At the switch ports the incident and reflected wave are related by the following expression

$$a_B = \Gamma_{BB} b_B \tag{3.6}$$

Combining equations (3.5) and (3.6)

$$a_B = \Gamma_{BB} (S_{BA} a_A + S_{BB} a_B) = (I - \Gamma_{BB} S_{BB})^{-1} \Gamma_{BB} S_{BA} a_A \tag{3.7}$$

Now, combining (3.5) and (3.7)

$$\begin{aligned} b_A &= S_{AA} a_A + S_{AB} (I - \Gamma_{BB} S_{BB})^{-1} \Gamma_{BB} S_{BA} a_A \\ &= \left[S_{AA} + S_{AB} (I - \Gamma_{BB} S_{BB})^{-1} \Gamma_{BB} S_{BA} \right] a_A \end{aligned} \tag{3.8}$$

Since the previous equation is a direct relation between the incident and reflected waves at the antenna ports, the S-matrix of the loaded multiport is equal to

$$S_{\mathrm{L}} = S_{\mathrm{AA}} + S_{\mathrm{AB}} \left(I - \Gamma_{\mathrm{BB}} S_{\mathrm{BB}} \right)^{-1} \Gamma_{\mathrm{BB}} S_{\mathrm{BA}} \tag{3.9}$$

In particular, this equation allows to compute the reflection coefficient of a pixel antenna from the full S-parameter matrix and the reflection coefficients corresponding to the switch configuration.

It is also possible to compute the radiation pattern of the antenna structure given the incident wave at each antenna port and the switch configuration. Let $\vec{E}_i$ be the radiated field by the port i, then the total radiated field can be computed by superposition weighting the radiated field of each port by the incident wave at the same port

$$\vec{E} = \sum_{i=1}^{N_{\mathrm{A}}+N_{\mathrm{B}}} a_i \vec{E}_i = \sum_{i=1}^{N_{\mathrm{A}}} a_{\mathrm{A},i} \vec{E}_{\mathrm{A},i} + \sum_{i=1}^{N_{\mathrm{B}}} a_{\mathrm{B},i} \vec{E}_{\mathrm{B},i} \tag{3.10}$$

Given a specific excitation vector a_{A}, the incident waves a_{B} at the switch ports can be computed by equation (3.7) and the resulting radiation pattern can be evaluated with expression (3.10).

Taking into account the previous expressions it is possible to compute numerically the pixel antenna reflection coefficient, directivity, gain, polarization or any other parameter required in the fitness evaluation without requiring further full-wave simulations.

3.3   MULTI-SIZE PIXEL ANTENNA

This section presents the first of the two main contributions of this doctoral work regarding the design of pixel antennas. A novel geometry is presented which reduces the number of switches in a factor 10 compared to usual pixel antenna designs preserving a rich compound reconfiguration. This reduction in the number of switches has important advantages regarding the antenna cost, complexity, efficiency and reconfiguration speed. The key concept to reduce the number of switches is the use of multiple-sized pixels.[1]

3.3.1   Switch reduction using multi-size pixels

Pixel apertures are the antenna structures with highest reconfiguration capability, however their implementation is still very limited due to the large number of required switches. Even for low-loss switches, the antenna efficiency drops easily below 50% due to their serial concatenation. The cost is strongly affected by the large number of high-quality switches required, together with complex biasing networks and control circuitry. Additionally, the antenna response to environmental changes is slowed due to the additional variables in the real-time reconfiguration algorithms. Therefore, the

---

[1]This section includes figures and text fragments, sometimes verbatim, from references [JA7], [JA10] and [CA8].

(a) Uniform Pixel Aperture

(b) Bi-clustered Pixel Aperture

(c) Multi-size Pixel Aperture

(d) Low-complexity Pixel Aperture
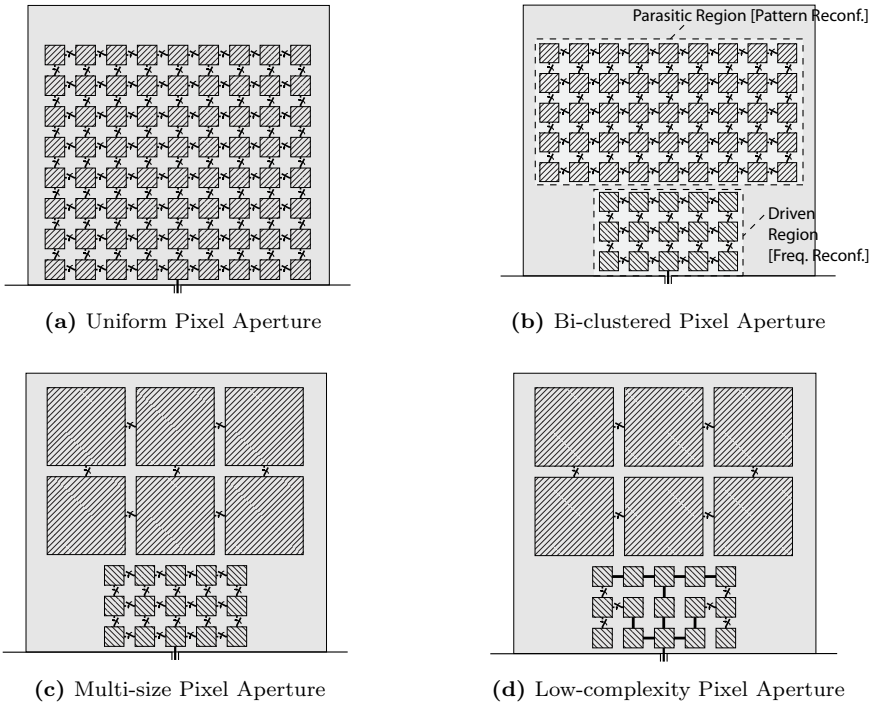
Fig. 3.7: Pixel geometry optimization, from high-complexity uniform pixel antennas to low-complexity multi-size pixel apertures.

future of pixel apertures lies on the switch number reduction in order to improve the antenna efficiency, cost and reconfiguration speed.

The common geometry of pixel antennas is a uniform grid of small metallic patches with switches between every pair of adjacent patches as depicted in Fig. 3.7a. However, uniform pixelation is a suboptimal geometry in terms of complexity because the contribution of each pixel to the antenna reconfigurability is not uniform. Pixels and switches located close to the RF-port have a much stronger influence over the antenna input impedance than those at further locations. The following paragraphs exploit this phenomenon to develop a three-step modification process to maximize reconfiguration properties while minimizing the number of necessary switches.

The first modification mitigates the interdependence between the different antenna parameters by dividing the antenna surface in a driven and a parasitic region, as depicted in Fig. 3.7b. The idea is to locate different reconfiguration functionalities on different aperture regions: the near-port region affects mainly the input impedance, while the parasitic region affects basically the radiation pattern. The parasitic region requires a physical area significantly larger than the driven area to dominate the antenna pattern. This modification does not intend to achieve a perfect division of functionalities, which is not possible due to the closeness of the two regions.

The second modification is illustrated in Fig. 3.7c and takes advantage of the previous division by introducing multiple sized pixels. The antenna driven region requires a dens grid of small patches due to the sensitivity of the input impedance respect near-feed modifications. On the other hand, radiation pattern depends on the overall current distribution, making convenient the use of larger pixels to cover the parasitic region. The result is a large area covered by larger pixels than in uniform pixel apertures leading to a substantial switch reduction of up to a 70% as in the example on Fig. 3.7c. This multi-size pixel technique can be also understood as an equalization of the switch contribution to antenna reconfiguration. While in uniform pixel apertures the switch contribution to the antenna reconfiguration decreases with its distance to the RF-port; in multi-size pixel apertures this contribution is equalized by forcing far switches to operate between larger patches.

The third and final modification addresses the determination of switch locations. Traditionally, pixel apertures include switches between every pair of adjacent patches. However, when the goal is to minimize complexity, it is convenient to remove those of them that contribute less to the antenna reconfigurability as shown in Fig. 3.7d. One effective procedure consist in optimizing a fully switched model for different frequency and radiation requirements and substitute the switches with a less variable state by wires or gaps depending on the predominant state. This is particularly useful for switches located close to the input port. By forcing some near-port interconnections, the average configuration matching can be increased and the number of switches reduced.

This technique is compatible with many different antenna architectures. Some conceptual examples are presented in Fig. 3.8 for monopole, patch and dipole architectures. As can be seen in the previous figure the application of the multi-size technique is similar for all the cases, using a fine grid of small pixel near the RF-port and a coarse grid of large pixel for the antenna regions further from the RF-port. The following sections present specific designs for a multi-size pixel monopole and a multi-size pixel dipole, respectively.

3.3.2 Multi-size pixel monopole

The modifications described in the previous section are applied to a monopole architecture leading to the multi-size pixel monopole presented in Fig. 3.9. The prototype is designed to provide simultaneous pattern and frequency reconfiguration operating at a central frequency of 5.5 GHz.

The antenna consists of a $\lambda/2$ by $\lambda/2$ surface composed of multiple-sized pixels divided in a driven and a parasitic region. The driven region has a high density of pixels with dimensions below $\lambda/20$. Its height is intentionally shorter than a quarter-wave monopole in order to enable strong horizontal currents which intensify the coupled currents over the parasitic area. This parasitic region is composed of larger pixels with dimensions of 0.15λ and, in order to strongly influence the antenna pattern, it is designed to cover almost four times the area of the driven region.

RF-switches have been implemented in the simulation model using RF-MEMS technology. The exact MEMS geometry of a monolithically-integrated cantilever switch has been used in the model. The MEMS switch provides an insertion loss of 0.1 dB

(a) Planar Monopole

(b) Printed Patch

(c) Planar Dipole
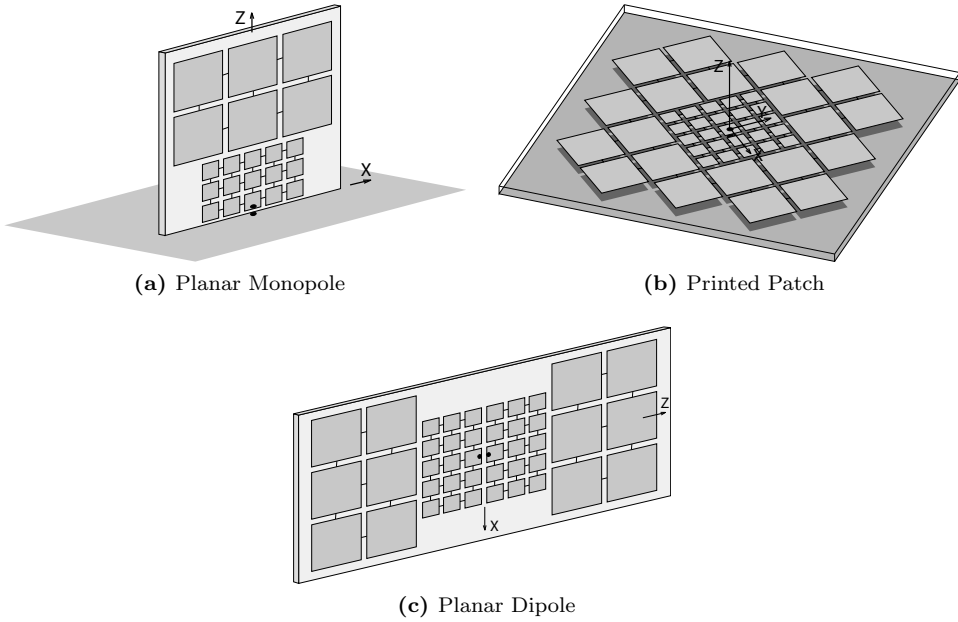
Fig. 3.8: Application of the multi-size pixel technique to different antenna architectures.

(a) Realistic view

(b) Conceptual view

Fig. 3.9: Multi-size pixel monopole with simultaneous frequency and pattern reconfigurability ($w = 40$, $h = 30$, $p_l = 7$, $p_s = 2.4$, $p_g = 0.8$, quartz substrate 0.5mm) [units in mm].

and an isolation of 20 dB.

To determine which switches will be replaced by gaps or metal strips in the prototype, a fully switched model with switches between each pair of adjacent pixels

	Resonance Frequency			Radiation Pattern			
	4 GHz	5 GHz	6 GHz	-60°	-30°	30°	60°
S_1	0	1	0	0	1	0	0
S_2	0	0	1	0	0	1	1
S_3	0	1	0	1	0	0	0
S_4	0	0	0	0	0	1	0
S_5	1	0	1	0	1	0	1
S_6	1	0	0	1	1	1	1
S_7	1	1	1	0	1	0	0
S_8	1	1	0	0	0	0	1
S_9	1	1	0	1	1	1	1
S_{10}	1	0	1	0	1	1	1
S_{11}	1	0	1	0	0	1	1
S_{12}	0	1	1	1	1	0	0

Tab. 3.2: Fitness functions used for different types of antenna reconfigurability

has been optimized for different directions of arrival at the central frequency. The optimization objective has consisted on the maximization of the realized gain, which includes mismatch losses. By using this optimization goal the directivity of the antenna towards each specific angular direction is maximized and simultaneously, the reflection coefficient at the central frequency is minimized. The optimization process has been performed using a genetic algorithm in combination with full-wave FEM simulations. The implementation consisted on a custom-coded optimization algorithm running over Matlab and using Visual Basic scripting to launch the multiple required simulations with the commercial software HFSS. Switches have been included in the simulation model using RLC boundaries with the corresponding ON-OFF state circuit values. The set of optimized configurations has been analyzed and switches with a clear predominant ON or OFF state have been replaced by a metal strip and a gap respectively. This information has been used also to decide about the near-port interconnections. The optimized design has required only 12 switches equally distributed between the driven and the parasitic region as shown in Fig. 3.9.

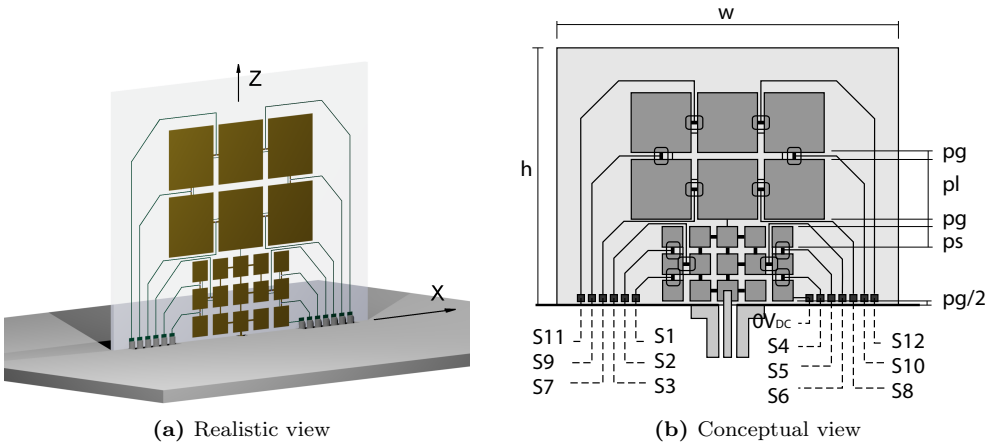An additional advantage of the previous switch allocation is the simplification of the biasing network, which can be accommodated in the same layer as the pixel surface avoiding the use of vias. The complete pixel surface is interconnected through high-resistivity lines which do not affect the RF-currents and allows to bias the RF-MEMS using 13 lines (12 switches and 1 DC-ground). Additionally, biasing lines are designed to cross the ground plane, what permits locating the switch control circuitry below the ground plane, thus minimizing undesired coupling.

The multi-size pixel monopole antenna has been optimized to provide simultaneous reconfigurability in frequency and radiation pattern. In Fig. 3.10 and Fig. 3.11 the results corresponding radiation pattern and frequency reconfiguration are respectively represented. The switch status for the optimal configurations are presented in Table 3.2

Four different directions-of-arrival over the XZ plane corresponding to the angles

(a)

(b)
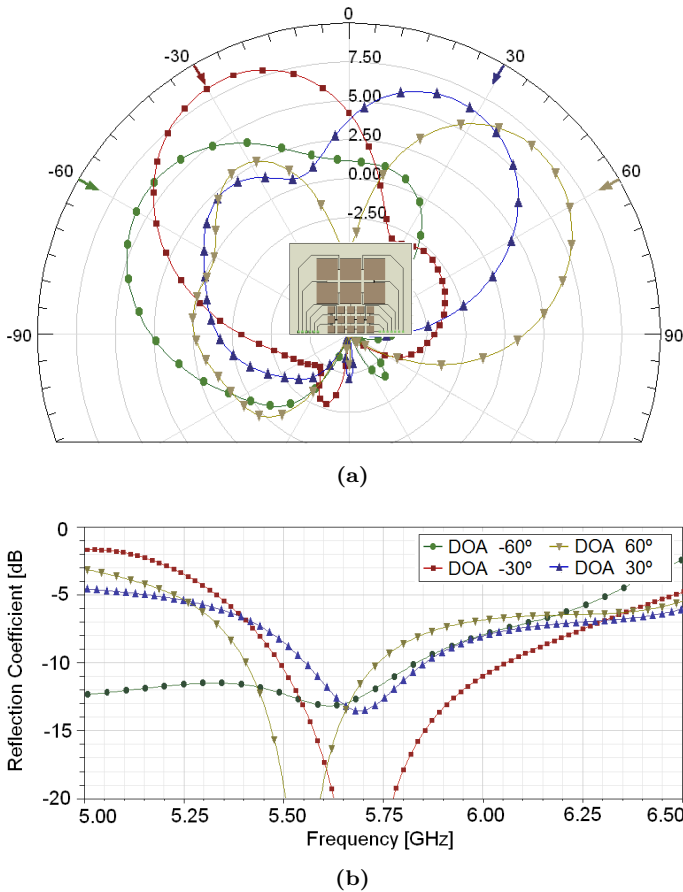
Fig. 3.10: Pattern reconfigurability of the multi-size pixel monopole.

$\theta = -60^{\circ},\ -30^{\circ},\ 30^{\circ},\ 60^{\circ}$ have been considered. The antenna configurations have been optimized to maximize the realized gain in each specific direction. As shown in Fig. 3.10a, the optimized configurations are clearly steered toward the corresponding directions achieving a gain of approximately 7 dB. These four configurations present also a low reflection coefficient at the central frequency of 5.5 GHz as can be observed in Fig. 3.10b.

The antenna has been also optimized to reconfigure its operating frequency switching from 4 GHz, 5 GHz and 6 GHz. The reflection coefficient of each configuration is represented in Fig. 3.11a. As expected the antenna resonances are centered at the corresponding frequencies covering a frequency range from 3 GHz to 6 GHz. The radiation pattern shape is almost equal for the three operating modes as shown in Fig. 3.11b.

The results presented show that the multi-size pixel monopole is able to tune its resonance frequency while keeping a constant radiation pattern, and independently, to steer its radiation pattern keeping a good matching. The multi-size pixel monopole
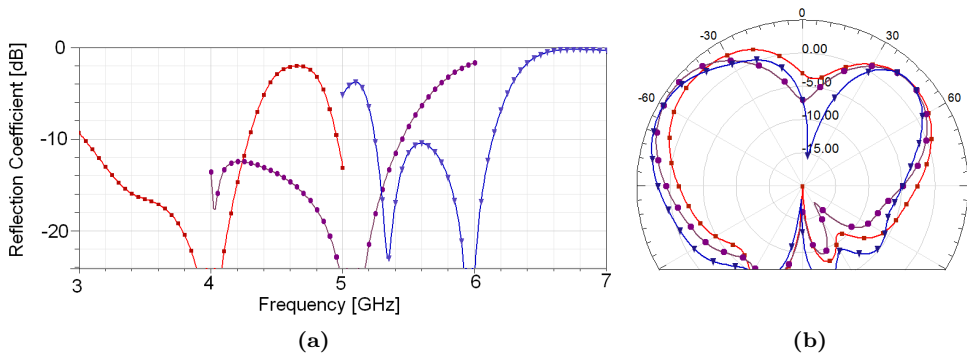
Fig. 3.11: Frequency reconfigurability of the multi-size pixel monopole.
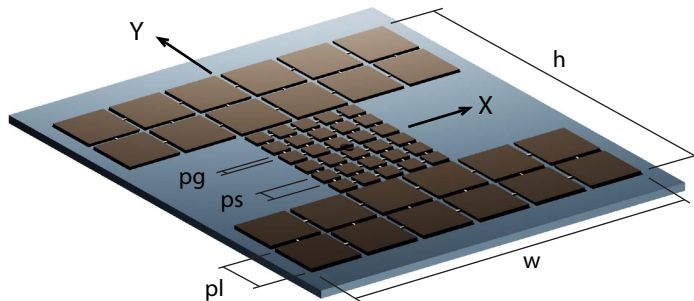
Fig. 3.12: Multi-size pixel dipole with simultaneous beam-steering and beamwidth reconfiguration ($w = 46$, $h = 49.6$, $p_l = 7$, $p_s = 2.4$, $p_g = 0.8$, quartz substrate 0.5mm) [units in mm].

is also able to tune simultaneously its operating frequency and radiation pattern, meaning that the antenna is able to produce different radiation patterns for several different operating frequencies. These reconfiguration capabilities have been fully analyzed from an experimental perspective showing that the antenna is able to steer its radiation pattern for a variable frequency changing over a 1:6 frequency range. The full results can be found in the chapter corresponding to prototyping and characterization, more specifically in section 5.1.

3.3.3 Multi-size pixel dipole

The multi-size pixel monopole can be easily transformed into a pixel dipole by removing the ground plane and doubling the monopole geometry to form the two arms of the dipole. The multi-size pixel antenna is represented in Fig. 3.12. The parasitic region of the pixel dipole has been redesigned to occupy a larger area in order to meet gain requirements of 7 dB. In this case, a fully switched design has been considered.

The multi-size pixel dipole has been optimized to provide simultaneous reconfiguration of the steering angle and beamwidth. The antenna has two main operating

(a) 4-beam, $\theta_0 = 45°$ **(b)** 8-beam, $\theta_0 = 0°$ **(c)** 8-beam, $\theta_0 = 45°$ **(d)** 8-beam, $\theta_0 = 90°$
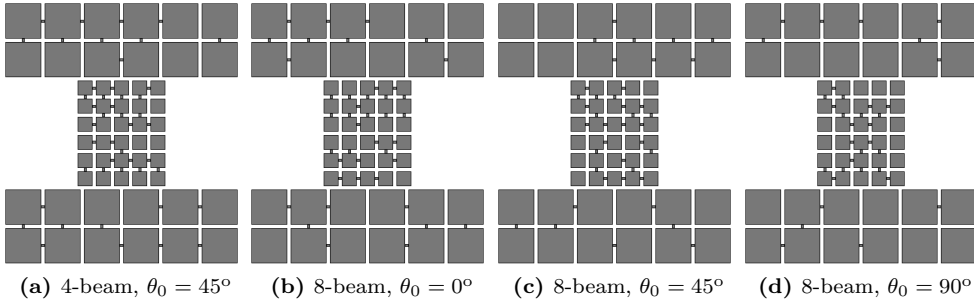
Fig. 3.13: Optimal configurations of the multi-size pixel dipole.

modes. The first operating mode provides a 5 dB gain, with a beamwidth of 90° and four possible directions-of-arrival $\theta = \{45°, 135°, -135°, -45°\}$. The second operating mode provides a 8 dB gain, with a beamwidth of 45° and eight possible directions-of-arrival $\theta = \{0°, 45°, 90°, 135°, 180°, -135°, -90°, -45°\}$.

The fitness function used in the optimization has been modified to take into account the antenna beamwidth. The specific fitness function to be maximized is

$$\min_{|\theta-\theta_0|\leq\Delta\theta/2} G(\theta) - T(\theta) \tag{3.11}$$

where θ_0 is the direction-of-arrival, $\Delta\theta$ is the required beamwidth $\{45°, 90°\}$, $G(\theta)$ is the antenna realized gain and $T(\theta)$ is a 3 dB linear taper used to conform the pattern shape.

As seen in Fig. 3.12, the geometry of the multi-size pixel dipole is symmetrical along X and Y axes. This implies that by applying an X or Y symmetry to the optimal switch configuration for a given direction, we obtain the optimal configuration for the corresponding symmetric direction. Due to the symmetric geometry, there is one basic configuration for the 4-beam MRA from which the other three configurations can be determined by applying the symmetry transformations. Similarly, there are three basic configurations for the 8-beam MRA, and the rest can be obtained from these. The basic reconfigurable modes of operation and the corresponding status of all interconnecting switches for the 4-beam and 8-beam MRA dipole are provided in Fig. 3.13. The radiation patterns of the different switch configurations corresponding to 4-beam and 8-beam designs at 5.5 GHz are presented in Fig. 3.14. The application of X- and Y-symmetries is clearly reflected in the radiation patterns of the 4-beam MRA, as shown in Fig. 3.14a. Fig. 3.14b shows only the three basic radiation patterns of the 8-beam MRA for the sake of clarity. As indicated, the other five patterns are obtained by applying X/Y symmetries. In both cases, the radiation patterns have the required -3 dB-beamwidth of approximately 90° and 45° for 4-beam and 8-beam case, respectively. The directivity is approximately 7 dB for both cases and the reflection coefficient is below -9 dB for all the configurations.

(a) 4-beam, 90° beamwidth   **(b)** 8-beam, 45° beamwidth
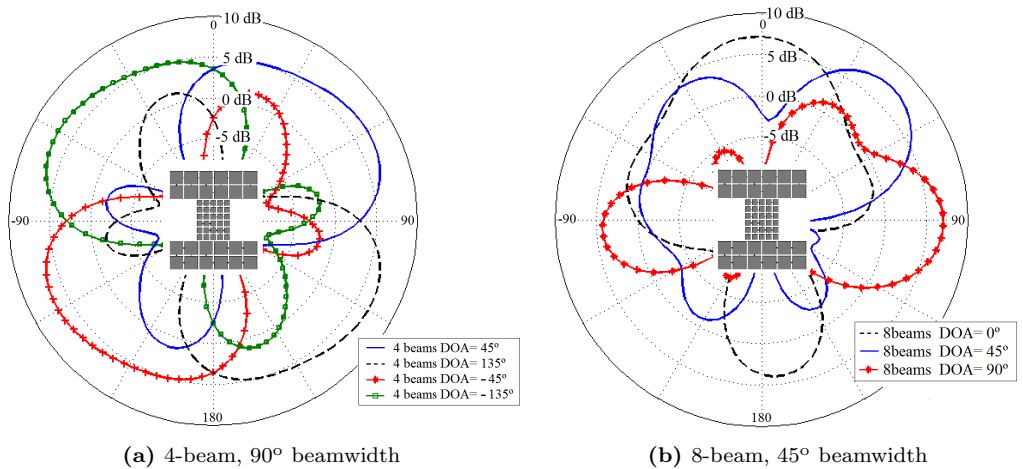
Fig. 3.14: Radiation patterns of the multi-size pixel dipole corresponding to different angular directions and beamwidths.

3.4   PARASITIC PIXEL ANTENNA

This section presents the second of the two main antenna geometry contributions of this doctoral work regarding the design of pixel antennas. Unlike the previous section which explored new pixel geometries, this section focuses on new conceptual pixel architectures. The traditional active nature of pixel antennas is here abandoned and a new architecture is proposed where the pixel layer has a purely parasitic behavior. This approach allows to add reconfiguration capabilities to existing antennas and has clear advantages from fabrication, integration and biasing perspectives.[2]

3.4.1   Parasitic pixel layer

The usual approach followed by pixel antennas consists in pixelating the antenna active surface as depicted in Fig. 3.15a. However, in this approach the antenna has to be completely redesigned taking into account the effects of the switches along with the associated biasing network, whose allocation is often difficult.

   The strategy proposed in this section approaches the pixelation from a very different perspective, which leads to significant advantages. Instead of replacing the original antenna, the antenna is kept unmodified and reconfiguration capabilities are provided by an external parasitic pixel layer, which is separated from the driven antenna as shown in Fig. 3.15b. This approach takes advantage of existing antenna designs and is compatible with a wide variety of antenna architectures. In Fig. 3.16 it is shown a conceptual representation of different pixel parasitic layers adapted to unidirectional, omnidirectional and bidirectional antennas using rectangular, cylindrical and circular geometries, respectively.

---

[2]This section includes figures and text fragments, sometimes verbatim, from reference [CA5].
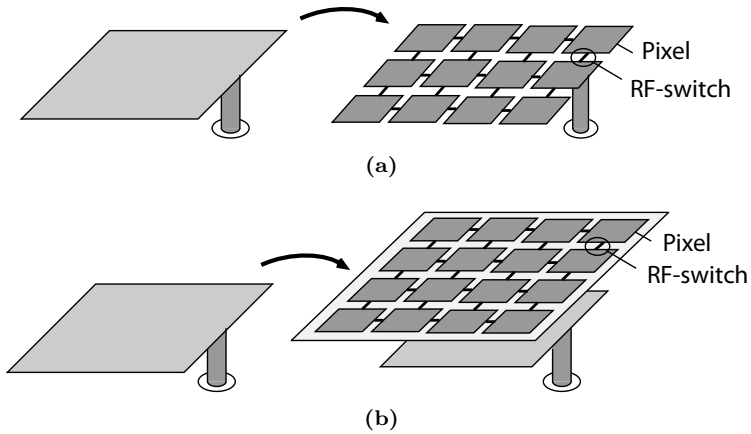
Fig. 3.15: Comparison between (a) the standard approach followed by pixel antennas where the active surface is pixelated and (b) a novel approach where the pixel layer is used as a parasitic surface.
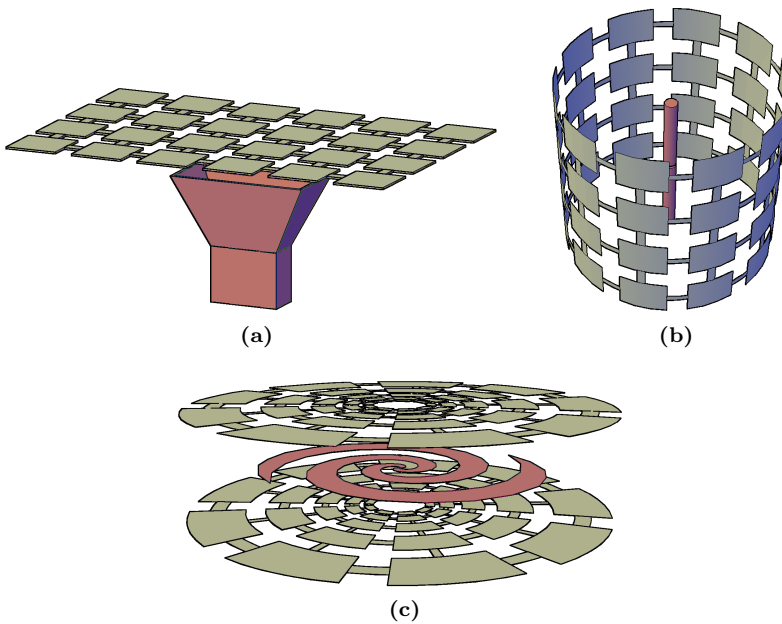
Fig. 3.16: Parasitic pixel layer geometry adapted to conventional radiating structures such as (a) unidirectional, (b) omnidirectional and (c) bidirectional antennas.

The parasitic nature of the pixel layer proposed has clear advantages compared to conventional pixel antennas. The design of the switch biasing network is simplified since all biasing lines can be allocated in the back side of the pixel layer substrate
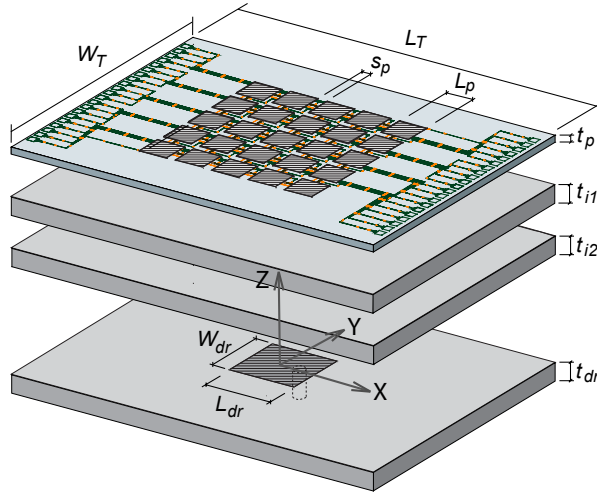
Fig. 3.17: Patch reconfigurable antenna using a parasitic pixel layer ($L_{dr} = 9.15$, $L_P = 3.0$, $L_T = 40.0$, $W_{dr} = 8.0$, $W_T = 30.0$, $t_{dr} = t_{i1} = t_{i2} = 1.575$, $t_p = 1.0$, $s_p = 1.0$) [units in mm]

independently of the active antenna architecture. Due to the parasitic behavior of the pixel layer, the power handling requirements for the switches are relaxed and consequently non-linear effects are reduced. Additionally, the pixel layer is highly integrable due to its planar shape and the lack of physical interconnections with the driven antenna. This lack of interconnections also allows the pixel layer to be fabricated with a different technology than that used to fabricate the active antenna. For instance, the active antenna can be fabricated using standard photolithography while the pixel layer is fabricated using microfabrication techniques to integrate MEMS switches.

The parasitic pixel layer allows to reconfigure multiple antenna parameters simultaneously. Since the parasitic layer is located in the reactive field region of the driven antenna, the driven antenna is affected by a significant impedance loading that modifies its resonance frequency. On the other hand, the strong coupling between the driven antenna and the parasitic pixel surface induces significant currents over the pixel layer, therefore affecting the antenna radiation pattern and polarization. As a result, it is possible to simultaneously tune the antenna resonance frequency, radiation pattern and polarization by properly selecting the switch configuration.

3.4.2 Reconfigurable patch with parasitic pixel layer

In this section a microstrip patch has been selected to operate as the driven antenna. Patch antennas, and printed microstrip antennas in general, are particularly well-suited to be used in conjunction with the parasitic pixel surface. The unidirectionality of their radiation pattern permits reconfiguration using a single pixel surface. Additionally, their planar geometry results in low-profile reconfigurable antennas even after the addition of the pixel surface.
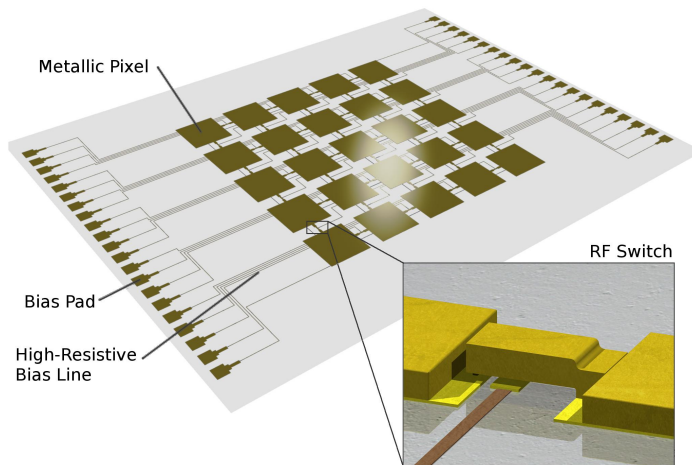
Fig. 3.18: Realistic representation of the 5x5 pixel layer including details of the RF-MEMS switch and the biasing lines.

An schematic of the reconfigurable patch antenna using a parasitic pixel layer is presented if Fig. 3.17. The driven element is a standard patch antenna designed to operate at $10\,\mathrm{GHz}$ using a RT/Duroid 5880 substrate with 1.575mm thickness. The pixel layer is located at a distance of $t_{i1} + t_{i2} + t_p = 4.15$mm from the patch using two intermediate PCBs identical to that of the driven patch. The pixel layer dimensions and the individual pixel size are designed to maximize the coupling with the driven element in order to maximize the reconfiguration capabilities. Therefore, the overall size of the pixel surface is large enough to enable resonant shapes of at least half-wavelength. On the other hand, the size of the individual pixels is small enough to finely tune the dimensions of these resonant shapes. It has been observed that pixel sizes below $\lambda/10$ are sufficient to provide rich reconfigurability. As a result of the pixel layer has 5×5 elements and occupies a physical area of 30×40mm^2 which is compatible with standard microfabrication processes over 4-inch wafers.

The pixel layer is located over a quartz glass substrate with a thickness of 1mm thickness. Quartz glass presents excellent electromagnetical properties ($\epsilon_r = 3.9$, $\tan\delta < 0.0001$ @1GHz, $\tan\delta = 0.0004$ @30GHz [110]) and allows the monolithical integration of RF-MEMS switches [111]. A realistic view of the pixel layer is presented in Fig. 3.18 showing the RF-MEMS switch element and the biasing lines. Details about the RF-MEMS geometry and microfabrication are provided in section 4.2.3

The antenna is optimized to maximize the received power in an scenario with an incoming plane wave with a certain direction of arrival (DOA$_0$) and frequency (f_0), or by reciprocity, to maximize the radiated power for a specific direction and frequency. Therefore, reconfiguration for the described scenario can be formulated as the following discrete optimization problem,

$$\max_{s_j \in \{\mathrm{ON,OFF}\}\ \ j=1..40} G(\theta_{\mathrm{DOA}_0}, \phi_{\mathrm{DOA}_0}, f_0) \tag{3.12}$$

(a) $f_0 = 9\,\text{GHz}$, $\theta_0 = -45°$ **(b)** $f_0 = 9\,\text{GHz}$, $\theta_0 = 0°$ **(c)** $f_0 = 9\,\text{GHz}$, $\theta_0 = 45°$

(d) $f_0 = 10\,\text{GHz}$, $\theta_0 = -45°$ **(e)** $f_0 = 10\,\text{GHz}$, $\theta_0 = 0°$ **(f)** $f_0 = 10\,\text{GHz}$, $\theta_0 = 45°$
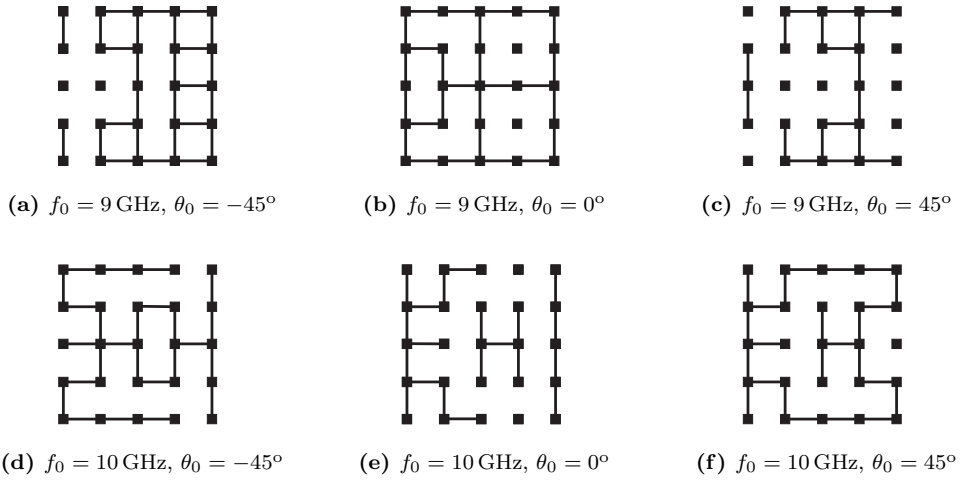
Fig. 3.19: Optimal switch configurations of the 5×5 parasitic pixel layer.

where $\{s_j\}_{j=1..40}$ is the switch configuration and G represents the antenna realized gain including mismatch losses. A genetic optimization (GA) with a population equal to 21 and a 5% mutation probability has been carried out to determine the switches optimal configuration for each specific set of parameters. Only symmetrical configurations with respect to XZ plane and directions of arrival over the same plane are considered, thus forcing a linear polarization. Three different directions of arrival $\theta_{\text{DOA}} = -45°$, $0°$, $45°$, $\phi_{\text{DOA}} = 0°$, and two frequencies of operation, $f = 9\,\text{GHz}$, $10\,\text{GHz}$, are considered. The genetically optimized configurations are depicted in Fig. 3.19, where each pixel is represented by a small square and the segments joining different pixels represent ON-sate switches.

The reflection coefficients and radiation patterns of the three configurations operating at 9 GHz are represented in Fig. 3.20. The three configurations are well-matched at the previously specified frequency. To avoid narrowband configurations the fitness function has been modified to consider the worst in-band reflection coefficient. The radiation pattern of these three configuration is clearly steered towards each specified DOAs preserving the gain level and beamwidth. A realized gain of approximately 5 dB is obtained for each direction. Analogous results are presented in Fig. 3.21 for the three optimal configurations corresponding to a central frequency of 10 GHz. Again the configurations are well-matched at the central frequency and the radiation patterns are tilted towards the three specified angular directions having a similar pattern shape than those corresponding to 9 GHz.

Taking into account the previous results it is clear that the presented pixel antenna is reconfigurable in frequency and radiation pattern simultaneously. Other antenna designs tune individually frequency and radiation pattern, that is on one side changing the radiation pattern at a central frequency and, on the other side, shifting the operating frequency while keeping the original radiation pattern. Notice that the

(a)   **(b)**
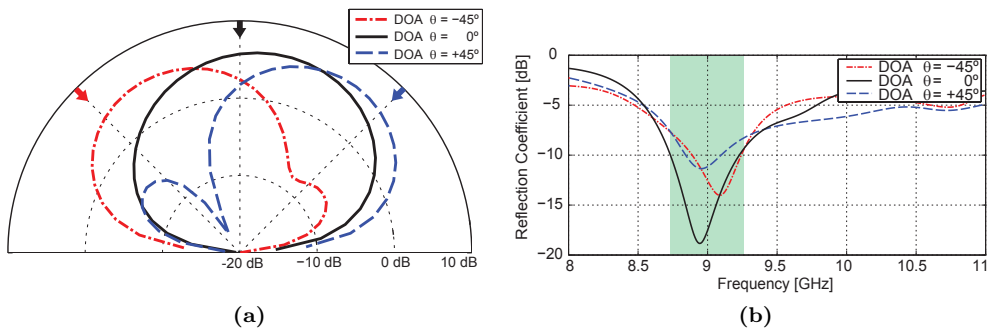
Fig. 3.20: (a) Radiation pattern and (b) reflection coefficient of the three 9 GHz configurations.

(a)   **(b)**
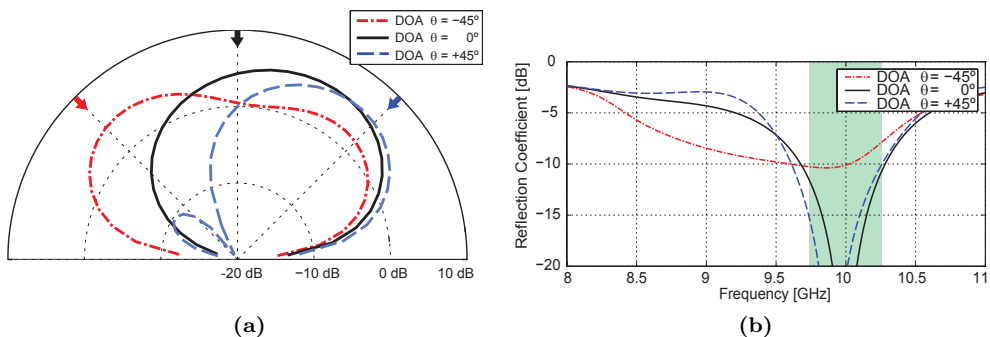
Fig. 3.21: (a) Radiation pattern and (b) reflection coefficient of the three 10 GHz configurations.

reconfigurability here presented overcome the previous capability in the sense that both frequency and radiation pattern can be simultaneously reconfigured covering any combination of central frequency and DOA.

In fact, the presented design is also reconfigurable in polarization. The simultaneous reconfiguration of frequency, radiation pattern and polarization of the parasitic pixel layer in combination with the microstrip patch has been experimentally analyzed in section 5.2. Other important aspects as the effect of the distance between the driven antenna and the parasitic layer are also covered in the mentioned section.

3.4.3   Low-complexity parasitic layer

The previous design showed that the parasitic pixel layer provides high reconfiguration capabilities over multiple antenna parameters. The number of switches used was below one hundred, which in the context of pixel antennas corresponds to a low value. However, in many applications the cost and complexity of such prototype may be excessive, specially those applications that require a lower level of reconfigurability. In this section we present an optimized pixel layer with a very low number of switches and very low-complexity, suitable for wireless applications that require only radiation pat-
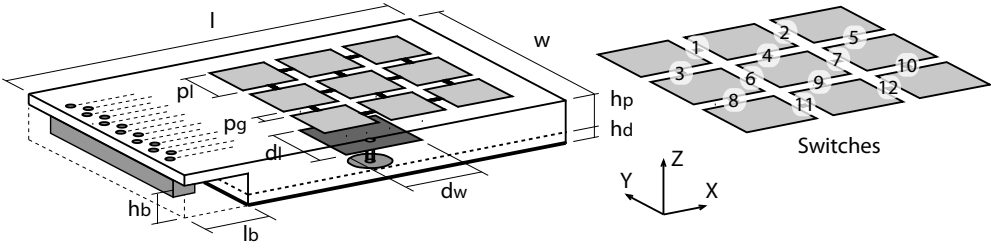
Fig. 3.22: Patch reconfigurable antenna using a low-complexity parasitic pixel layer ($l =$ 60.0, $w = 40.0$, $p_l = 8.5$, $p_g = 2.0$, $d_l = 11.9$, $d_w = 11.9$, $h_p = 4.5$, h_d=1.5, $h_b = 4.5$, $l_b = 10.0$) [units in mm]

tern reconfiguration. The design has been optimized to operate at $5.8\,\mathrm{GHz}$ WiFi band being able to steer the radiation pattern over the E-plane, H-plane and $\pm 45°$-planes. The total number of configurations is nine: one corresponding to broadside radiation plus two additional configurations corresponding to each steering plane.

The present design is based on the same architecture as the previous design consisting in a microstrip patch and a parasitic pixel layer as depicted in Fig. 3.22. PIN-diodes are used to implement the RF-switches, more specifically the diodes used correspond the model Skyworks SMP1345-040LF. An RF-inductance has been located in parallel to each diode to improve the switch isolation at the operating frequency. The inductance is chosen so it resonates with the diode OFF-capacitance at the operating frequency. The biasing lines are oriented orthogonally to the patch polarization and are connected to the flat ribbon connector in the left side. The design has been simulated using HFSS in combination with the port-loading technique described in section 3.2.5 using the ON-OFF circuit models provided by the diode manufacturer. The simulation time required is approximately one hour to simulate the multi-port design in HFSS and a few additional minutes to evaluate the reflection coefficient and radiation pattern for all the switch configurations.

Firstly, the driven patch dimensions are designed to minimize the reflection coefficient in the presence of the pixel layer. Subsequently, the pixel layer dimensions are optimized using the port-loading simulation approach. It has been observed that the nine required configurations can be provided by a low-complexity 3×3 pixel layer. However, in this case the pixel size (p_l), the gap between pixels (p_g) and the distance to the pixel layer (h_p) have to be carefully fine tuned. The optimized dimensions are detailed in Fig. 3.22.

Since an RF-switch is located between each pair of pixels in the 3×3 pixel layer, the total number of switches is only 12. Notice, that this number of switches is one order of magnitude lower than that of common pixel antennas. The optimal switch configurations corresponding to the nine DOAs are specified in Table 3.3. These configurations are determined by exploring exhaustively the complete configuration space, discarding those with a reflection coefficient above $-10\,\mathrm{dB}$ and selecting the ones that maximize the partial realized gain for each DOA.

The radiation pattern of each switch configuration is represented in Fig. 3.23. The representation corresponds to an orthogonal proyection of the spherical space over the

	θ_{DOA}	ϕ_{DOA}	1	2	3	4	5	6	7	8	9	10	11	12
Conf. #1	0º	0º	0	1	0	1	0	0	1	0	1	0	0	0
Conf. #2	0º	0º	0	0	1	1	0	1	0	1	1	0	1	0
Conf. #3	0º	0º	0	0	0	0	0	1	0	1	1	0	1	0
Conf. #4	0º	0º	1	1	0	0	0	1	1	1	1	1	1	1
Conf. #5	0º	0º	0	0	0	0	0	1	0	0	1	1	1	1
Conf. #6	0º	0º	0	0	0	1	1	0	1	0	1	1	0	1
Conf. #7	0º	0º	0	1	0	0	1	1	1	0	0	0	0	0
Conf. #8	0º	0º	1	1	1	1	0	1	1	0	0	1	1	1
Conf. #9	0º	0º	1	1	1	1	0	1	1	0	1	0	0	0

Tab. 3.3: Optimal switch configurations of the low-complexity parasitic pixel layer.

XY plane. This representation has been chosen for the sake of clarity when representing multiple three-dimensional radiation patterns. The contour lines correspond to different gain levels, starting at 7 dB and increasing in steps of one tenth of decibel. The represented values correspond to the antenna partial realized gain, which takes into account the losses due to switch insertion losses, impedance mismatch and polarization mismatch. It can be clearly observed that each radiation pattern is steered toward the required angular direction. The gain levels achieved for the different DOAs are in all cases between 7 dB and 8 dB, which is a moderately high value considering the antenna size. Additionally, the shape and separation of contour lines indicate that the radiation pattern shape and beamwidth is almost identical for the different configurations.

The reflection coefficients of the optimal configurations are represented in Fig. 3.24. As a result of the optimality criteria followed, all the configurations are well-matched at the central frequency (5.8 GHz) with a reflection coefficient lower than −10 dB.

The main conclusion of this section is that the parasitic pixel layer is a good candidate in moderate-complexity high-reconfigurability applications, but also in applications where antennas with low-complexity are required.
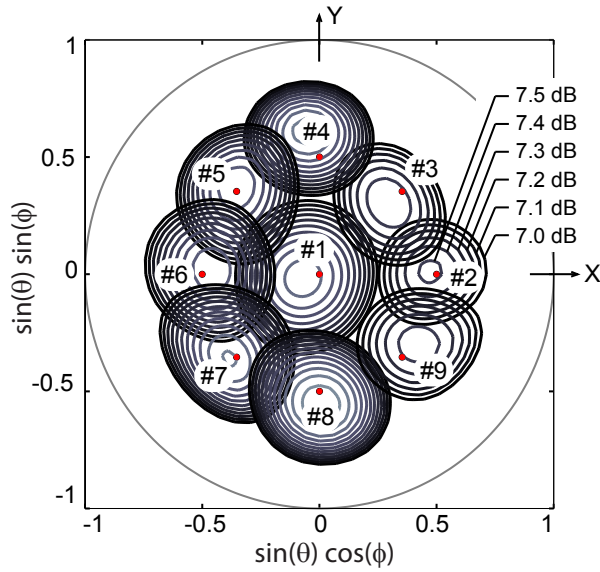
Fig. 3.23: Radiation patterns corresponding to the optimal switch configurations of the low-complexity parasitic pixel layer.
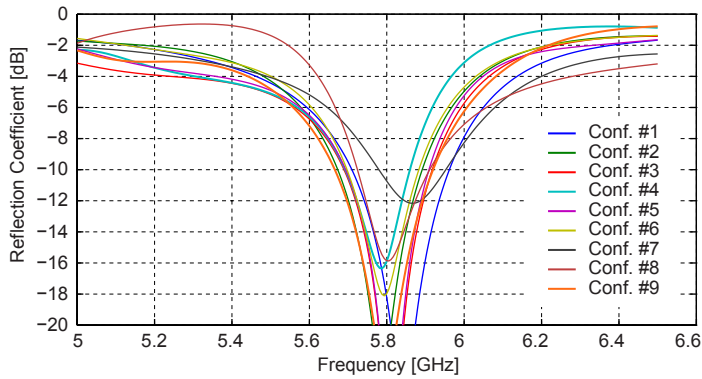

Fig. 3.24: Reflection coefficients corresponding to the optimal switch configurations of the low-complexity parasitic pixel layer.

PIXEL ANTENNA TECHNOLOGY

T ECHNOLOGY plays a key role in the performance of pixel antennas. In particular, the switching element has a drastic influence over the pixel antenna reconfigurability, efficiency, reconfiguration time, cost and power consumption. This section describes the different technological alternatives to implement the switching element. These technologies are described in order of increasing novelty and cover semiconductor, micro-electromechanical and microfluidic technologies.

4.1   SEMICONDUCTOR SWITCHES

Semiconductor switches, such as PIN diodes and FET transistors, are the main switching components used by pixel antennas. They are very good candidates due to their fast switching times (some nanoseconds), low cost (a few cents per device), excellent reliability and compatibility with standard PCB assembly processes. Their insertion loss and isolation levels are acceptable at frequencies up to few gigahertz and their power consumption is in general compatible with wireless communication devices except for highly switched designs under severe power limitations. Semiconductor switches operating at several tens of gigahertz are also commercially available, however beam-lead packaging is used at these frequencies, which rises significantly the device and assembly costs.

The characterization of the switch is an important step to validate its good performance over the frequency range of operation and to ensure the accuracy of the pixel antenna simulations. In Fig. 4.1 it is shown the measured insertion loss and isolation of the PIN diode switch used in some of the pixel antenna designs here presented. The semiconductor switch correspond to the model BAR64-02V from Infineon Technologies. The switch characterization has been performed using calibrated measurements to remove the effects of the microstrip feeding fixture. The insertion loss of the switch for a biasing current higher than $10\,\text{mA}$ is between $0.2\,\text{dB}$ and $0.3\,\text{dB}$ at the central frequency of operation which is $2.5\,\text{GHz}$. The isolation curve shows the typical series-capacitor response where the isolation smoothly decreases with frequency. An isolation level of $12\,\text{dB}$ is obtained at $2.5\,\text{GHz}$ for a reverse voltage of 0V. In the case of pixel antennas it has been observed that isolation levels above $12\,\text{dB}$-$14\,\text{dB}$ provide a reconfiguration level almost identical to that achieved by ideal switches with
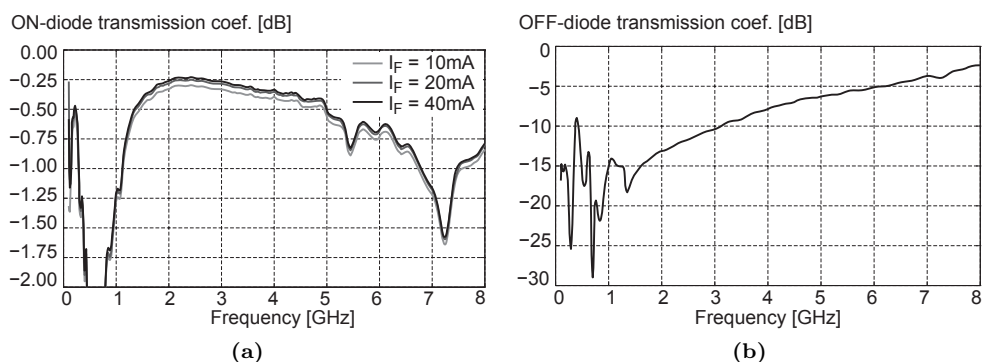
Fig. 4.1: Insertion loss and isolation of the Infineon BAP64-02V diode.
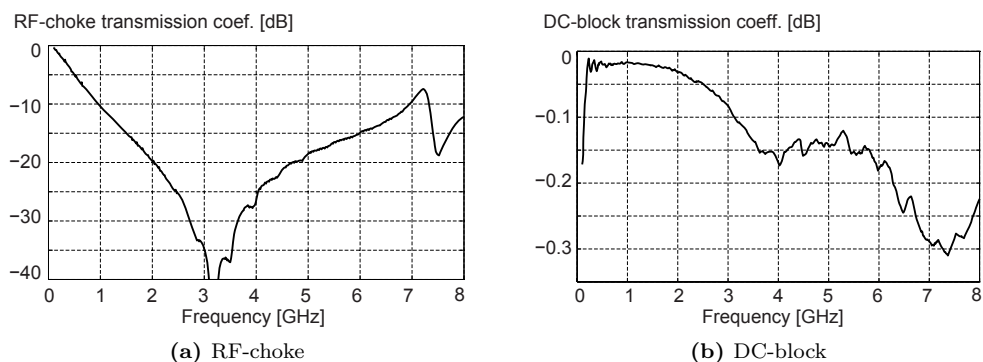
Fig. 4.2: Transmission coefficient of the RF-choke and the DC-block.

perfect-isolation.

The biasing of the PIN diode switch requires additional circuit elements. These additional elements are basically RF-chokes and DC-blocks. The RF-choke consists basically in an inductance that enables the biasing DC-current but prevents RF-currents. RF-chokes are located at the interconnection between the biasing line and the antenna structure to prevent the deviation of antenna currents to the biasing lines. RF-chokes can be also distributed over the biasing lines to minimize the undesired coupling with the antenna structure. The DC-block presents the opposite behaviour than that of the RF-choke, that means that it is a series capacitor that allows RF-currents and blocks the biasing current. DC-block are typically used in series with the PIN diode. It must be mentioned that RF-chokes and DC-blocks present a certain self-resonance frequency due to undesired parasitic effects. It is important to ensure that the self-resonance frequency is not much lower than the frequency of operation.

In Fig. 4.2 the measured transmission coefficients of an RF-choke and DC-block are presented. The RF-choke is an inductor corresponding to the model LQW15A from Murata with a nominal inductance of 47 nH. An isolation level of 25 dB is obtained
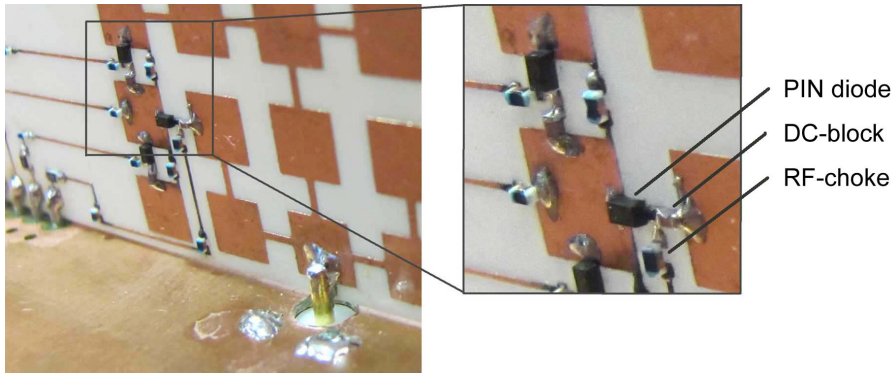
Fig. 4.3: Detail of a pixel antenna prototype showing the PIN diode switches and biasing circuitry.

at $2.5\,\mathrm{GHz}$ and the self-resonance frequency is slightly higher than $3\,\mathrm{GHz}$. The DC-block is a capacitor corresponding to model GRM15 from Murata with a nominal capacitance of $100\,\mathrm{pF}$. The insertion losses of the DC-block are only $0.05\,\mathrm{dB}$ at the frequency of operation.

The typical configuration of the PIN diode switch and the RF-chokes/DC-blocks used in pixel antennas is shown in Fig. 4.3. The PIN-diode and the DC-block are serially interconnected and are located between two adjacent pixels. An RF-choke is located in the interconnection of the biasing line with the diode and DC-block combination. This switch and biasing technique is the one used in the prototypes presented in chapter 5, where a more detailed description of the biasing scheme is provided. The reliability required by the long-run characterizations corresponding to the prototypes in chapter 5 has motivated the choice of PIN diode as reconfiguration element.

4.2 RF-MEMS SWITCHES

4.2.1 RF-MEMS switches for pixel antennas

RF-MEMS technology can enable RF-switches with a superior performance than semiconductor switches in many aspects. RF-MEMS switches have almost zero power consumption, present very low insertion losses and can be monolithically integrated in the antenna structure. These three properties are extremely beneficial for pixel antennas because the required number of switches in pixel antennas is typically larger than in other reconfigurable antenna designs. Indeed, RF-MEMS switches enable switch-integrated pixel antennas with extremely low power consumption and high efficiency. On the other hand, the reliability and robustness of RF-MEMS switches is inferior to that of semiconductor switches.

The structure and principle of operation of a cantilever-type RF-MEMS switch is described in Fig. 4.4. The three main connections of the switch are the drain,

(a) RF-MEMS switch structure

(b) OFF-state

(c) ON-state
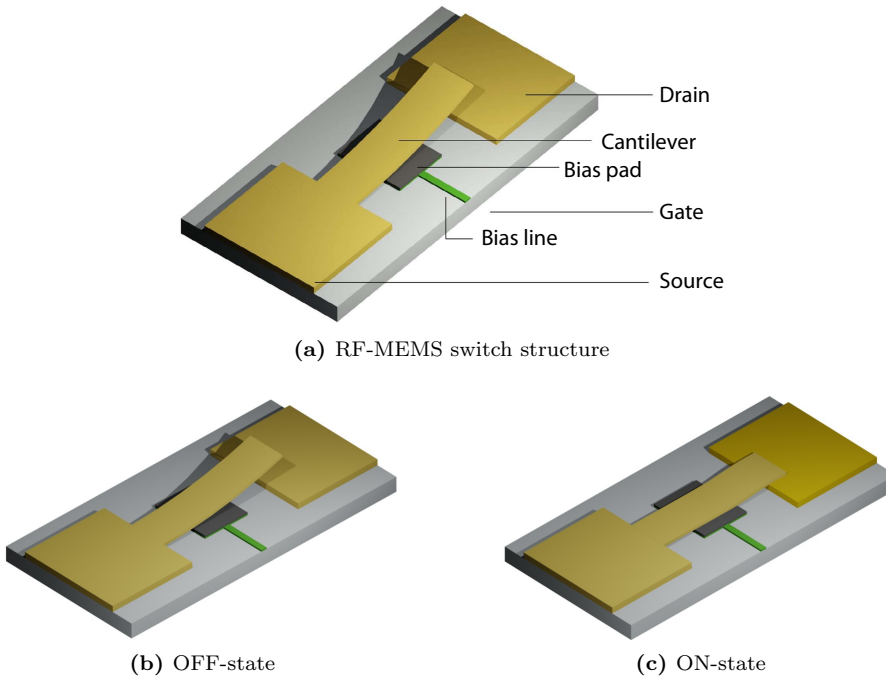
Fig. 4.4: Structure and principle of operation of a cantilever-type RF-MEMS switch.

source and gate which are named after the corresponding connections of semiconductor transistors. The basic part of the switch is the movable cantilever that is anchored on the MEMS source and connects it with the drain depending on its position. To activate the switch a certain voltage is applied between the gate and source, creating an electrostatic field at the bias pad that pulls the cantilever down to establish a physical path between drain and source. The minimum voltage required to activate the switch is named pull-in voltage and is typically between 30 V and 100 V. Since the actuation mechanism is electrostatic, the currents over the bias lines are negligible and so is the power consumption. Due to this zero-current consumption biasing lines can be fabricated using a high-resistivity material that does not prevent the switch actuation and minimizes the coupling between the antenna structure and the biasing lines.

There are different alternatives to model the RF-MEMS switches in simulation software as explained in section 3.2.2. One alternative consists in replacing the switch by an equivalent circuit model. Another alternative is the simulation of the exact switch geometry as presented in Fig. 4.5. In this case the switch isolation is perfectly modeled. However, it is important to mention that the switch contact resistance, which is typically $1\,\Omega$, is related to microscale metal-contact physics and therefore, is underestimated by most simulation softwares.
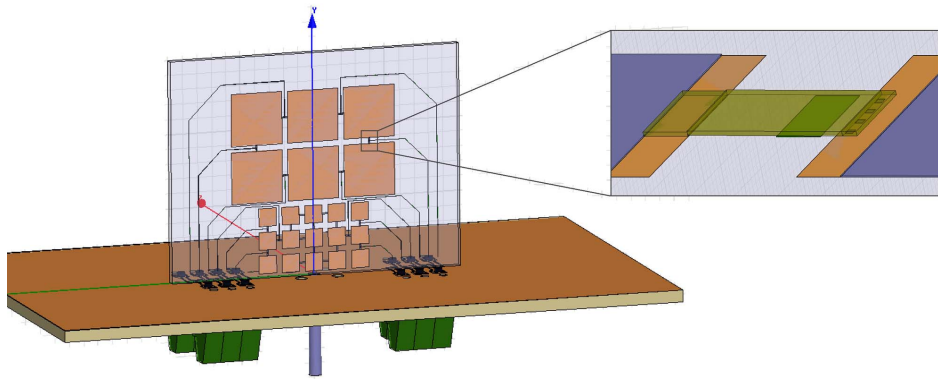
Fig. 4.5: HFSS model of the multi-size pixel monopole where the RF-MEMS switches are modeled using their exact geometry.
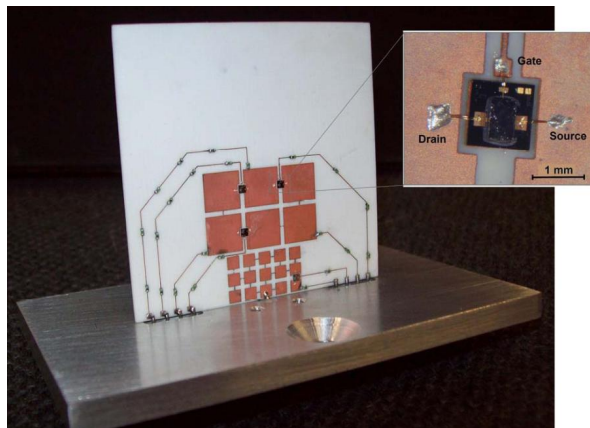
Fig. 4.6: Multi-size pixel monopole with individually packaged Radant MEMS connected using epoxy and wirebonding.

4.2.2 Individually packaged RF-MEMS

Individually packaged RF-MEMS can be used in pixel antennas in a very similar way as done with semiconductor switches. This allows to fabricate the pixel antenna using standard PCB fabrication processes. The RF-MEMS switches are epoxied to the pixel antennas are connected using wire-bonding. A multi-size pixel antenna prototype using individually packaged RF-MEMS switches is presented in Fig. 4.6. The RF-MEMS switch corresponds to the model RMSW100 from Radant MEMS.

The presented prototype corresponds to a preliminary design with four RF-MEMS and two modes of operation producing different radiation patterns. The simulated and measured radiation patterns are presented in Fig. 4.7.

Individually packaged RF-MEMS present a good performance and relatively high
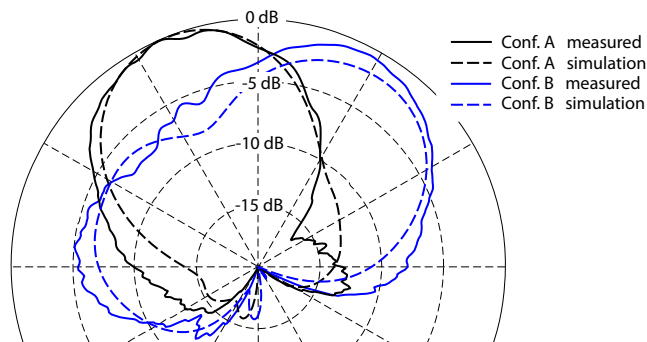
Fig. 4.7: Simulted and measured radiation pattern of the multi-size pixel monopole with individually packaged Radant MEMS.

reliability due to the hermetic packaging. However, the cost of individually packaged MEMS is much higher than that of semiconductor switches due to the high cost of the packaging process. Typical costs for high-volume quantities is above one dollar per unit, a price that is prohibitive for most commercial applications. The assembly process is also more expensive that typical PCB assembly processes due to the wire-bonding connections.

4.2.3   Monolithically integrated RF-MEMS

The large number of necessary switches in reconfigurable pixel antennas makes the external addition of individually packaged switches unpractical due to the cost and fabrication time. By using monolithically integrated switches, both the antenna and switches are manufactured with the same microfabrication process. This technique substitutes the serial addition of individual switches by the parallel process of micro-fabricating integrated switches. Since all the switches are fabricated simultaneously, densely switched designs can improve the fabrication time and cost, and addition-ally the undesired parasitic effects of the individual packaging and wirebondings are minimized. In this section we describe the RF-MEMS switch and switch-integrated pixel designs developed in a collaboration between Utah State University (USU) and Universitat Politècnica de Catalunya (UPC).[1]

RF-MEMS switch design

The RF-MEMS switch design is based on a cantilever structure and a scaled model is depicted in Fig. 4.8f. The cantilever is made of gold and its dimensions are $60\mu m$ by $105\mu m$, with a thickness of $3\mu m$. The dimensions of the cantilever determine the RF-MEMS spring constant, which can be roughly described as the resistance of the

---

[1]The work and results presented in this section are the result of a collaboration between Universitat Politècnica de Catalunya (UPC) and Utah State University (USU). The microfabrication process has been optimized by USU and has been carried out at Cornell Nanoscale Science and Technology Facilities (CNF) in Ithaca, New York.

cantilever to buckle. This is an important parameter with strong influence over the switch pull-in voltage and the switching time. This cantilever is anchored over a thin gold layer which is identical to the layer forming the contact surface between the cantilever and the RF-MEMS drain.

A gold rectangle located directly below the cantilever applies the electrostatic field required for switching. The location, size and shape of this biasing pad affect the pull-in voltage of the switch. The biasing line starting in the bias pad is manufactured using Tantalum Nitrate (TaN) which is a high-resistive material. The width of the line is $20\mu m$ and the thickness is approximately $0.3\mu m$ leading to a bulk resistance of approximately $2k\Omega$/sq.

In the lower part of the cantilever four small squares are located, which are called *dimples*. These small pieces reduce the contact area of the cantilever and minimize the stiction problems, that is the undesired sticking of the cantilever during the ON to OFF transition.

The analysis of the switch has been carried out by USU using the multiphysics sofware *Coventor*. The simulations predict a pull-in voltage of $40\,V$, insertion losses of $0.2 - 0.3\,dB$ (@ $5.5\,GHz$) and isolation of $20\,dB$ (@ $5.5\,GHz$). The switch is limited in frequency due to isolation, having $12\,dB$ of isolation at $20\,GHz$.

Microfabrication process

The RF-MEMS switch is fabricated using microfabrication processes which consist in the selective application of material addition (deposition), material removal (etching) and material modification (implantation, diffusion...). Certain areas are *protected from* or *exposed to* these processes and thus patterning the material. This patterning is done using microlithography which consists in three basics processes: deposition, exposure and etching.

The first step in microlithography is the deposition of a layer of the material to be patterned (for instance, a metal). The different deposition methods are evaporation, sputtering, spinning and electroplating. Since direct patterning of the material is almost always impossible, a thin layer of a polymeric material called photoresist (PR) is coated over the material. The properties of this material change when is exposed to ultra-violet radiation. After coating with photoresist, certain areas are exposed to radiation using either contact lithography, image projection or e-beam lithography. Subsequently the wafer is developed, which means to eliminate the exposed photoresist, or to remove the unexposed photoresist in case of negative PR. At that moment, the geometry is already patterned over the photoresist. To transfer that pattern from the PR to the material, the etching process is applied, which consists of removing the non-protected material. This is done using etching liquids (wet etching) or high energy ions (dry etching). Finally, the stripping process removes the remaining photoresist, and only the patterned material remains.

The specific process followed to microfabricated the RF-MEMS switches here presented is subsequently described.

Step 1: *High-Resistive Lines* - Mask #1

(a) High-resistivity   **(b)** Evaporated gold   **(c)** Sacrificial layer

(d) Dimple patterning   **(e)** Electroplatted gold   **(f)** Release
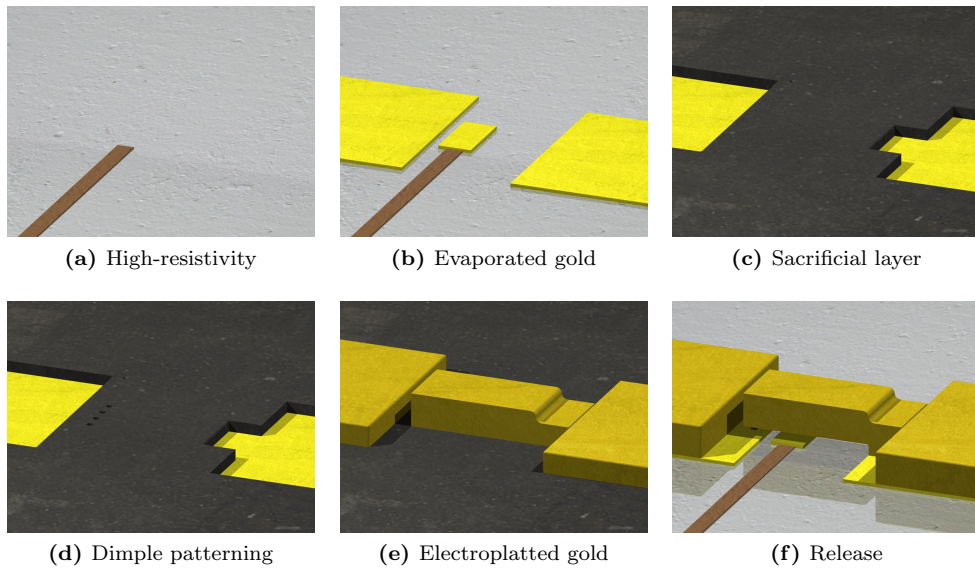
Fig. 4.8: RF-MEMS microfabrication process (vertical dimensions 10x magnified).

The employed material is Tantalum Nitrate (TaN). It is deposited using sputtering and dry etched with CF4 (Tetrafluoromethane) as a plasma etchant.

Step 2: *Thin gold Layer* - Mask #2
The gold is deposited by evaporation and patterned using wet etching. On the first stages lift-off technique was used but was rejected due to the undesired creation of spikes at the layer borders.

Step 3: *Sacrificial Layer* - Mask #3
Since the MEMS cantilever is a suspended structure, its fabrication requires the deposition of an auxiliary sacrificial layer to fabricate the cantilever on top. This sacrificial layer is composed of PMMA (Poly-Methyl Methacrylate) and is deposited by spinning. The patterning of PMMA is complex due to its similar properties to photoresist. For that reason, the PMMA has been covered by a masking titanium layer. The titanium has been patterned using wet etching and afterwards the PMMA has been etched using O_2 dry etching.

Step 4: *Dimples* - Mask #4
To create the dimples, a set of small holes must be patterned over the photoresist and for that reason there is no deposition process in this step. The patterning of the dimples is identical to the PMMA patterning in the previous step.

Step 5: *Electroplatting* - Mask #5 & #6
In this step the cantilever is created. Due to large thickness of this layer ($3\mu m$) the deposition technique used is electroplating. Since electroplating only de-

(a) Multi-size pixel monopole **(b)** Parasitic pixel layer
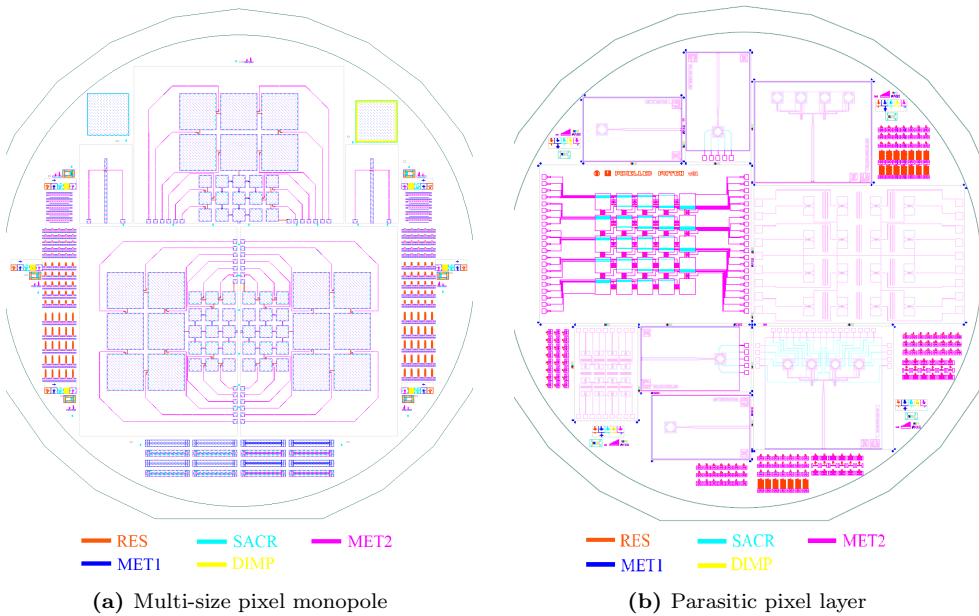
Fig. 4.9: Mask set used in the fabrication of the MEMS-antenna prototypes.

posits metal over metal surfaces, a Au/Cr seed layer is previously deposited and patterned. This is the most critical step in the MEMS microfabrication process.

Step 6: *Dicing*
The quartz glass substrate is diced using a diamond blade. This is harsh process that generates high amplitude vibrations. For this reason it is important to keep the PMMA under the cantilever during this process to prevent damages.

Step 7: *Release*
The release process consists on the removal of the sacrificial layer, leaving the MEMS cantilever in the appropriate suspension state. The PMMA is wet etched and dried using critical point dry technique, which prevents damages resulting from the surface tension produced at the liquid-gas phase interface.

MEMS-antenna prototypes

Two MEMS-antenna prototypes have been fabricated following the multi-size pixel monopole design and the parasitic pixel layer design. The mask set used in each prototype is depicted in Fig. 4.9. The mask set for the multi-size pixel monopole includes three identical copies of the pixel antenna, while the mask set used for the parasitic pixel layer is shared with other MEMS-antenna designs.

The RF-MEMS in the pixel antennas where individually tested directly on-wafer after their release. It was observed that the yield of the microfabrication process was
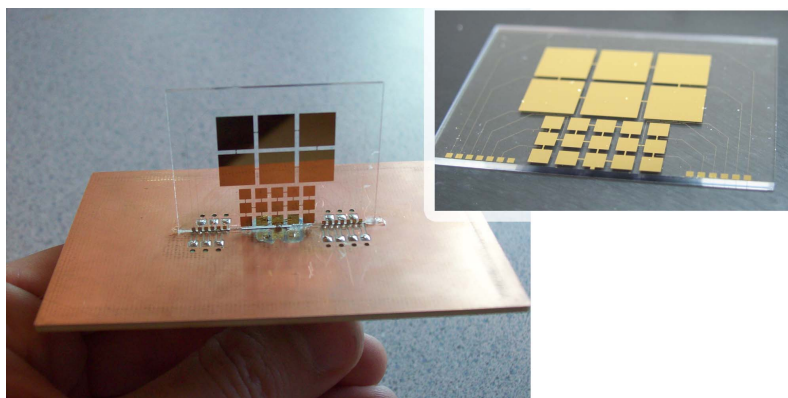
(a) Multi-size pixel monopole
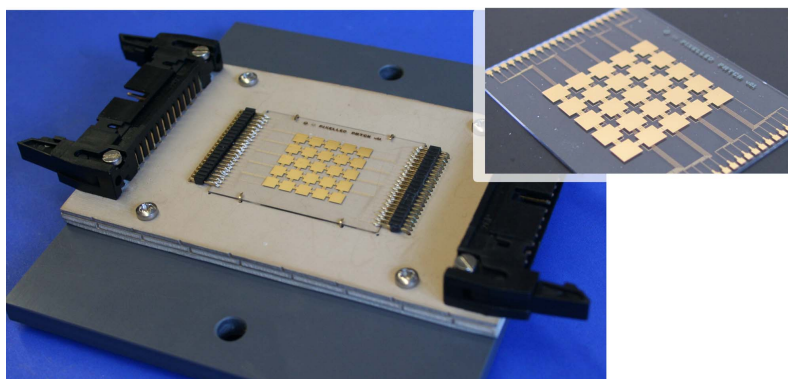
(b) Parasitic pixel layer

Fig. 4.10: Pixel antenna prototypes with monolithically integrated RF-MEMS switches.

approximately 40%, which means that 40% of the RF-MEMS used by the antennas operated as expected. The rest of the RF-MEMS presented a certain type of malfunction, typically a short-circuit between the source and drain. After the on-wafer testing of the RF-MEMS, the two antenna prototypes were assembled as shown in Fig. 4.10. The impedance properties of each prototype were tested, however only minor modifications of the antenna properties were observed when the switches were biased. The reason of this poor reconfigurability was the original low yield plus the additional stress produced over the switches due to transportation and assembly, specially considering that the RF-MEMS switches were not packaged.

This result contrasts with the high yield achieved by the microfabrication process for the switches located on the same wafers but outside the antenna structures. These switches are located in uniform grids for individual testing and the observed yield in this case is between 80% and 90%. The cause of these different yields is the thickness uniformity of the electroplated gold, which depends on several factors such as the distance to the wafer edge and the amount of metal surrounding the RF-MEMS. This
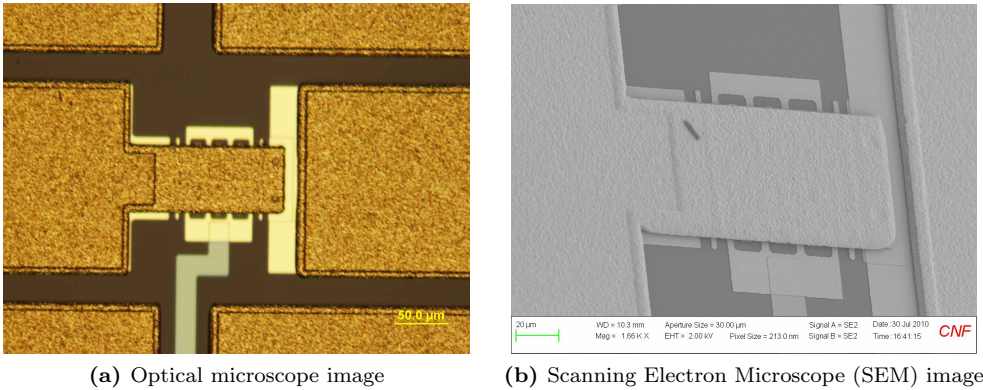
(a) Optical microscope image

(b) Scanning Electron Microscope (SEM) image

Fig. 4.11: Microscope images of the microfabricated RF-MEMS switches.

phenomenon makes that the cantilevers of the RF-MEMS inside the antennas present different thickness thus reducing the yield of the process. As a conclusion, the RF-MEMS antennas have to be designed to maximize the uniformity of the distribution of the electroplated gold surrounding the RF-MEMS. The microfabrication process has to be optimized to maximize the yield for the RF-MEMS in the antennas rather than for those uniformly located outside the antennas.

Individual switch characterization

Images of the microfabricated switches are presented in Fig. 4.11. The image in Fig. 4.11a corresponds to an optical microscope where the different parts of the RF-MEMS switch described in Fig. 4.4a can be clearly distinguished. It is worth mentioning the clear differences that can be observed between the uniform evaporated gold over the bias and contact pads and the grainy-looking electroplated gold that forms the cantilever and most part of the source and drain. The image in Fig. 4.11b corresponds to an scanning electron microscope (SEM). Since the SEM provides a perspective image rather than a top-view image, it can be clearly observed that the cantilever is suspended on top of the bias and contact pads.

Several of the RF-MEMS in the wafer where located in CPW lines for characterization purposes. The RF-MEMS where characterized using on-wafer calibrated measurements. In Fig. 4.12 it is represented the transmission coefficient of a RF-MEMS in ON and OFF states. The insertion losses of two different MEMS were measured, showing very similar results and an average insertion loss of 0.17 dB between 0 GHz and 20 GHz. The isolation of the RF-MEMS shows the typical response of a capacitor where the isolation decreases with frequency. There is an excellent agreement between the measured isolation and the simulations modeling the exact RF-MEMS geometry. The RF-MEMS operates from DC to a maximum operating frequency that limited by the switch isolation. For an minimum isolation of 10 dB the maximum operating frequency is 20 GHz. The isolation at lower frequencies is 28 dB at 2.4 GHz and 20 dB at 5.5 GHz. The insertion loss and isolation values agree well with those predicted by
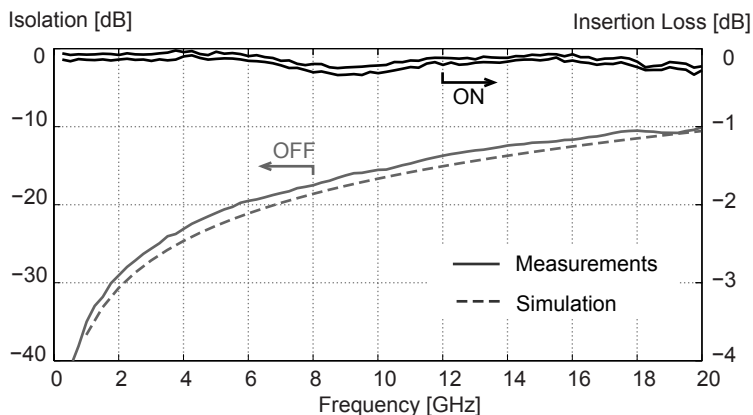
Fig. 4.12: Measured isolation and insertion loss of the microfabricated RF-MEMS switches.

the multiphysics simulations described in a previous subsection.

4.3 MICROFLUIDIC TECHNOLOGY

4.3.1 Microfluidic pixel antenna

Microfluidics is a technology with great potential in pixel antennas. By using well-known microfluidics techniques such as continuous-flow or electro-wetting it is possible to move small portions of liquid metals. This capability allows to dynamically create and remove the pixels of a liquid metal pixel antenna. This way, the reconfigurability of a microfluidic pixel antenna does not depend on the interconnection of different pixels, but instead, the different pixels are dynamically activated by moving liquid metal sections. This pixel creation capability provides an improved reconfiguration capability to microfluidic pixel antennas compared to switched pixel antennas.

The operating mechanism of the microfluidic pixel antenna is novel in the field of reconfigurable antennas, however it has been previously demonstrated for color displays as a new method to fabricate color electronic ink [112]. The pixels of the microfluidic pixel antenna consists on a flat square shape made of a polymeric material with an internal reservoir that contains a liquid metal. For OFF-state pixels (Fig. 4.13a) the liquid metal is completely contained in the internal reservoir of the pixel, occupying an small disconnected area which makes it transparent from an electromagnetic perspective. When the pixel switches to ON-state (Fig. 4.13b), the liquid in the reservoir is transported to the surface of the pixel, occupying the complete area of the pixel and potentially establishing contact with adjacent pixels.

The liquid metal transportation can be achieved by electrowetting on dielectric (EWOD), a technique that consists on moving a liquid by changing its surface tension through the application of a static electric field [113, 114]. This technique can be applied for moving liquid metals such as mercury or a non-toxic alternative such is Galinstan®.

(a) Pixel OFF   **(b)** Pixel ON
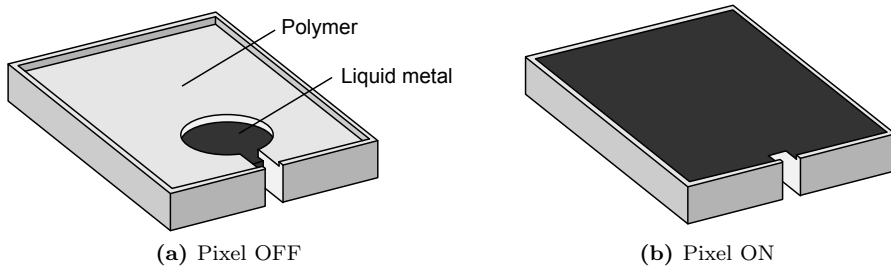
Fig. 4.13: .

At the time of writing this document, the usage of liquid metals together with microfluidic technology in reconfigurable antennas is very limited. Liquid dielectrics are relatively common in reconfigurable antennas due to the phase velocity tunability of liquid crystals [41] and nanoparticles mixes [115, 116]. However the usage of liquid metals such as mercury has been constrained to deformable body-wearable antennas [57, 117], with recent applications to frequency selective surfaces and metamaterials [118–120].

Considering the low maturity of microfluidics in the context of reconfigurable antennas, the goal of this section has been set as the design, fabrication and characterization of a microfluidic reconfigurable antenna with movable liquid metal sections. This microfluidic antenna prototype would validate the practicality of liquid metal microfluidics in the design of reconfigurable antennas and would pave the way for future microfluidic pixel antennas.[2]

4.3.2 Microfluidic Yagi-Uda design

The work here presented uses liquid metal to implement movable parasitic elements that steer the antenna beam through their variable positions. The actuation over liquid metals is effectively controlled using standard microfluidic techniques more commonly used in chemical and medical applications rather than electromagnetics.

The design is based on a reconfigurable Yagi-Uda type array consisting of a central driven element and movable liquid metal parasitic sections located into a microfluidic channel circularly arranged around the central active driven element as seen in Fig. 4.14. The driven antenna, which is made out of solid copper, has a static behavior while reconfigurability is achieved through the variable positions of the liquid metal parasitics. The novelty of the antenna lies in the circular geometry of the Yagi array, the particular design of the driven element and, more importantly, the liquid composition of the parasitics. The antenna is designed to operate in 1.8 GHz LTE band which might be a good candidate for future US public safety communications networks. Due to the liquid nature of the parasitics, a micropump can be utilized to change their positions by controlling a continuous flow inside a microfluidic channel. The proper design of the driven antenna along with the positions of the movable

---

[2]This section includes figures and text fragments, sometimes verbatim, from reference [JA6].
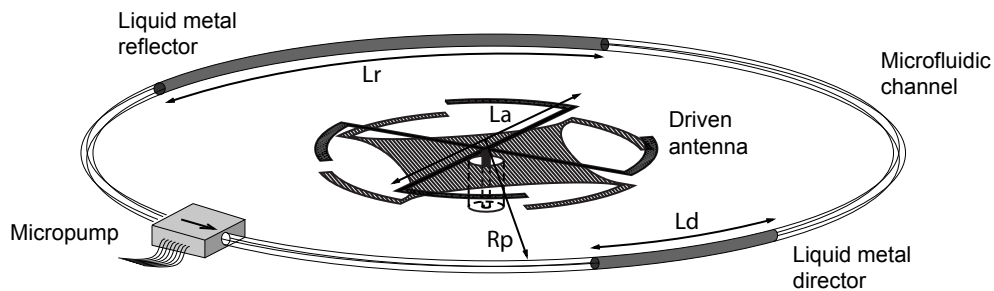
Fig. 4.14: Design of the microfluidic antenna based in a circular Yagi-Uda architecture with liquid metal parasitics.

parasitics enables a continuous steering of the radiation pattern with fine tuning over 360° range. In comparison with a beam-steerable rotor-driven antenna, the total mass displaced by the microfluidic system is substantially reduced, leading to lower power consumption and less suffering from inertia. These advantages, together with the natural auto-lubrication and liquid heat dissipation of microfluidic systems, provide additional mechanical robustness.

Driven Antenna Design

The reconfiguration capability of the microfluidic antenna is based on electromagnetically coupled liquid metal parasitics. The driven antenna, therefore, has to be designed to maximize induced currents over the parasitics. This can be achieved by using a central active element with omnidirectional pattern and horizontal polarization. It is desirable that its radiation pattern presents a maximum in the parasitics plane and that the magnitude and phase of the generated electric field remain constant over the complete microfluidic channel. This last condition ensures that the parasitics movement into the microfluidic channel produces a non-distortive rotation of the radiation pattern.

The first natural candidate is the loop antenna which has horizontal polarization, omnidirectional pattern and an invariant electric field over the microfluidic channel ensured by the revolution symmetry of its currents. The loop antenna, must be kept electrically small in order to maintain a uniform current. On the other hand, the radiation resistance of a electrically small loop is very low, leading to narrowband low-efficiency solutions. The main approach here is to use an Alford-type loop [121], a set of in-phase fed antennas rotationally distributed over a circumference.

A few Alford-loop examples can be found in the literature [122–124], however their use as driven element in the circular Yagi array is not appropriate due to the required pattern uniformity level, horizontal diameter and thickness respectively, therefore, a novel specific design needs to be considered. The requirements regarding these three aspects are detailed below.

1. *Pattern uniformity.* When considering the directivity variation over the omnidirectional plane, it is clear that increasing the number of sections of the Alford
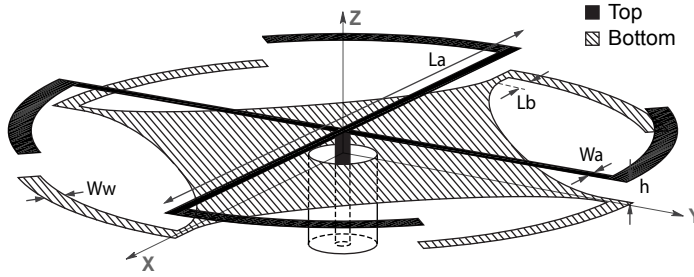
Fig. 4.15: 3-D schematic of the driven antenna (Wa=1.0, Ww=2.0, La=58.5, Lb=2.0, h=0.81) [units in mm]

loop results in an omnidirectional pattern with higher uniformity and a less variable electric field over the circular microfluidic channel. In this particular Yagi array, simulations show that a loop approximation of at least 4 sections is necessary to avoid pattern distortions when the parasitics move.

2. *Horizontal dimensions.* The dimensions of the driven antenna are related to the parasitic elements. Since these parasitics are used to provide directionality to the Yagi, their lengths must be comparable with the central loop length; otherwise, the radiation pattern would be dominated by the central driven antenna. As an example, if a half wavelength director is desired to represent at least 50% of the driven element length, the maximum diameter of the central antenna is $\lambda_0/3$.

3. *Thickness.* From a practical perspective, low-profile printed antennas are preferred due to their integrability, low-weight and the possibility of fabrication using surface micromachining techniques [125, 126]. Although microfabrication aspect has not been considered in this work due to the large physical dimensions of the antenna, it is the preferred approach at higher frequencies because it allows the integration of antennas, microfluidic systems and control circuitry.

The 3-D schematic of the driven antenna design is depicted in Fig. 4.15 and is fabricated using RO4003 as substrate ($\epsilon_r = 3.55$, $h = 0.81$mm). It consists of four printed dipoles rotationally distributed over a loop. This number of dipoles leads to a good trade-off between size and pattern uniformity. The antenna has a diameter (L_a) of 58.5mm ($0.35\lambda_0$) and a simulated pattern variation over the horizontal plane of ± 0.09 dB .

The four dipoles are in-phase fed using transmission lines that transport the energy from the central coaxial feed. The lengths of the transmission lines in terms of the effective wavelength are $0.27\lambda_{ef}$ and are in fact quarter-wave transformers. Therefore, the equivalent impedance of each dipole can be adjusted modifying the transmission line widths in order to obtain a 50Ω impedance after the parallel combination of the four dipoles at the coaxial feeding point.

The antenna is desired to be microstrip fed and requires a balun to transform the unbalanced microstrip feeding in an appropriate balanced line to feed each dipole. The antenna is highly compatible with a balun design which consists of the progressive
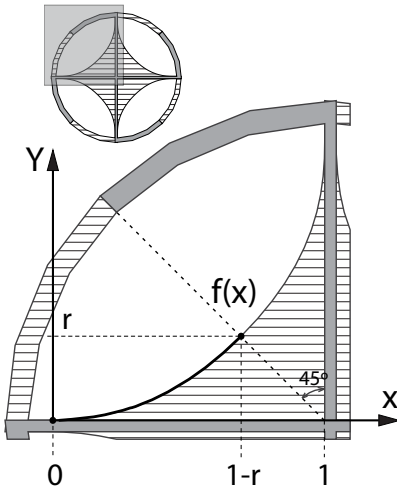
Fig. 4.16: Analythical representation of the balun contour.

(a) $r = 0.05$ **(b)** $r = 0.20$

(c) $r = 0.35$ **(d)** $r = 0.50$
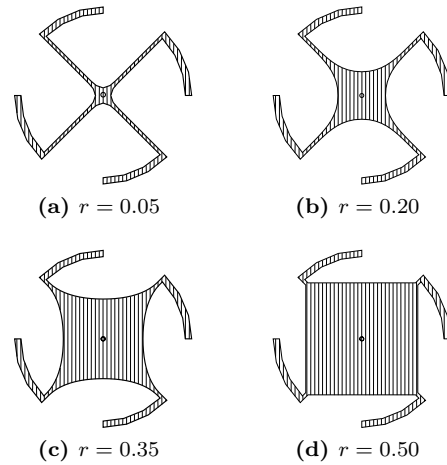
Fig. 4.17: Bottom layer for different aspect ratio baluns

reduction of the microstrip ground plane [127]. The length of these lines is approximately a quarter wavelength, which is the minimum required length for the balun. Let $f(x)$, $0 \leq x \leq 1 - r$, be the taper function of a normalized length balun as shown in Fig. 4.16. The complete balun is obtained by applying repeated 90° rotations to the basic taper function, which is properly designed to ensure smoothness. The first order continuity constraints are presented in (4.1), where r is a *shape factor* parameter which represents the narrowing rate of the microstrip ground plane as shown in Fig. 4.16.

$$
\begin{aligned}
f(0) &= 0 \qquad f(1 - r) = r \\
f'(0) &= 0 \qquad f'(1 - r) = 1
\end{aligned} \tag{4.1}
$$

The performance of this balun type is discussed in [128, 129]. The typical choice is an exponential taper but the addition of the continuity conditions leads to non-analytically solvable equations. A similar potential-function taper was chosen, resulting in a compact analytical solution given in (4.2).

$$
f(x) = Ax^B \ , \ \text{where} \quad
\begin{aligned}
A &= r(1 - r)^{1 - 1/r} \\
B &= \tfrac{1}{r} - 1 \\
r &< 0.5
\end{aligned} \tag{4.2}
$$

The bottom layer of the balun structure for different values of the shape factor "r" is depicted in Fig. 4.17. Values of r greater or equal to 0.5 are not considered due to the creation of a vertex near the dipole feed, which violates the continuity conditions in (4.1).

The performance of the balun was evaluated for different shape factors by analyzing the crosspolar level of the antenna, which is mostly due to the undesired currents over
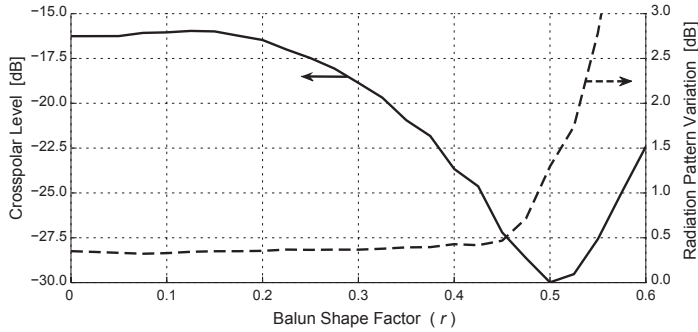
Fig. 4.18: Analysis of the balun performance for different shape factor values. The crosspolar level has been simulated for a coaxial cable with a length of 32mm and the ground capacitive coupling has been created using a PEC dish with a diameter of 58mm. A 0.5mm top-bottom alignment accuracy has been considered for the pattern uniformity simulation

the outer surface of the coaxial shield and is an indicator of the balun performance. Accurate simulation of these currents requires a volume-modeled outer conductor and a forced capacitive coupling between the antenna and the ground. The results are presented in Fig. 4.18. Shape factor values between 0.4 and 0.5 result in crosspolar levels between -23dB and -30dB. However, shape factors close to 0.5 degrade the antenna omnidirectionality in case of top-bottom misalignment. Accordingly, a value of $r = 0.4$ was chosen.

The simulated and measured reflection coefficients for the antenna design are presented in Fig. 4.19. Very good agreement between simulations and measurements can be observed for resonance frequency (1.8 GHz) and bandwidth (5.0%). The minor shift in resonance frequency is consistent with substrate and fabrication tolerances. The radiation patterns for the two main cuts are presented in Fig. 4.20. The measured pattern variation over the horizontal plane is ± 0.3 dB which is consistent with the alignment accuracy and is small enough to preserve the integrity of the pattern in conjunction with the movements of the parasitics. The measured crosspolar level is below -20 dB, which corresponds to a 10 dB improvement compared to preliminary non-balun prototypes.

Parasitics Optimization

By using the Yagi-Uda array principle, the microfluidic antenna creates a directional radiation pattern through the addition of several parasitics. In this section the location and dimensions of the parasitics are optimized for maximum directivity and front-to-back ratio.

A geometry with one reflector and one director on a single microfluidic channel is chosen as a proof-of-concept. Design details and dimensions are presented in Fig. 4.21. The distance between the driven antenna and the parasitics (D_p) is usually between $0.15\lambda_0$ and $0.35\lambda_0$. In this design the parasitic elements are distributed over a circle
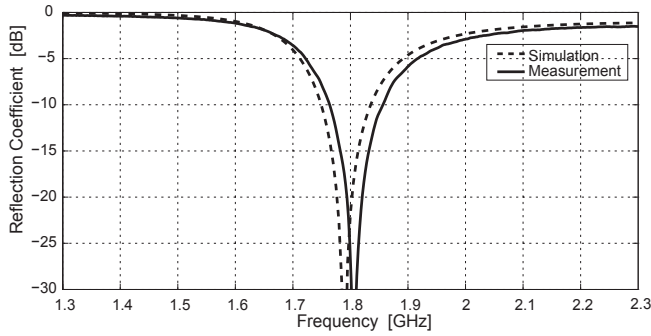
Fig. 4.19: Reflection coefficient of the driven antenna

(a) E-Plane (XY)

(b) H-Plane (XZ)
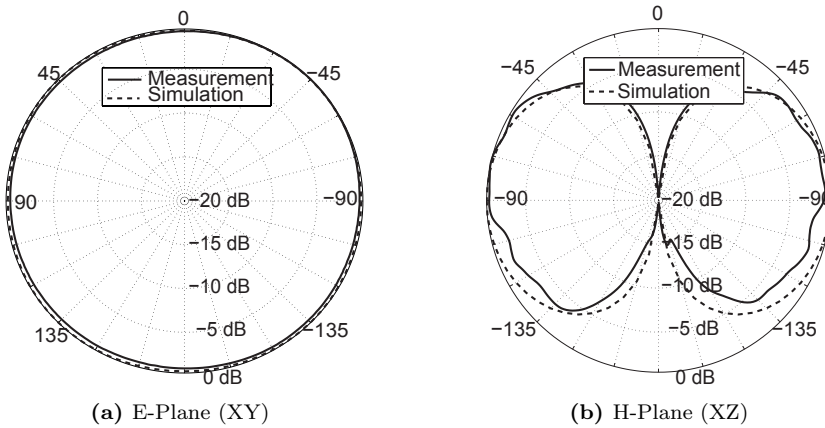
Fig. 4.20: Radiation patterns of the driven antenna

with a radius $R_p = 80$mm, which corresponds to a distance $D_p = 50.75$mm $= 0.3\lambda_0$. The director is slightly shorter than the resonant length, which in this design corresponds to an optimum value of $L_d = 62$mm. Since the effective permittivity of a dipole over this substrate is $\epsilon_{\mathrm{r,eff}} = 1.41$, the electrical length of the director is $0.45\lambda_{\mathrm{eff}}$. Simulations indicate that the reflector parasitics with a large length (L_r) produce a stronger reflection, thus redirecting power towards the director direction. Accordingly, the reflector has been designed to operate on its second resonance, having an electrical length slightly longer than $\frac{3}{2}\lambda_{\mathrm{eff}}$. The resulting reflector length after optimization is 217mm $(1.56\lambda_{\mathrm{eff}})$.

A prototype where the segments of liquid metal are replaced by sections of solid copper wire was manufactured. The simulated and measured radiation patterns are presented in Fig. 4.22 with good agreement between them. As expected, the main beam points towards the director with a beamwidth of approximately 90°. Two side-lobes are observed, with a power level of -2 dB compared with the main beam. On the other hand, the level of back radiation is much lower, having a front-to-back ratio
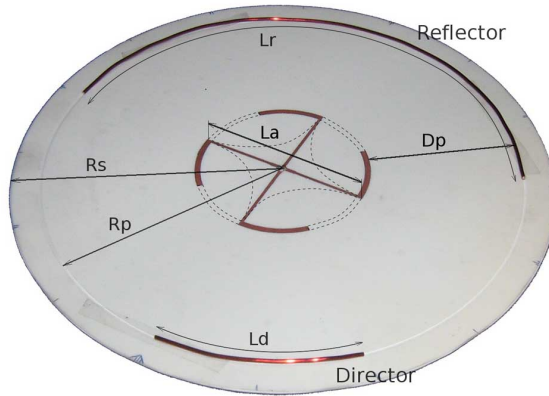
Fig. 4.21: Parasitic elements ($R_p = 80$, $R_s = 90$, $L_d = 62$, $L_r = 217$, $La = 58.5$, $D_p = 50.75$) [units in mm]

of 10 dB. Then, this particular antenna design could be better suited for applications where a low level of back radiation is more important than side-radiation. A higher directivity and narrower beamwidth can be achieved by increasing the number of parasitic directors located over several concentric circles.

The main advantage of this design is the continuous steerability of the radiation pattern by simply rotating the parasitics. This can be seen in Fig. 4.23 where the measured radiation pattern is shown for three different parasitics positions corresponding to rotation angles of 0º, 22.5º and 45º. The radiation pattern shape is properly preserved and no distortions are observed. The preservation of the pattern shape for other angles is ensured by the invariance of the antenna geometry respect to 90º rotations. This has also been checked experimentally demonstrating continuous beam-steering capability with smooth angular variation over a 360º range.

4.3.3 Microfluidic Yagi-Uda prototype

The main advantage of replacing solid wire parasitics by portions of liquid metal is that their physical displacement can be achieved through microfluidic techniques like pumping or electrowetting. A microfluidic antenna prototype was manufactured using mercury as liquid metal and pumping as a displacement method. A picture of this prototype along with the pumping elements is shown in Fig. 4.24.

The sections of mercury forming the parasitics are confined in a microfluidic channel with a inner diameter of 0.8mm, arranged in a closed double loop shape. The movement of the parasitics is produced by a micropump which is serially inserted into the tubing loop. The micropump and therefore, the parasitic movement, is controlled by a variable voltage source identified in the figure as the micropump controller.

Mercury was chosen based on its suitable electrical and physical properties; it has a high conductivity ($\sigma_{\mathrm{Hg}} = 10^6$ S/m), remains liquid for a wide range of temperatures (from -39ºC to 357ºC) and presents low adhesion to plastic elements which prevents
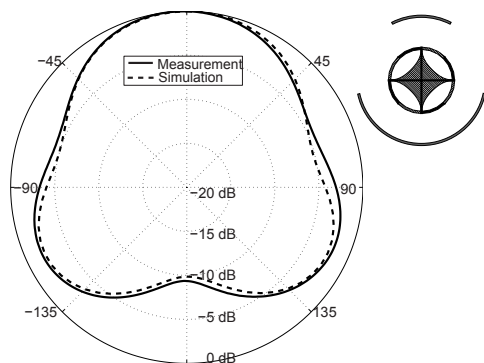
Fig. 4.22: Measured and simulated radiation patterns of the reconfigurable antenna with copper parasitics.
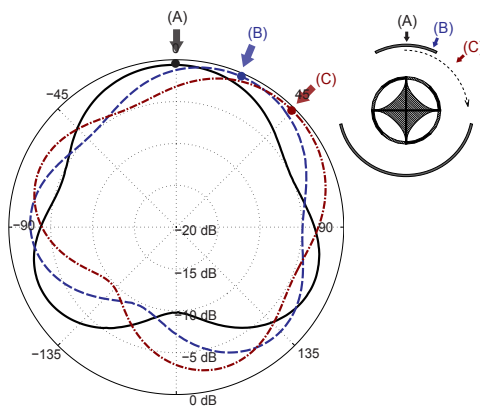
Fig. 4.23: Measured radiation patterns of the reconfigurable antenna with copper parasitics for configurations corresponding to rotations of 0°, 22.5° and 45°.
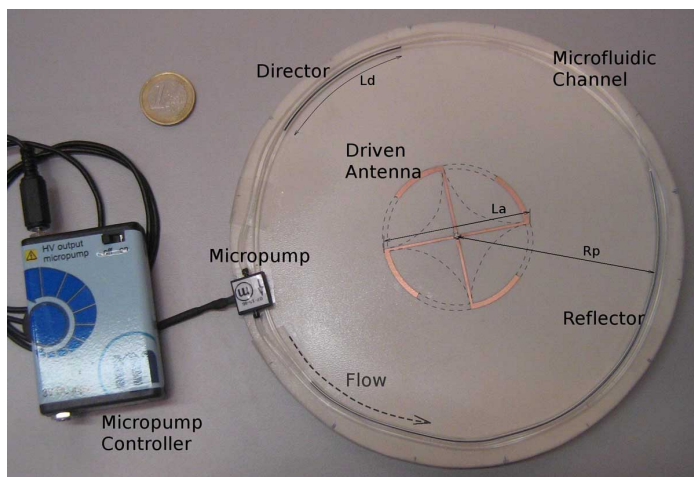
Fig. 4.24: Microfluidic Reconfigurable Antenna: Driven Antenna (Solid Copper), Director and Reflector (Liquid Metal, Hg), Microfluidic channel (plastic tube), Micropump and Controller.

wetting the tubing.

The arrangement of the tubing is made in a double loop shape instead of a single loop, otherwise some configurations would have one of the parasitics crossing the micropump. This situation could break or change the lengths of the parasitics due to internal reservoirs and inner valve systems of the micropump. The empty sections between mercury parasitics are filled with de-ionized water. Since the total volume of water is very small, the radiation pattern modifications and efficiency reduction due
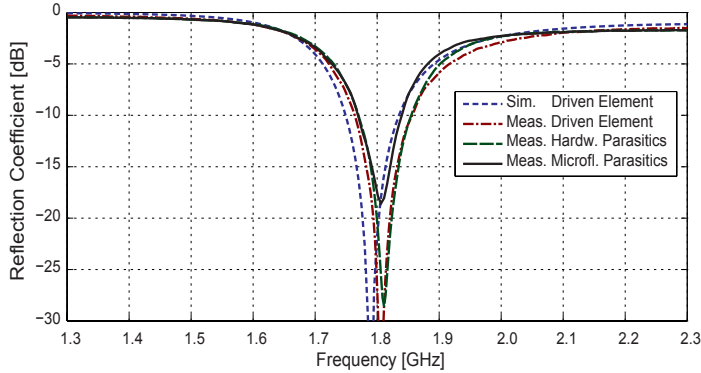
Fig. 4.25: Reflection coefficients of the microfluidic antenna.

to the water high contrast and losses ($\epsilon_r \approx 77$, $\tan\delta \approx 0.1$ @1.8 GHz [130]) is not significant.

A piezoelectric actuated micropump is used (mp5, Bartels Mikrotechnik GmbH). The physical dimensions of the micropump are 14mm × 14mm, which are smaller than a tenth of the wavelength at the operating frequency. The pump is voltage controlled by a 100Hz square signal generated at the micropump controller, which are the optimum signal shape and frequency for DI water pumping with this micropump. The flow rate and thus the parasitic movement speed can be adjusted by modifying the feeding voltage, which ranges from 100V to 250V. The flow rate changes linearly with the voltage, achieving a maximum flow rate of 5ml/min, providing the liquid parasitics with a linear speed of 0.16 m/s and leading to a beam-steering reconfiguration speed of 2 rad/s. Higher speeds could be achieved by reducing the tube diameter; however a narrower resonance of the parasitics may appear as a limiting factor.

The measured results of the microfluidic prototype corroborate the transparency of all microfluidic elements. The perturbations observed are due to the plastic tubing. These perturbations are produced by a slight increase on the effective permittivity ($\epsilon_{r,\text{eff}}$) seen by the liquid metal parasitics (from 1.41 to 1.49) and can be easily compensated by shortening the parasitics physical lengths. The corrected dimensions of the microfluidic parasitics are $L'_d = 58$mm and $L'_r = 205$mm.

The measured reflection coefficient of the microfluidic antenna prototype is presented in Fig. 4.25 and compared with those of the isolated driven element and the prototype with solid copper wire parasitics. The measured reflection coefficient remains unchanged for different positions of the parasitics for both prototypes, therefore, a single curve for each prototype is shown in the figure. Even after the addition of all microfluidic reconfiguration elements, the resonance frequency is maintained at 1.8GHz with a minor degradation of the resonance depth. The frequency bandwidth of the microfluidic prototype is slightly narrower than the isolated driven element bandwidth, being reduced from 5.0% to 4.0% at −10 dB level.

In Figs. 4.26 and 4.27 the radiation patterns of the microfluidic reconfigurable antenna are presented for different configurations. Fine beam steering into 0º, 22.5º
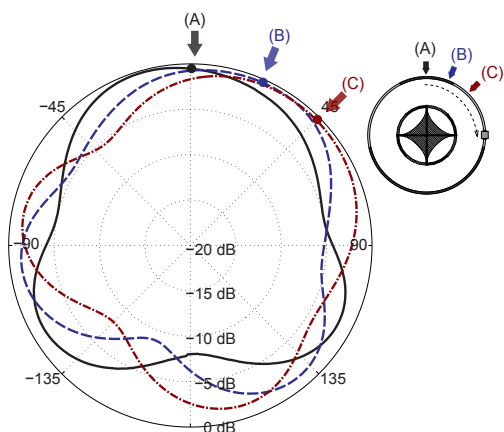
Fig. 4.26: Measured radiation patterns of the microfluidic reconfigurable antenna for configurations corresponding to rotations of 0°, 22.5^o and 45°.
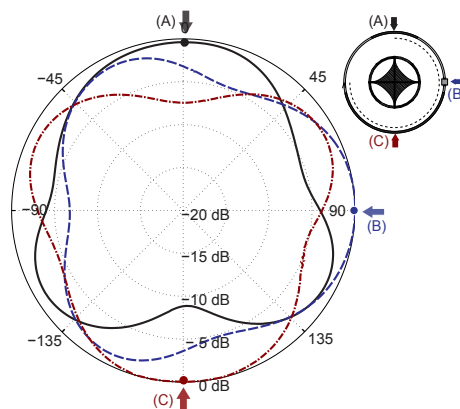
Fig. 4.27: Measured radiation patterns of the microfluidic reconfigurable antenna for configurations corresponding to rotations of 0°, 90° and 180°.

and 45º directions is shown in Fig. 4.26. The results are similar to the patterns measured for the wire parasitics prototype: the pattern shape is successfully preserved but both sidelobe ratio and front-to-back ratio are decreased by 1dB. The measured patterns corresponding to 0º, 90º and 180º steering angles are shown in Fig. 4.27. Again the pattern shape is preserved, providing reconfigurability in a range of 360º. The peak level variation between these configurations is ± 0.3 dB and is not related to the reconfiguration system but to the non-perfect omnidirectionality of the active element.

The measured peak gain of microfluidic antenna compared with the wire parasitics prototype is only 0.55 dB smaller, which is due to a combination of a reduction in directivity and efficiency. The loss of directivity for the microfluidic prototype, evidenced by an increased level of sidelobes and back-radiation, has a value of 0.5 dB. Therefore, the efficiency reduction due to the losses on all microfluidic elements (mercury, water, tubing and micropump) is 1%. This result completes the demonstration of the good electromagnetical performance of the presented microfluidic system regarding the antenna input impedance, radiation pattern and efficiency.

Future work concentrates on improving the microfluidic displacement technique by using digital microfluidics. In this technology, metal electrodes are used to actuate the liquid droplets of different size and shapes, by making use of the phenomenon known as electrowetting on dielectric (EWOD) [113, 114]. The main advantages for antenna reconfiguration are the precise control over the liquid metal position and the possibility of splitting and merging liquid droplets [131], making possible to dynamically adjust the number of parasitics, their lengths and positions. On the other hand, digital microfluidics introduces new considerations due to the intensive use of metallic elements such as electrodes and biasing lines. Ensuring their EM transparency, by

introducing high-resistive materials for example, will be one key requirement for new digital-microfluidic antennas.

PIXEL ANTENNA PROTOTYPING AND CHARACTERIZATION

Prototypes of the pixel antenna designs proposed in chapter 3 are presented in this chapter. All the practical issues related to antenna prototyping, such as the switch biasing and control, are thoroughly covered. The measuring set-up and methodologies for the experimental characterization of pixel antennas is also described. These characterization methodologies are used to fully characterize the reconfiguration capabilities of the multi-size pixel monopole and the parasitic pixel layer.

5.1 MULTI-SIZE PIXEL MONOPOLE

A prototype of the multi-size pixel monopole is fabricated and characterized in this section. The main considerations regarding the design process and pixel dimensions were covered in detail in section 3.3, while this section focuses on the practical and experimental perspectives.[1]

5.1.1 Multi-size Pixel Prototype

The prototype is a scaled version of the multi-size pixel monopole in section 3.3 and is designed to provide simultaneous pattern and frequency reconfiguration over L, S and C bands; achieving maximum pattern reconfigurability at 2.45 GHz ISM band. A picture of the prototype as well as the main antenna dimensions are presented in Fig. 5.1.

The antenna consists of a $\lambda_0/2$ by $\lambda_0/2$ surface composed of multiple-sized pixels divided in a driven and a parasitic region. The driven region has a high density of pixels with dimensions below $\lambda_0/20$. Its height is intentionally shorter than a quarter-wave monopole in order to enable strong horizontal currents which intensify the coupled currents over the parasitic area. This parasitic region is composed of larger pixels with dimensions of $0.15\lambda_0$ and, in order to strongly influence the antenna pattern, it is designed to cover almost four times the area of the driven region.

---

[1]This section includes figures and text fragments, sometimes verbatim, from references [JA7] and [CA4].
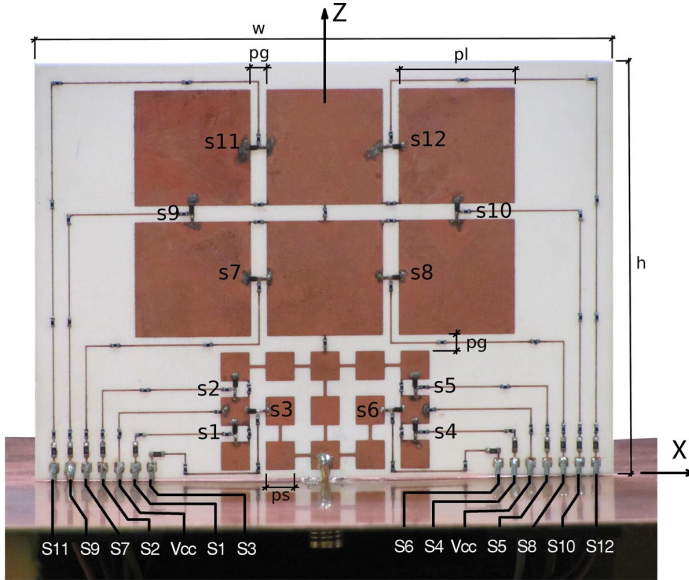
Fig. 5.1: Multi-size pixel monopole prototype fabricated over substrate RO4003 (t=0.81mm) with a 160mm x 200mm ground plane (p_g=2.5mm, p_s=4.5mm, p_l=18.0mm, w=90.0mm, h=65.0mm)

RF-switches have been implemented using PIN diodes (Infineon Technologies BAR64). The serial diode-capacitor combination used in the prototype has been previously characterized resulting in insertion losses of 0.3 dB and an isolation of 12 dB at 2.45 GHz. For simulation purposes, a data-fit equivalent circuit model has been calculated. The switch ON-state is modeled as a serial resistance ($R_{\mathrm{on}} = 3.5\,\Omega$) and the OFF-state is modeled as a parallel R-C circuit ($R_{\mathrm{off}} = 2.6\,\mathrm{k}\Omega$, $C_{\mathrm{off}} = 0.17\,\mathrm{pF}$). Switches have been included in the simulation model using RLC boundaries with the corresponding ON-OFF state circuit values.

The biasing network is accommodated on the same layer as the pixel surface to avoid the use of vias. The biasing network is depicted in Fig. 5.2. The complete pixel surface is interconnected through lumped inductors and DC-isolation between the different diodes is provided using DC-block capacitors. This configuration permits biasing the switches using 14 lines (12 switches and 2 Vcc), which have been split in electrically small sections using inductors, ensuring their RF transparency and minimizing coupling with the radiating pixel surface. Additionally, biasing lines have been designed to cross the ground plane, what permits locating the switch control circuitry below the ground plane, thus minimizing the undesired coupling.

5.1.2   Multi-size Pixel Characterization

The complete setup used to measure the impedance characteristics of the antenna is depicted in Fig. 5.3. The biasing lines of the multi-size pixel monopole are connected to a USB-controlled switch board (Agilent U-2653A). The switch board is in turn
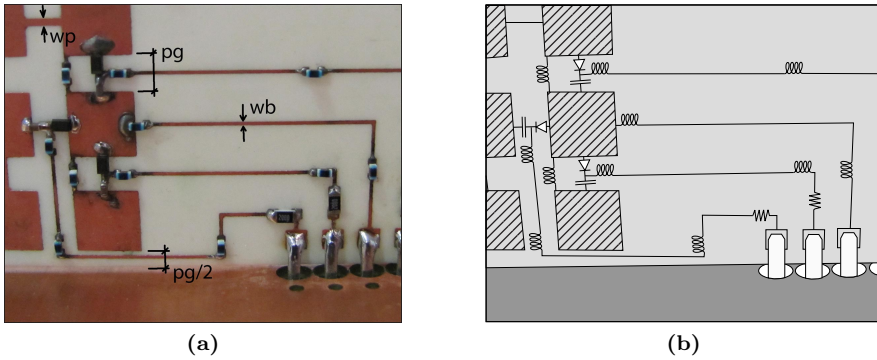
Fig. 5.2: Detailed view of the biasing network and the equivalent circuit model (w_p=0.25mm, w_b=0.15mm, p_g=2.5mm)
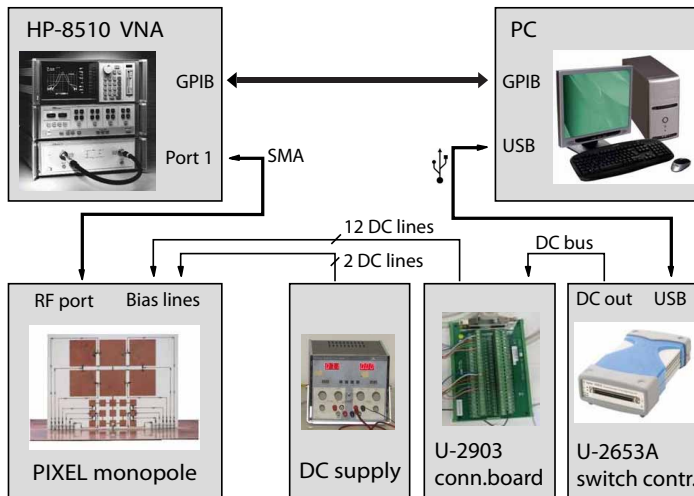
Fig. 5.3: Setup to characterize the frequency reconfiguration properties of the multi-size pixel monopole antenna.

connected to a PC, which determines and applies the required switch configuration at each time. The RF-port of the pixel antenna is connected to a Vector Network Analyzer (VNA) for characterization purposes.

An analogous setup in anechoic chamber has been used to measure its radiation patterns. In this case the antenna is located in the anechoic chamber and connected to the RF-measuring equipment and mechanical motors.

The characterization setup presented is used to explore and characterize the impedance and radiation properties of the complete antenna configuration space composed by $2^{12} = 4.096$ different configurations. The exponential growth of the configurations space with the number of switches, makes an exhaustive characterization unafford-
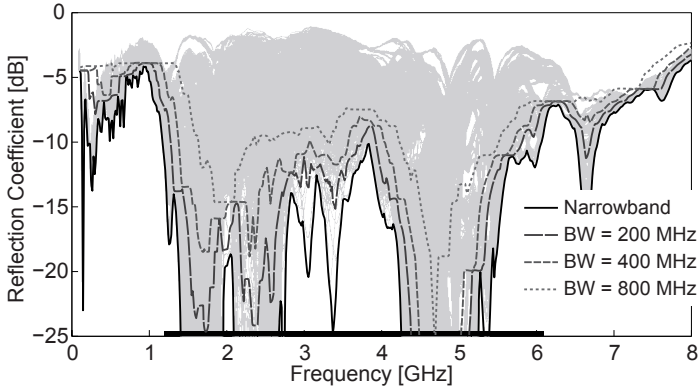
Fig. 5.4: Reflection coefficient of the optimal configuration at each frequency.

able for common pixel antennas, which typically use more than a hundred switches. However, the aggressive switch reduction approach applied in the presented prototype enables the possibility of performing exhaustive measurements to fully characterize the reconfiguration properties of the antenna, offering valuable information about maximum reconfiguration ranges and about the linkage between frequency and pattern reconfiguration.

5.1.3   Frequency Reconfigurability

The frequency reconfiguration capabilities of the pixel monopole are represented in Fig. 5.4. The background grey lines correspond to the superposition of the reflection coefficient for all the different configurations. Based on the previous complete set of configurations, four specific minimum boundary curves based on Eq. (5.1) corresponding to BW=0 (narrowband), 200 MHz, 400 MHz and 800 MHz are represented.

$$|s_{11}^{\mathrm{opt}}(f_0, BW)| = \min_{\substack{s_j \in \{0,1\} \\ j=1:12}} \max_{|f-f_0| \leq BW/2} |s_{11}(f)| \tag{5.1}$$

The curve labeled as *narrowband* provides a good approximation of the maximum frequency reconfiguration range for applications requiring a bandwidth up to some tents of megahertz. For each frequency between 1 GHz and 6 GHz approximately, the antenna is capable of synthesizing optimized configurations with a reflection coefficient below -10 dB.

Analogous traces are presented for applications with wider bandwidth requirements by considering the worst in-band reflection coefficient instead of the central frequency reflection coefficient, as expressed in Eq. (5.1). It can be observed that the frequency reconfiguration range is almost entirely preserved up to bandwidths of 400 MHz, what means that the frequency reconfiguration range is achieved through wideband configurations rather than sharp resonances.

The previous results quantify the quality of the optimal configurations. However, from a practical perspective, it is important to quantify also the quality of the global
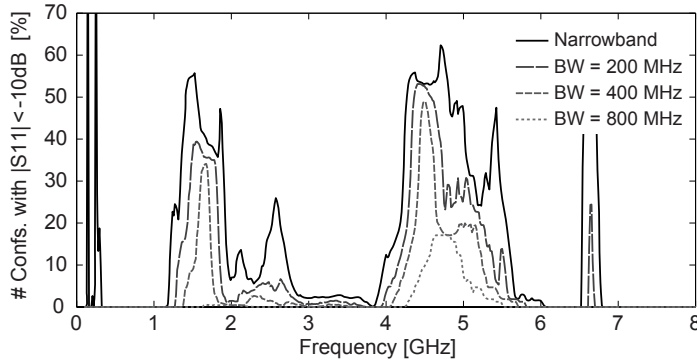
Fig. 5.5: Relative number of configurations with a reflection coefficient below -10 dB at each frequency

configurations space. For instance, in applications where the switch configuration is dynamically optimized, the reconfiguration time does not depend on how low is the reflection coefficient for the best configuration but instead, it depends on how many configurations have an acceptable reflection coefficient. In Fig. 5.5 the relative number of configurations producing a reflection coefficient below -10 dB is represented. These curves are generated by counting at each frequency the number of configurations with a reflection coefficient below -10 dB over the required bandwidth and expressing the result as a percentage of the 4.096 possible configurations. The resulting curves indicate a large number of suitable configurations over the whole frequency range. Notice that a value of 1% indicates the existence of more than 40 suitable configurations. These curves would be desired to be as flat as possible, however, the results indicate that the capability of the antenna to generate suitable configurations is highly frequency dependant. Notice that as a result of the design procedure, a significant number of configurations with a reflection coefficient below -10 dB is obtained for the design frequency (2.45 GHz).

5.1.4 Pattern Reconfigurability

As shown in the design section of the multi-size pixel monopole, this pixel antenna is not only frequency reconfigurable but also pattern reconfigurable. Pattern reconfiguration has been analyzed here from a beam-steering perspective. The realized gain (including mismatch losses) at the design frequency has been measured for the complete configuration space. Gain measurements have been constrained to the XZ plane. Due to the XZ mirror symmetry of the antenna, polarization over this plane is always linear ($\hat{\theta}$ oriented) regardless of the selected configuration. Additionally, configurations steered towards directions out of this plane are avoided because they produce an undesired lobe towards the symmetric direction that reduces the total gain of the configuration.

In Fig. 5.6 the measured and simulated realized gains of the optimal configurations for $\theta_0 = -60^\circ$, -30°, 0°, 30° and 60° directions are represented. It can be clearly

(a) f = 2.45 GHz, measurement

(b) f = 2.45 GHz, simulation
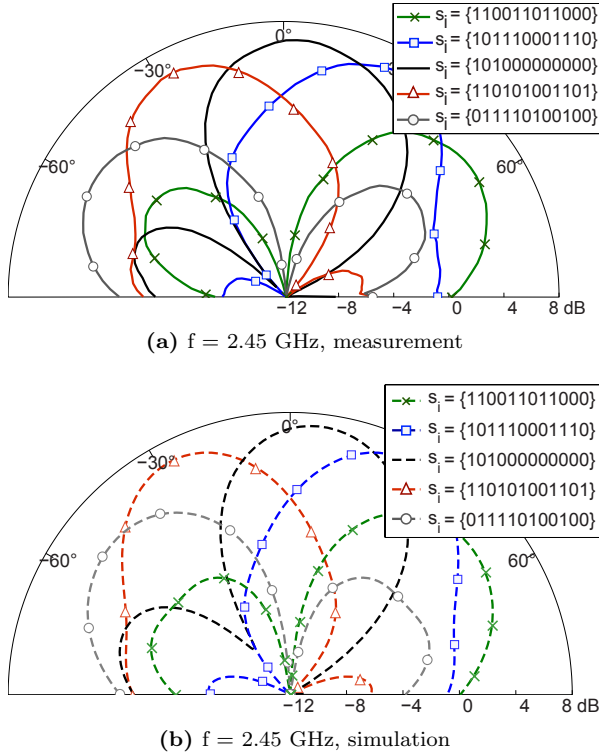
Fig. 5.6: Realized gain pattern of the configurations with maximum gain at angular directions $\theta = -60^\circ$, -30°, 0°, 30° and 60°.

observed that the optimal configuration for each DOA is clearly steered towards the required angular direction achieving a realized gain between 5 dB and 6 dB.

The switch status of the optimal configurations are detailed in the legend of the figure as a binary word $(s_1 s_2 ... s_{12})$ where 0's and 1's represent OFF and ON states respectively. The switch numbering was previously specified in Fig. 5.1. Due to the vertical symmetry of the prototype, the switch configurations steering the beam towards -30° and -60° are symmetric with respect the configurations steered towards 30° and 60° respectively.

A very good agreement is obtained between measurement and simulations, corroborating the antenna model and the RF-transparency of the biasing lines, which have not been included in the simulation model to reduce simulation time. The average measured and simulated realized gain for the presented configurations is 6 dB and the average radiation efficiency is 70%. The measured reflection coefficients are presented in Fig. 5.7. As expected the reflection coefficient of symmetrical configurations is the same and in all cases is below -10 dB at the central frequency.
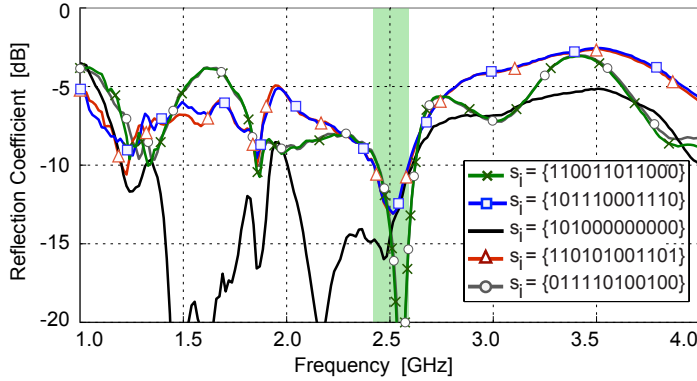
Fig. 5.7: Measured reflection coefficient of the configurations with maximum gain at angular directions $\theta = -60^o$, -30°, 0°, 30° and 60°.

5.1.5 Compound Reconfigurability

While the previous results analyze the one-parameter reconfiguration of frequency and pattern independently, this section explores the two-parameter simultaneous reconfiguration of frequency and pattern. The performance analysis is approached in a similar way as in pattern reconfiguration by maximizing the realized gain of the antenna for each specific frequency and angular direction as detailed in Eq. 5.2. Using this procedure the antenna pattern, reflection coefficient and radiation efficiency are simultaneously considered, reshaping the pattern to maximize directivity while minimizing losses due to the switches and minimizing impedance mismatch.

$$
\{s_j\}_{\text{opt}}(f_0, \theta_0) = \arg \max_{\substack{s_j \in \{0,1\} \\ j=1:12}} G_{\text{realized}}(f_0, \theta_0) =
$$
$$
= \arg \max_{\substack{s_j \in \{0,1\} \\ j=1:12}} D(f_0, \theta_0) \ \eta_{\text{rad}} \ (1 - |s_{11}(f_0)|^2) \tag{5.2}
$$

The results corresponding to the two-parameter reconfiguration are shown in Fig. 5.8. For each frequency and angular direction, the maximum realized gain achieved among all the configurations is represented. It can be observed that simultaneous frequency and pattern reconfiguration can be achieved for frequencies between 2.0 GHz and 4.5 GHz and angular directions between -80° and 80°, obtaining realized gains between 4 dB and 8 dB.

Although the maximum achievable gain is a key parameter to quantify reconfiguration capability, to provide a better characterization it is also important to understand how different the resulting radiation patterns are. To this purpose, for each specific frequency, the patterns that maximize gain for each angular direction have been plotted, removing those which a high degree of similarity. This process has been applied to frequencies covering the frequency reconfiguration range, from 1.5 GHz to 5.5 GHz in steps of 1 GHz, and the resulting patterns are presented in Fig. 5.9. Notice that
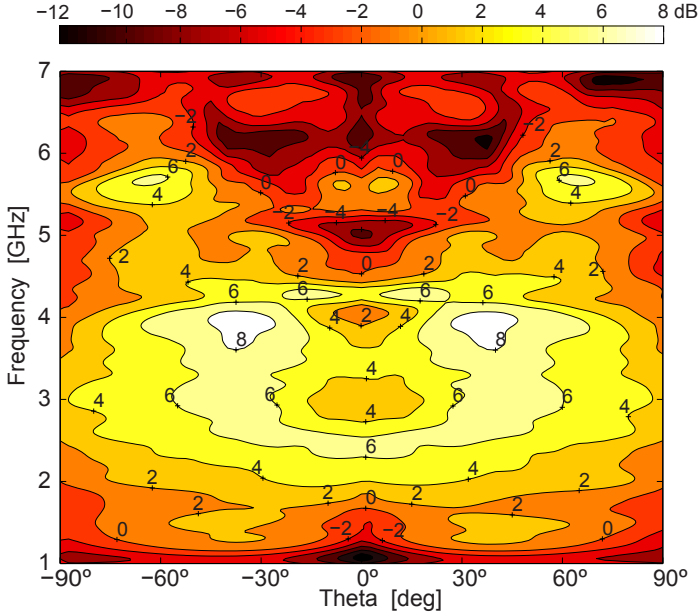
Fig. 5.8: Realized gain of the optimal configuration for each frequency and angular direction.

as expected, the upper envelope of the presented patterns at each frequency is equal to the corresponding horizontal cut of the graph in Fig. 5.8. It can be observed that maximum reconfiguration capability is obtained at 2.5 GHz and 3.5 GHz, where 5 and 4 different patterns can be synthesized respectively, covering the whole angular range. At 4.5 GHz it is also possible to generate 4 different patterns, however, angular directions close to $\theta = 0^\circ$ can not be covered. Reconfiguration capabilities decrease when we move towards the frequency reconfiguration limits, being possible to generate only 2 different patterns at 1.5 GHz and 5.5 GHz. As expected, for higher frequencies the pattern tends to shift towards horizontal directions due to the electrical length increase of the ground plane.

It is important to notice that a high relative number of well-matched configurations at a certain frequency does not imply a rich pattern reconfigurability at that frequency. This is the case of this particular prototype. At 3.5 GHz a high reconfigurability is obtained although the relative number of well-matched configurations is only a 2%, which correspond to approximately 90 well-matched configurations. On the other hand, at 1.5 GHz almost 50% of all configurations are well-matched but the reconfiguration level is relatively low with basically two different radiation patterns.

Besides the previously presented high-gain patterns, the presented prototype can also generate common monopole-type omnidirectional patterns. This behavior can be achieved by using symmetric configurations. Due to the symmetry on the surface currents the radiation pattern is symmetric and has a null in $\theta = 0^\circ$ direction. In Fig. 5.10, the pattern of the maximum-gain symmetric configurations is represented for each one of the previously analyzed frequencies. In pixel antennas it is usually very

(a) f = 1.5 GHz

(b) f = 2.5 GHz

(c) f = 3.5 GHz

(d) f = 4.5 GHz

(e) f = 5.5 GHz
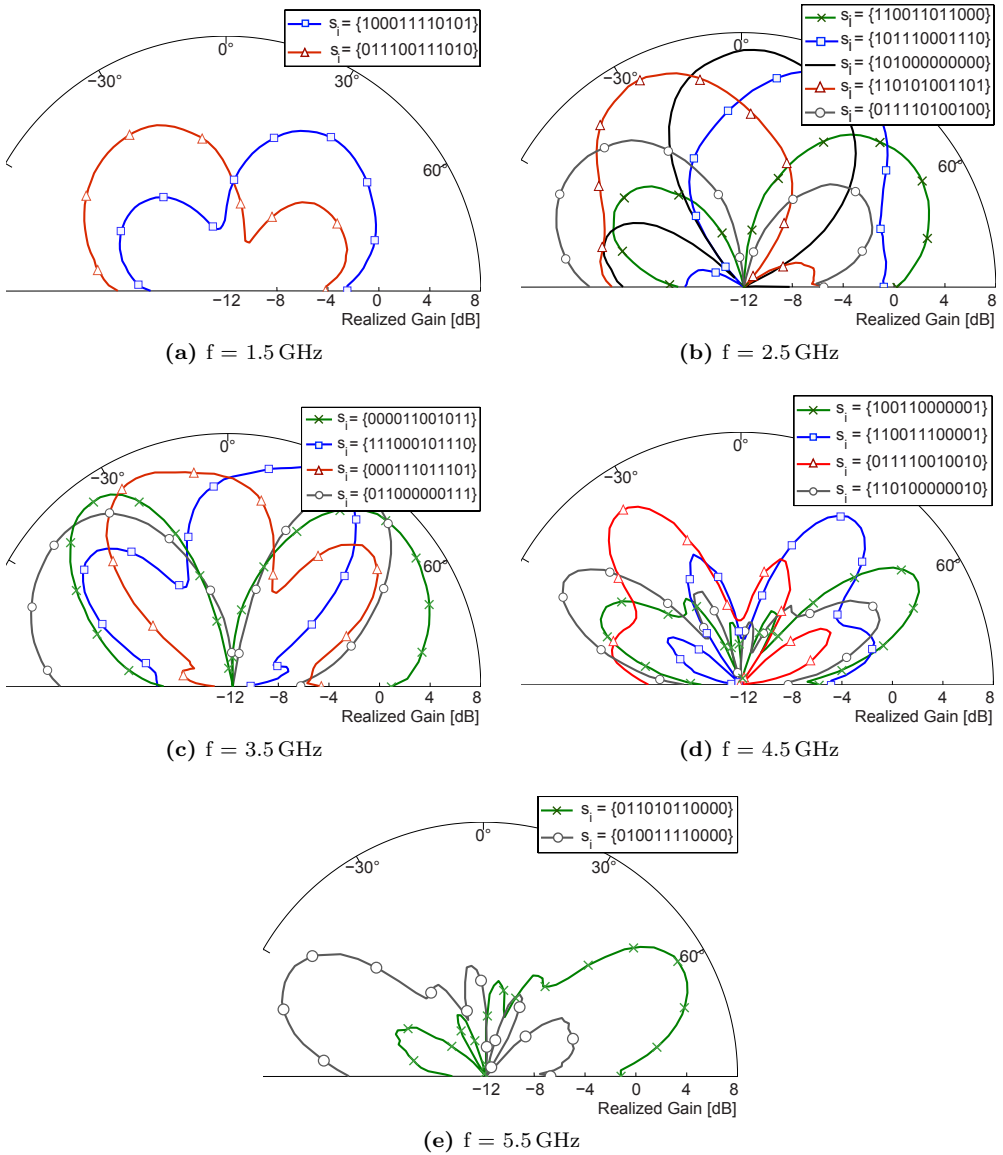
Fig. 5.9: Realized gain patterns of the maximum-gain configurations.

difficult to physically interpret the resulting configurations, however in this case one can easily notice that as the frequency increases, the optimal configuration has fewer active switches in order to reduce the physical length of the antenna.

The presented prototype provides useful insight on the resulting reconfiguration properties of pixel antennas after applying a multi-size pixel geometry and an aggres-
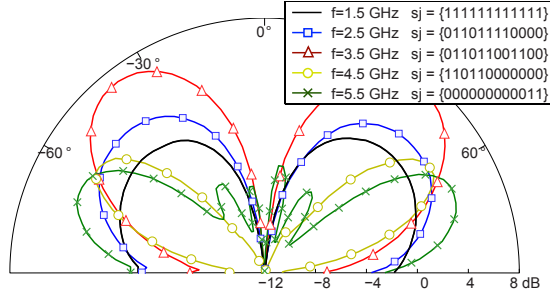
Fig. 5.10: Realized gain patterns of the omnidirectional configurations.

sive switch reduction approach. It has been demonstrated that even for small pixel structures ($\frac{1}{2}\lambda_0 \times \frac{1}{2}\lambda_0$) with only 12 switches, it is possible to achieve a 1:6 frequency reconfiguration range, up to 5 different radiation patterns covering a 180° angular range and simultaneous reconfigurability of the operating frequency and radiation pattern.

5.1.6   Interference Rejection

Besides the previous in-band operational characteristics, the pixel monopole can take advantage of its reconfiguration capabilities to provide interference rejection capability. It is well-known that multi-user wireless systems, such are WLAN or cellular networks, are very often limited by inference [132]. Interferences between users reduce the system reliability, produce a significant impact over the data and bit error rates, and eventually limit the maximum number of users in the system. The effects of interferences can be effectively mitigated by using antenna pattern diversity. Traditionally, adaptive arrays have been used [133], however they require a large size and a complex biasing network. These drawbacks are alleviated using parasitic reconfigurable apertures [24], however the resonant nature of the parasitic elements limits the frequency range of operation provided by this solution. The antenna here presented is a wideband alternative to interference rejection based on the combination of frequency and pattern reconfiguration.

The reconfiguration capabilities of the antenna are used to reject interferences in a line-of-sight scenario with one incident interference as described in Fig. 5.11. The directions of arrival of the signal (θ_s) and the interference (θ_i) are statistically distributed over a 120° range, and their frequencies (f_s, f_i) are in a frequency range from 2 GHz to 4 GHz.

Frequency reconfiguration can be used to reject interferences by synthesizing configurations with a low reflection coefficient for the signal frequency and a high reflection coefficient for the interfering frequency. The performance of the antenna is evaluated based on the realized Signal-to-Interference Ratio (SIR). In this situation the Signal-to-Interference Ratio (SIR) of the frequency reconfigurable antenna is computed as the maximum signal-to-interference ratio among all the configurations that provide an average gain above a certain threshold. The previous definition is expressed by the
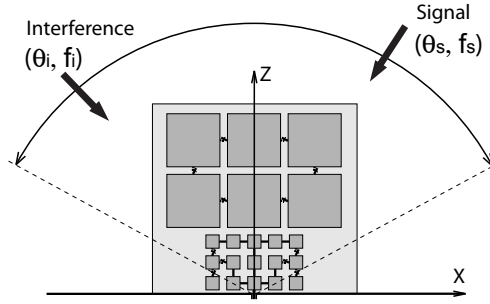
Fig. 5.11: Line-of-sight scenario with one incident interference.
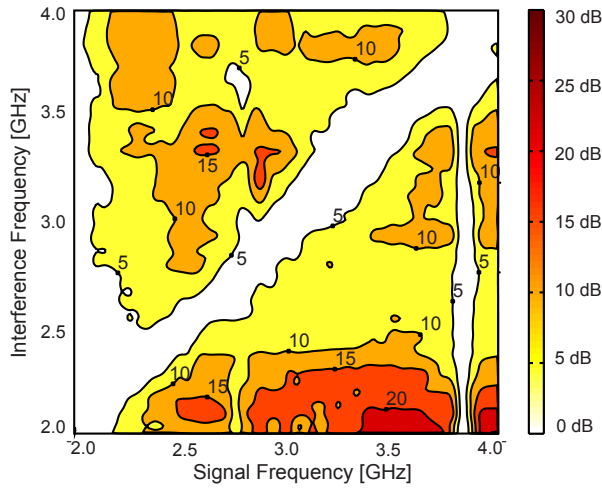
Fig. 5.12: Interference rejection level using only frequency reconfiguration (SIR_1).

following equation

$$SIR_1(f_s, f_i) = \max_{\substack{j=1..N \\ G_{av}^j(f_s)>G_{th}}} \frac{G_{av}^j(f_s)}{G_{av}^j(f_i)} \tag{5.3}$$

where G_{th} is the minimum required gain for the signal and G_{av}^j is the average gain of the jth configuration over the angular zone of interest

$$G_{av}^j(f_s) = \frac{1}{2\Delta\theta} \int_{-\Delta\theta}^{\Delta\theta} G^j(\theta, f_s) d\theta \tag{5.4}$$

The measured interference rejection is represented in Fig. 5.12 for a minimum gain (G_{th}) of $0\,\text{dB}$. The average rejection for the presented frequency range is $8\,\text{dB}$. As expected no rejection is possible for in-band interferences, which corresponds to the diagonal of the graph. The interfering frequency needs to be at a relative distance of at least 10% from the signal frequency to achieve rejection rates above $5\,\text{dB}$.
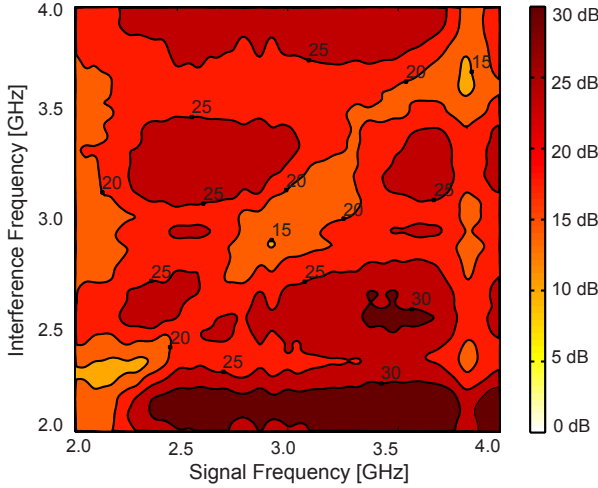
Fig. 5.13: Interference rejection level combining frequency and radiation pattern reconfiguration (SIR_2).

The interference rejection performance of the antenna can be improved by taking advantage of its pattern reconfiguration capabilities in addition to the previous frequency reconfiguration. In this case the antenna achieves a higher interference rejection by combining a high reflection coefficient and a low radiation level for the interference frequency and angular direction. The Signal-to-Interference Ratio is computed by averaging the maximum SIR level for the different DOAs as described in the following equation

$$SIR_2(f_s, f_i) = \left(\tfrac{1}{2\Delta\theta}\right)^2 \int\limits_{-\Delta\theta}^{\Delta\theta} \int\limits_{-\Delta\theta}^{\Delta\theta} SIR(f_s, f_i, \theta_s, \theta_i) \ d\theta_s \, d\theta_i \qquad (5.5)$$

where

$$SIR(f_s, f_i, \theta_s, \theta_i) = \max_{\substack{j=1..N \\ G^j(\theta_s, f_s) > G_{\text{th}}}} \frac{G^j(\theta_s, f_s)}{G^j(\theta_i, f_i)} \qquad (5.6)$$

The resulting rejection level is presented in Fig. 5.13 for the same threshold gain of $G_{\text{th}} = 0$ dB. It can be observed that the interference rejection is significantly improved, resulting in an average rejection of 24 dB which is 16 dB higher than the value achieved by frequency reconfiguration. Unlike the previous case, in-band interferences can also be mitigated, resulting in an average in-band rejection of 18 dB. Not only the average rejection level is improved thanks to pattern reconfigurability, but also the reliability of interference rejection is improved. As seen in Fig. 5.13 an interference rejection of 15 dB can be reliably provided for any combination of signal and interference frequencies between from 2 GHz and 4 GHz.
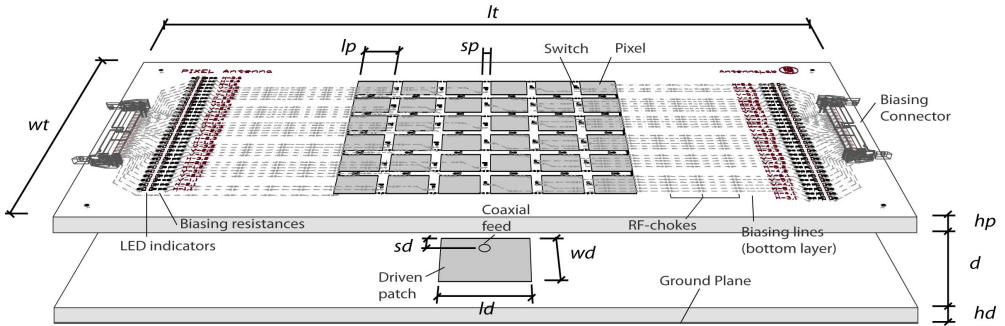
Fig. 5.14: Schematic of the parasitic pixel layer prototype (lp=12, sp=3, hp=1.5, ld=wd=31, sd=10.5, hd=3, lt=240, wt=120, d=variable [units in mm])

5.2 PARASITIC PIXEL LAYER

A prototype of the reconfigurable patch using a parasitic pixel layer is fabricated and characterized in this section. The main design considerations for this prototype have been previously discussed in section 3.4. The fabrication and characterization of the parasitic pixel layer are the central topics of this section. The frequency, radiation pattern and polarization reconfigurability of this design is fully characterized from an experimental perspective.[2]

5.2.1 Parasitic Pixel Layer Prototype

The prototype is a based on the parasitic pixel layer design presented in section 3.4.2 and is designed to operate at a central frequency of 2.5 GHz. The main difference respect to the previously presented design is a larger pixel layer with 6×6 elements to improve the reconfiguration capabilities (at the expense of a larger complexity). Also the distance between the pixel layer and the driven antenna can be manually adjusted to experimentally characterize the effect of this parameter over the antenna reconfigurability.

A schematic along with the dimensions of the different parts and a picture of the antenna design are depicted in Fig. 5.14 and Fig. 5.15, respectively. The patch antenna and the pixel layer are fabricated using Rogers RO4003 substrate. The driven patch antenna is designed to operate at 2.5 GHz and the pixel layer is dimensioned accordingly. The parasitic layer is composed of a 6×6 grid, with an individual pixel size of 12mm ($\lambda/10$) and a overall size of 87mm (0.72λ). Between each pair of adjacent pixels a low-cost PIN diode (NXP BAP 64-02 [134]) has been located operating as an interconnecting RF-switch. The insertion losses and isolation of the switches were presented in section 4.1 and at the antenna operating frequency are 0.3 dB and 12 dB respectively.

Simulation tests have been carried out before the fabrication of the prototype to ensure its reconfiguration capabilities. The simulations have been conducted using

---

[2]This section includes figures and text fragments, sometimes verbatim, from references [JA1].
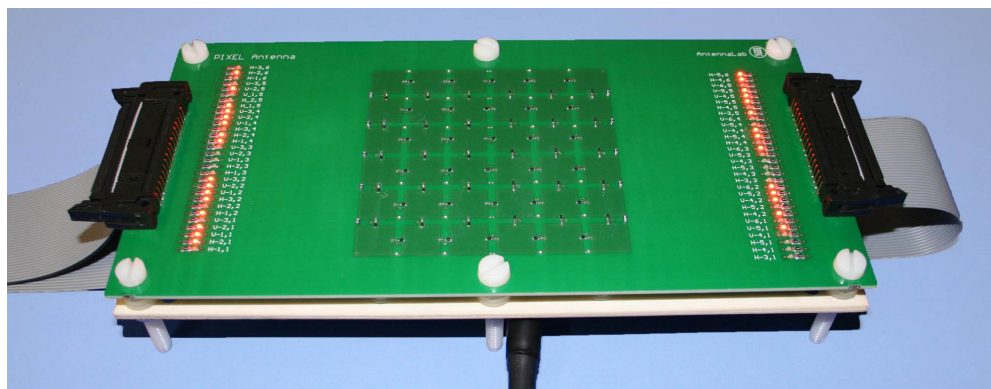
(a)
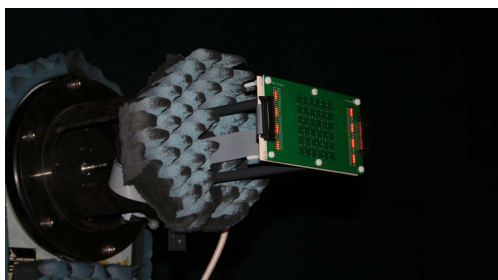
(b)

Fig. 5.15: Picture of the pixel antenna prototype

finite elements method and the switches have been modeled as RLC boundaries. It has been verified that due to the high switch density and the high redundancy, small variations of the pixel size around its design value of $\lambda/10 \times \lambda/10$ do not have considerable effect on the overall reconfiguration capabilities. For this reason the pixel size has been kept at 12×12 mm^2 without needing for further optimization. On the other hand, the distance between the parasitic layer and the driven antenna strongly affects their mutual coupling and thus, it is expected to have a significant impact over the antenna reconfiguration capabilities. The prototype has been designed in such a way that this distance can be modified easily, enabling a parametric characterization of the reconfiguration capabilities for different distances.

The prototype includes 60 switches with independent biasing and control. The biasing strategy followed in this prototype requires one bias line for each switch and two common DC-lines. All the pixels are mutually interconnected by means of inductors and they are in turn connected to the two common bias lines that set a DC-voltage of 5V. The anode of each PIN diode switch is directly connected to the corresponding pixel and its catode is connected to the adjacent pixel through a DC-block capacitor. The switches are biased through 60 independent biasing lines located on the bottom surface of the pixel layer substrate. These lines are split in several short non-resonant sections by means of inductors to ensure their electromagnetic transparency and pre-

vent for any influence over the pixel antenna properties. Each one of these lines include a biasing resistance and a LED indicator to visually inspect the ON/OFF status of each switch.

In order to accurately investigate the effect of the distance between the pixel layer and the driven antenna, vertical interconnections between these two layers have been avoided, thus resulting in a prototype with a relatively complex biasing network. In a commercial prototype, however, all the biasing lines could be located beneath the ground plane of the driven antenna and connected to the switch through multi-layer vias. In this way the bias lines would be naturally shielded by the ground plane and all the inductors located along the bias lines could be removed, except the RF-choke at the switch interconnection. Also the LED indicators and biasing resistances could be removed. In this case, the power consumption of an average of 30 active switches draining a DC-current of 20mA each, would be 0.42W. From a practical perspective, this would lead to a battery lifetime of more than 12 hours for continuous usage on a cell phone battery (1500mAh) and a few days on a laptop battery.

5.2.2 Parasitic Pixel Layer Characterization

The switch ON/OFF status is controlled by a 64-output modular digital I/O (Agilent U2653A) and the U2653A is in turn connected to a PC through USB. The PC is simultaneously connected to the measuring equipment via GPIB. The switch control and the complete set-up diagram is depicted in Fig. 5.16. This set-up is equivalent to the one used in the multi-size pixel antenna characterization and has been used to automatically characterize of the parasitic pixel layer reconfigurability in frequency, radiation pattern and polarization.

The antenna has more than 10^{18} switch configurations, therefore it is not possible to perform an exhaustive characterization for all the different configurations. Instead, an statistical approach has been planned consisting on characterizing a statistic sample of the configuration space. This is a useful approach to understand the average behavior of the antenna because only those antenna properties that can be synthesized by a large number of different configurations are likely to be observed in the sample. The size of the sample is limited by the available characterization time. In the following results a random sample of 20.000 configurations has been chosen, leading to measuring times of a few hours per each distance d between the patch antenna and the pixel layer in the case of frequency measurements, and some days in the case of radiation measurements.

5.2.3 Frequency Reconfigurability

The frequency reconfiguration capabilities of the pixel antenna prototype are discussed in this section. The reflection coefficient of the isolated driven patch antenna is represented in Fig. 5.17. This information is provided as a reference to compare with the reflection coefficient of the pixel antenna configurations provided in Fig. 5.18 for a distance $d=8$mm. The reflection coefficient of each configuration tested is represented as a grey line and some selected configurations evenly distributed over the frequency reconfiguration range are highlighted in black. It can be clearly observed that the resonant frequency of the patch antenna can be finely tuned over a significant frequency
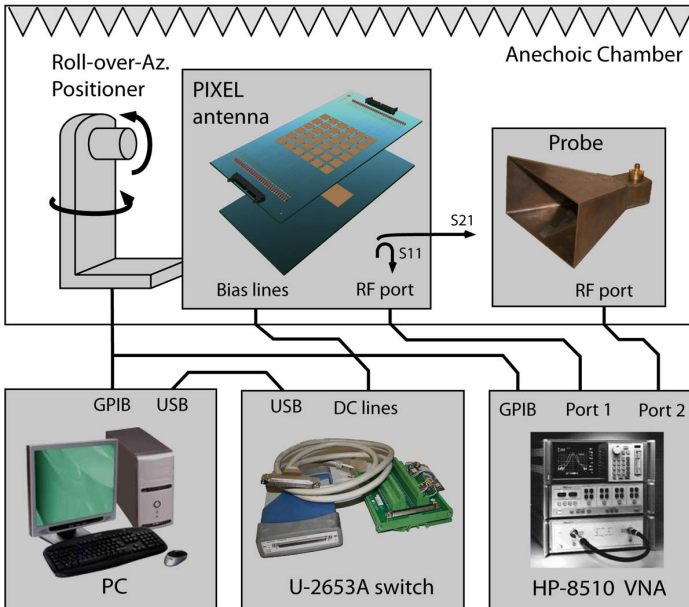
Fig. 5.16: Switch control and measurement set-up
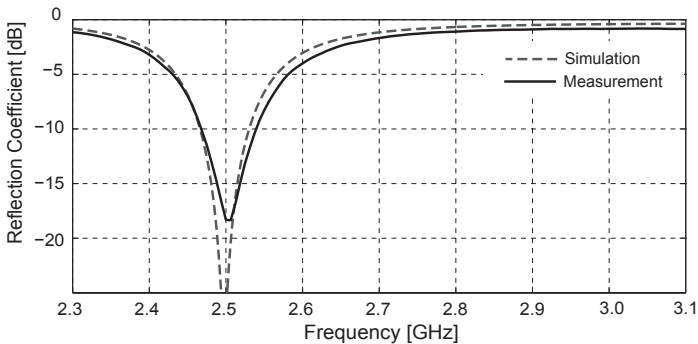
Fig. 5.17: Measured and simulated reflection coefficients of the driven patch antenna.

range. The same highlighted configurations have been simulated and considering the antenna complexity, the agreement with measurements is very good, with differences below 1% between the simulated and measured resonant frequencies. The biasing lines had not been included in the simulation model, indicating that they do not affect substantially the pixel layer properties.

Analogous results are provided in Fig. 5.19 for a distance $d = 3$mm. As expected the frequency reconfiguration range for $d = 3$mm (25.6%) is wider than for $d = 8$mm (12.3%) due to the stronger coupling of the parasitic pixel layer with the driven patch antenna. It is worth noting that regardless of this distance the instantaneous frequency

(a) Measurement

(b) Simulation
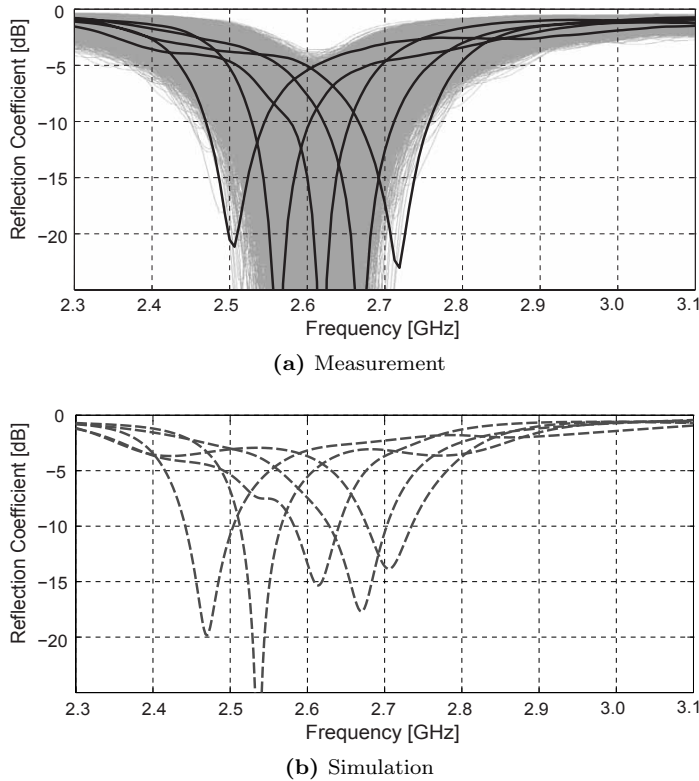
Fig. 5.18: Reflection coefficient of the different pixel antenna configurations for a distance $d=8$mm.

bandwidth (2.8% @-10 dB, 5.2% @-6 dB) is preserved for the different configurations and is almost equal to the patch antenna bandwidth. This behavior makes the parasitic pixel layer ideal for multi-channel applications with adjacent frequency channels which require a narrow instantaneous bandwidth tunable over a larger frequency range. The instantaneous bandwidth of the pixel antenna could be easily improved by using a driven antenna with larger bandwidth.

The effect of the distance has been further analyzed in Fig. 5.20 where the frequency reconfiguration range is presented for several values of d. The strong dependance of the frequency reconfiguration range with the distance can be clearly observed. The reconfiguration bandwidth increases significantly beyond the patch bandwidth when the distance is smaller than $\lambda/5$. As expected this transition occurs at a distance equal to the radianlength $(\lambda/2\pi)$ which determines the transition from low to high coupling due to the influence of the reactive fields [135]. This behavior has also a close relation with the effect of the inter-patch distance in stacked-patch antennas [136, 137], where the resonance of the upper patch dominates for small distances.

In cases where the antenna is reconfigured in real-time, it is also important to quantify the number of well-matched configurations because this value will determine
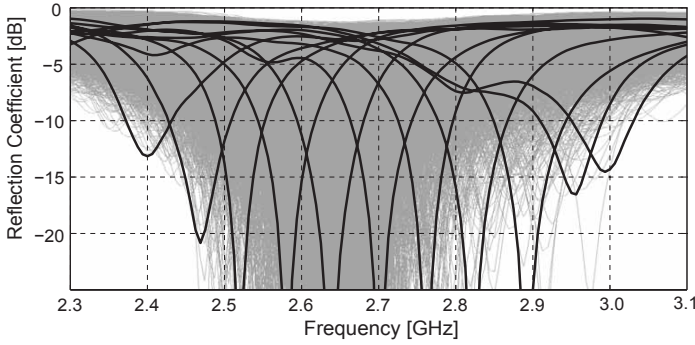
Fig. 5.19: Reflection coefficient of the different antenna configurations for a distance $d = 3$mm.
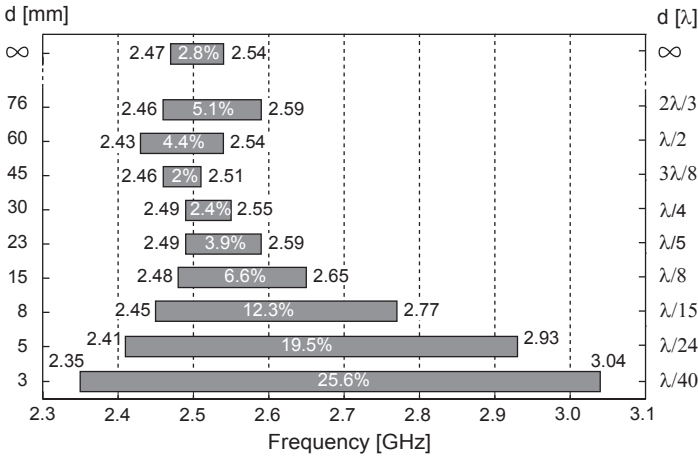
Fig. 5.20: Frequency reconfiguration range of the parasitic pixel layer antenna for different distances.

the training time required. Fig. 5.21 represents the relative number of configurations at each frequency with a reflection coefficient below $-10\,$dB. The first important conclusion from these results is that the frequency reconfigurability of the capacitive pixel layer is much better behaved than in common pixel antennas. In existing pixel antennas, where the pixelation is applied to the active antenna, the number of well-matched configurations changes abruptly with frequency and presents multiple local maximums and minimums as previously shown in Fig. 5.5. In the parasitic pixel layer presented here there exists a global maximum at a central frequency and the number of well-matched configurations decreases monotonically as the frequency deviates from this central frequency. For instance, for $d\!=\!8$mm almost 70% of configurations are well matched at $2.60\,$GHz and as the frequency increases to 2.65, 2.70 and 2.75 GHz, the number of suitable configurations decreases down to 40%, 5% and 0.1%, respectively.

The results in Fig. 5.21 also allow to determine the realistic reconfiguration band-
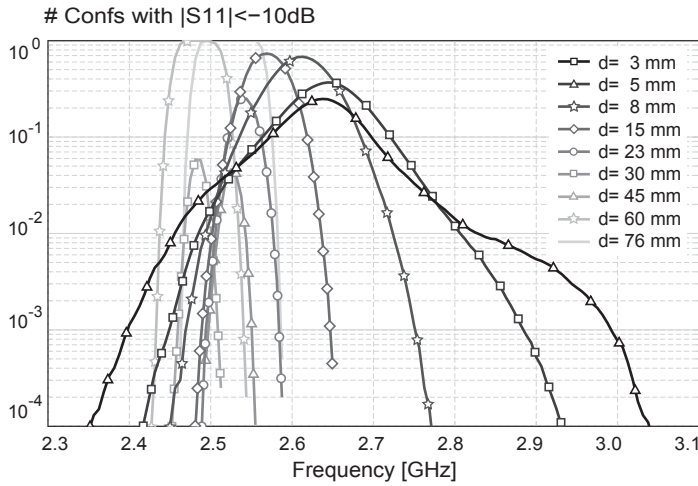
Fig. 5.21: Relative number of configurations with a reflection coefficient below $-10\,\mathrm{dB}$ evaluated for different distances (d).
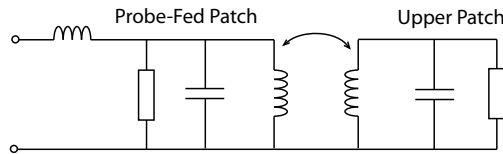
Fig. 5.22: Circuit model of a stacked-patch antenna.

width achieved by the real-time reconfiguration of the antenna depending on the number of configurations tested during the available training time. The reconfiguration range is given by the intersection of the presented curves with a horizontal line set at a level equal to the inverse of the number of configurations tested. For instance, frequency reconfiguration over the interval [2.45 GHz, 2.83 GHz] is achieved for $d=3$mm when one hundred configurations are tested during training (10^{-2} level). However when the number of configurations tested increases up to one thousand (10^{-3} level), the reconfiguration range widens up to [2.40 GHz, 3.00 GHz].

It is also observed that for small distances the antenna tends to resonate at frequencies above the resonant frequency of the patch (2.50 GHz). As expected this behavior reverses when the distance exceeds a quarter-wavelength and the resonance shifts towards lower frequencies. This is the opposite behavior of a typical stacked-patch antenna, where a large upper patch at a very short distance from the driven patch is seen as a capacitive coupling (Fig. 5.22) that lowers the antenna resonance frequency. This result indicates that the pixel layer loads the driven patch with an inductive load. One possible explanation to this phenomenon is the fact that the driven patch sees the pixel layer not as a larger patch but as a slotted surface. To further understand the statistical properties of the pixel surface an additional experiment has been carried out. The number of well-matched configurations has been analyzed for
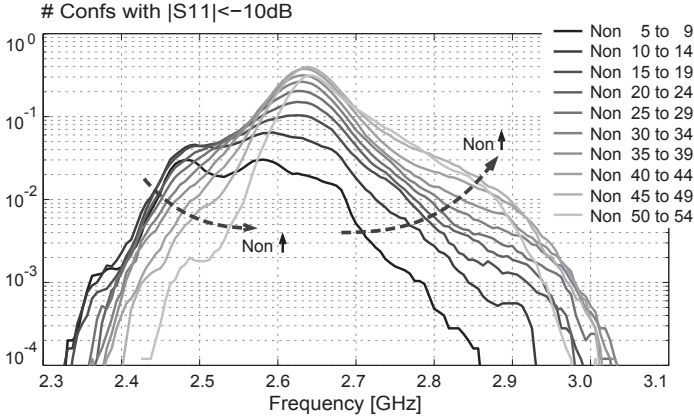
Fig. 5.23: Relative number of configurations with a reflection coefficient below $-10\,\text{dB}$ evaluated for different densities of ON-state switches (N_{on}).

different numbers of active switches (N_{on}) and the results are presented in Fig. 5.23 for $d = 3\text{mm}$. It can be observed that the lowest resonance frequencies are provided by highly disconnected configurations (N_{on} low). On the other hand, the highest resonance frequencies are provided by highly connected configurations (N_{on} high). In fact, for highly connected configurations the pixel structure resembles a slotted metallic sheet. As the number of active switches increases, the length of these slots shortens, thus increasing their inductive behavior and shifting the antenna resonance towards higher frequencies.

5.2.4   Compound Reconfigurability

Reconfiguration parameters and measurement procedure

This section presents the compound reconfiguration capabilities of the parasitic pixel layer, where several antenna parameters are simultaneously adjusted. The three main antenna parameters, which are the operation frequency, radiation pattern and polarization, are simultaneously tuned. The different parameters of operation are depicted in Fig. 5.24 and are subsequently detailed.

$$
\begin{aligned}
&\text{6 freq.:} &&f \in \{\ 2.4,\ 2.5,\ 2.6,\ 2.7,\ 2.8,\ 2.9\ \text{GHz}\ \} \\
&\text{5 DOA's:} &&\theta_{\text{DOA}} \in \{-30^{\text{o}},\ 0^{\text{o}},\ 30^{\text{o}}\},\ \phi_{\text{DOA}} \in \{0^{\text{o}},\ 90^{\text{o}}\} \\
&\text{4 polariz.:} &&\hat{e}_{\text{pol}} \in \{\ \hat{y},\ \hat{x},\ \tfrac{1}{\sqrt{2}}(\hat{x}+j\hat{y}),\ \tfrac{1}{\sqrt{2}}(\hat{x}-j\hat{y})\ \}
\end{aligned}
\tag{5.7}
$$

The antenna configuration has been experimentally optimized for each of the 120 combinations of resonant frequencies, directions-of-arrival (DOA) and polarizations defined in Eq. (5.7). The measurement procedure was specifically designed to reduce the measuring time of the previous parameter set to one week. The procedure was divided in two stages. In the first stage, for each combination of frequency, angular direction and polarization, the partial realized gain was measured for multiple antenna
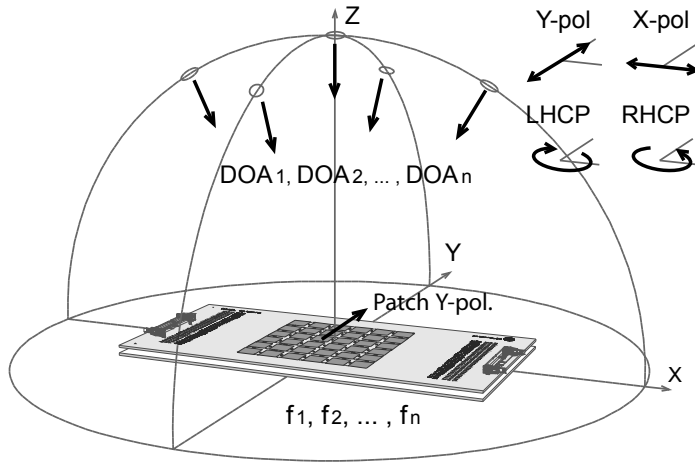
Fig. 5.24: Representation of the reconfiguration parameters (operation frequency, polarization, and beam direction) considered in compound reconfiguration.

Tab. 5.1: Gain of the driven patch antenna [dB]

		Y-pol.	X-pol.	LHCP	RHCP
	f = 2.4	4.7	$<$−30	1.7	1.7
	f = 2.5	7.1	$<$−30	4.1	4.1
XZ plane	f = 2.6	4.4	$<$−30	1.4	1.4
$\theta = 0^o$	f = 2.7	0.9	$<$−30	−2.1	−2.1
	f = 2.8	-1.0	$<$−30	−4.0	−4.0
	f = 2.9	-2.6	$<$−30	−5.6	−5.6

configurations. The same 20.000 configurations as in the previous section were measured in this case. For each of the 120 parameter combinations the configuration with highest partial realized gain was selected as the optimal configuration. In the second stage of the measurement, the radiation patterns of the optimal configurations were measured.

For brevity reasons the word *gain* will be used in this document to refer to the partial realized gain defined in [1]. According to this definition all the losses due to impedance mismatch, polarization mismatch and efficiency are taken into account. This parameter provides the best description of the antenna performance in an scenario where the antenna frequency, pattern and polarization are simultaneously reconfigured.

To serve as comparison for the pixel antenna characteristics that will be presented in this section, the radiation pattern of the isolated driven patch antenna is presented in Fig. 5.25. The gain of the driven patch is also provided in Table 5.1 for the different frequencies and polarizations.
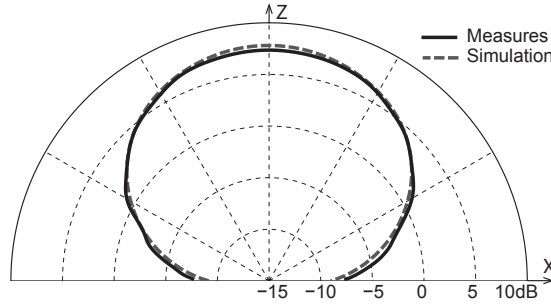
Fig. 5.25: Gain of the driven patch antenna over the XZ-plane at $f = 2.7\,\text{GHz}$.
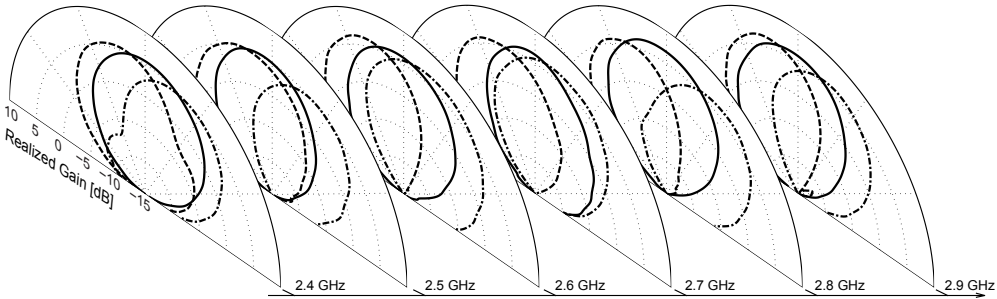
Fig. 5.26: Measured gain for $d = 3\text{mm}$, XZ-plane, $\hat{y}$-pol and multiple frequencies.

Compound reconfiguration capabilities

The compound reconfiguration has been characterized for the pixel antenna with $d = 3\text{mm}$, which among the different distances tested is the one that provides the highest frequency reconfigurability. The measured radiation patterns are represented in Fig. 5.26 for the optimal configurations with DOA's over the XZ-plane and linear polarization in the $\hat{y}$ direction (same as the driven patch). It can be observed that the measured radiation patterns are effectively steered towards the directions specified in Eq. (5.7) and the realized gain is between 5 dB and 6 dB for all the angular directions and frequencies. Furthermore, the optimal radiation patterns are very similar for all the different frequencies, which is an important requirement in antenna reconfiguration. This means that the antenna not only can tune its operation frequency over the frequency range specified in the previous section, but also the pattern integrity is preserved.

The simulated radiation patterns at the center of the frequency reconfiguration range are presented in Fig. 5.27. There is a very good agreement between simulations and measurements in terms of pattern shape and gain level.

The antenna can also steer the radiation beam over the YZ-plane as shown in Fig. 5.28. The gain achieved over the YZ-plane is similar as in the XZ-plane, as well
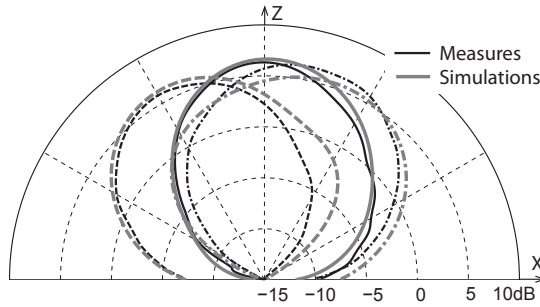
Fig. 5.27: Comparison between simulated and measured gain for $d=3$mm, XZ-plane, $\hat{y}$-pol and $f=2.7$ GHz.
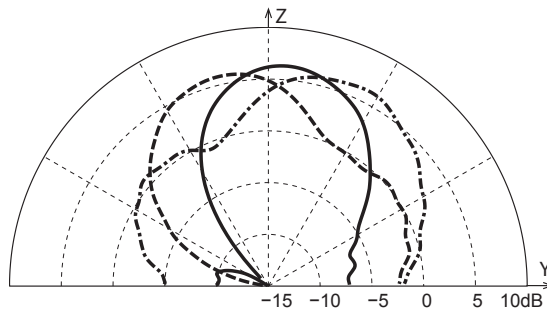
Fig. 5.28: Measured gain for $d=3$mm, YZ-plane, $\hat{y}$-pol and $f=2.7$ GHz.

as is the pattern shape. Directions of arrival up to $\theta = 60^{\circ}$ over these two planes were also considered during the initial measurements, however the measured patterns were not very different from those steering towards $\theta=30^{\circ}$. These results lead to the conclusion that the steering range of the antenna is $\pm 30^{\circ}$ for both XZ and YZ planes.

The parasitic pixel antenna not only can tune its frequency and steer its radiation pattern, but it can also adjust its polarization. Fig. 5.29 represents the gain of the optimal configurations for the three additional polarizations considered: linear $\hat{x}$-oriented, left-hand circular polarization (LHCP) and right-hand circular polarization (RHCP). The loss due to polarization mismatch has been already taken into account in these radiation patterns. It is observed that beam-steering is also possible for the different polarizations. However, the radiation patterns tend to have higher sidelobes. The achieved gain is also smaller than for the $\hat{y}$-polarized case, however it can easily reach values of 4 dB even for the $\hat{x}$-polarization. This value indicates that the pixel surface is able to produce strong currents in the transverse direction which are dominant for the $\hat{x}$-polarization mode and that are of similar magnitude as $\hat{y}$-components for the circular polarization modes.

The radiation patterns presented thus far illustrate the compound reconfiguration capabilities of the pixel layer. For the sake of completeness, Table 5.2 provides the gain achieved by each operating mode for all the different parameter combinations.
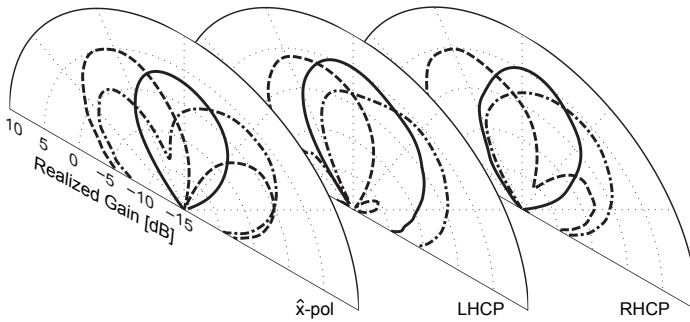
Fig. 5.29: Measured gain for XZ-plane, $d = 3\,\text{mm}$, multiple polarizations and $f = 2.7\,\text{GHz}$.

An analysis of the gain with respect to each parameter reveals some interesting conclusions. To enable this analysis the data in Table 5.2 has been averaged with respect to each one of the three parameters (frequency, direction-of-arrival and polarization) and the resulting average gain is presented in Table 5.3.

The antenna gain increases smoothly when the frequency changes from 2.5 GHz to 2.8 GHz. This is expected as the pixel layer becomes electrically larger at higher frequencies and thus the beam-steering capabilities are enhanced. However, when the frequency reaches 2.9 GHz the gain drops. This is due to the fact that the largest number of well-matched configurations is obtained at the central frequencies as shown in Fig. 5.19. Therefore a higher loss due to impedance mismatch is expected at the lower and upper bound frequencies. This is in fact corroborated by the reflection coefficient data presented in Table 5.4. The loss due to impedance mismatch is higher than 1 dB at the lower and upper bound frequencies, while at the center frequencies it is below 0.5 dB.

It is also observed that although the antenna can steer the beam in both XZ and YZ planes, the beam-steering capabilities are higher in the XZ plane which corresponds to the H-plane of the driven patch antenna. This is due to the fact that currents over the pixel layer tend to flow in the $\hat{y}$ direction. This current direction does not affect the XZ pattern but produces an additional $\cos\theta$-taper over the YZ plane. In fact, the gain difference between the two planes is approximately 1 dB, which is approximately the value of the previous taper at $\theta = 30°$.

The antenna gain with respect to the polarization also behaves as expected. The highest gain is achieved for the $\hat{y}$-polarization which is the same as the driven antenna polarization. On the other hand, the lowest gain corresponds to the transverse polarization ($\hat{x}$-polarization). The differences in gain are basically due to the lower number of configurations producing a polarization different from that of the patch. However, the average polarization efficiency is relatively high as shown in Table 5.5. As expected, the polarization efficiency for $\hat{y}$-polarization is almost 100%. On the other hand, the polarization efficiency for the $\hat{x}$-polarization is almost 80%, indicating only 1 dB of loss due to polarization mismatch.

Tab. 5.2: Par. Pixel Ant. $d=3$mm: Maximum Gain [dB]

Partial Realized Gain		XZ plane			YZ plane	
		$-30°$	$30°$	$0°$	$-30°$	$+30°$
Y-pol	f = 2.4	5.0	5.0	5.5	3.6	5.2
	f = 2.5	4.9	4.9	5.0	4.8	5.2
	f = 2.6	6.2	6.0	6.1	5.7	6.3
	f = 2.7	5.8	5.8	6.4	4.8	6.3
	f = 2.8	5.7	6.4	6.8	5.1	6.7
	f = 2.9	5.9	5.6	6.3	3.7	6.4
X-pol	f = 2.4	3.5	1.8	1.1	-0.4	-0.5
	f = 2.5	3.4	2.1	1.3	0.3	1.6
	f = 2.6	4.0	3.1	2.6	1.2	1.1
	f = 2.7	5.0	3.8	3.0	2.1	2.1
	f = 2.8	4.9	4.9	3.5	2.1	2.6
	f = 2.9	5.1	4.0	3.4	2.0	1.9
LHCP	f = 2.4	4.1	3.1	4.0	2.3	3.6
	f = 2.5	4.6	3.4	3.6	3.4	4.3
	f = 2.6	4.9	4.0	4.9	3.9	4.8
	f = 2.7	4.2	4.3	5.4	3.1	4.3
	f = 2.8	4.9	5.0	6.1	3.5	5.1
	f = 2.9	4.1	5.1	5.0	2.8	5.5
RHCP	f = 2.4	2.2	3.4	4.2	2.8	3.4
	f = 2.5	3.1	4.5	3.3	1.8	4.2
	f = 2.6	3.9	5.6	4.8	3.3	5.2
	f = 2.7	4.9	4.3	5.3	3.5	4.1
	f = 2.8	4.6	4.4	5.3	3.0	5.1
	f = 2.9	3.9	4.1	4.7	3.1	3.9

Effect of the distance between the driven antenna and the pixel layer

In the previous section it was observed that the frequency reconfigurability of the pixel layer increases when the distance (d) to the driven antenna is reduced. Also, the effect of this distance over the radiation pattern and polarization reconfigurability merits an investigation. To this end, the pixel antenna has been characterized for a distance $d=8$mm and these results are compared with those of corresponding to $d = 3$mm.

The measured radiation patterns do not present any significant shape variation for the new distance. As an example, Fig. 5.30 shows the radiation pattern of the pixel layer with $d=8$mm over the XZ-plane, for a frequency of 2.7 GHz and $\hat{y}$-polarization.

Tab. 5.3: Par. Pixel Ant. $d=3$mm: Average Gain [dB]

Frequency	Gain	DOA	Gain	Polariz.	Gain
2.4 GHz	3.1	XZ -30°	4.5	$\hat{x}$-pol	5.6
2.5 GHz	3.5	XZ +30°	4.4	$\hat{y}$-pol	2.6
2.6 GHz	4.4	0°	4.5	LHCP	4.2
2.7 GHz	4.4	YZ -30°	3.0	RHCP	4.0
2.8 GHz	4.8	YZ +30°	4.1		
2.9 GHz	4.3				

Tab. 5.4: Par. Pixel Ant. $d=3$mm: Average Reflection Coefficient

Freq.	2.4	2.5	2.6	2.7	2.8	2.9
$|S_{11}|$ [dB]	-6.2	-8.1	-10.4	-13.1	-7.9	-6.8
L_{mismatch} [dB]	1.2	0.7	0.4	0.2	0.8	1.0

Tab. 5.5: Par. Pixel Ant. $d=3$mm: Average Polarization efficiency

Polarization	$\hat{y}$-pol	$\hat{x}$-pol	LHCP	RHCP
η_{pol}	96%	79%	85%	89%
η_{pol} [dB]	-0.2	-1.0	-0.7	-0.5

The results presented in this figure are very similar to the corresponding patterns presented in Fig. 5.27 for $d=3$mm.

Although the pattern shape is qualitatively the same for the different distances, the level of gain achieved strongly depends on this parameter. To evaluate this dependance, the maximum gain achieved by the pixel layer is represented in Table 5.6 for the different parameters and compared with the values in Table 5.2 corresponding to
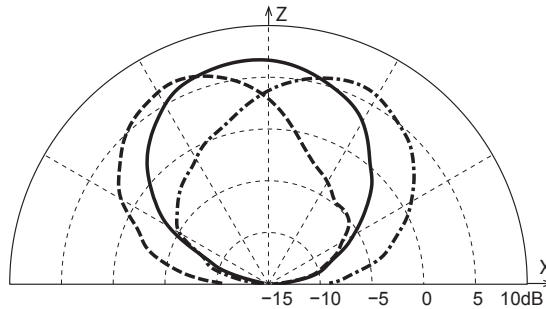
Fig. 5.30: Measured gain for $d=8$mm, XZ-plane, $\hat{y}$-pol and $f=2.7$ GHz.

Tab. 5.6: Par. Pixel Ant. $d=8$mm: Maximum Gain

		XZ plane			YZ plane	
		$-30°$	$30°$	$0°$	$-30°$	$+30°$
Y-pol	f = 2.4	4.9	4.8	6.1	3.4	4.9
	f = 2.5	6.8	5.9	6.2	4.8	5.9
	f = 2.6	7.6	7.3	7.3	5.7	7.1
	f = 2.7	6.6	6.1	6.7	4.7	5.6
	f = 2.8	6.3	6.3	6.1	4.4	5.3
	f = 2.9	4.1	4.6	5.5	1.6	3.9
X-pol	f = 2.4	1.6	1.6	0.3	0.3	3.3
	f = 2.5	3.5	3.0	1.9	1.2	1.8
	f = 2.6	4.0	4.3	4.8	3.1	4.4
	f = 2.7	3.9	3.4	2.7	2.2	2.2
	f = 2.8	3.8	3.3	1.6	1.7	1.4
	f = 2.9	2.0	1.6	-0.4	-0.5	-0.7

$d=3$mm. The values for which the pixel antenna with $d=8$mm performs better are represented in black, while the rest is represented in grey.

It can be clearly observed that the pixel antenna with higher distance performs better than its low-distance counterpart for frequencies close the patch resonance. For the central frequencies of 2.5 GHz and 2.6 GHz the pixel antenna with $d=8$mm reaches an average gain 1 dB higher than the gain achieved with $d=3$mm. However, the situation is reversed when the frequency moves away from the patch resonance.

Following the previous observation it can be noticed that the distance between the driven antenna and the pixel layer can be used as a design parameter to balance the reconfiguration capabilities among the different parameters of reconfiguration. Low distances benefit frequency reconfiguration and preserve a moderate reconfigurability in radiation pattern and polarization. On the other hand, for higher distances the frequency reconfiguration range shrinks but the pattern and polarization reconfiguration is improved.

FIGURES-OF-MERIT FOR PIXEL AND RECONFIGURABLE ANTENNAS

O NE of the factors that slows down the implementation of RAs in current commu-
nications systems is the lack of quantification figures that determine the system-
level benefits produced by the replacement of common antennas by RAs [2]. Closely
related to this fact is the lack of figures-of-merit (FoM) that quantify the reconfigura-
tion capabilities of reconfigurable antennas and pixel antennas.

In this chapter, the average gain provided by pattern and polarization reconfig-
urable antennas is analyzed. Based on this performance evaluation, figures-of-merit of
pattern reconfigurability are subsequently derived. Two different figures-of-merit have
been obtained. The first FoM is suitable for antennas with a moderate number of con-
figurations where the optimal configuration at each specific time can be determined.
The second FoM is suitable for antennas with a very large number of configurations
where a sub-optimal selection algorithm is used to determine the configuration used
at each specific time.[1]

6.1 PERFORMANCE EVALUATION FOR RADIATION RE-CONFIGURABILITY

6.1.1 Formulation for pattern and polarization reconfiguration

The beam-switching capabilities of a pattern reconfigurable antenna can be exploited
to maximize the gain budget in line-of-sight applications where the relative position
and/or orientation between the transmitting and receiving antennas is not preserved
over time. From the RA perspective it is equivalent that the modifications in their rel-
ative position and orientation are produced by its own movement or by the movement
of the other antenna in the link. Due to reciprocity, it is also equivalent that the RA
operates as a transmitter or as a receiver. Without loss of generality it is assumed that
the RA is physically static in a scenario with an incoming plane wave from a variable
angular direction and with a variable polarization as represented in Fig 6.1. For a RA
with N different configurations, being $\{G_R^i\}_{i=1}^N$ its corresponding radiation patterns,

---

[1]This section includes figures and text fragments, sometimes verbatim, from reference [JA3].
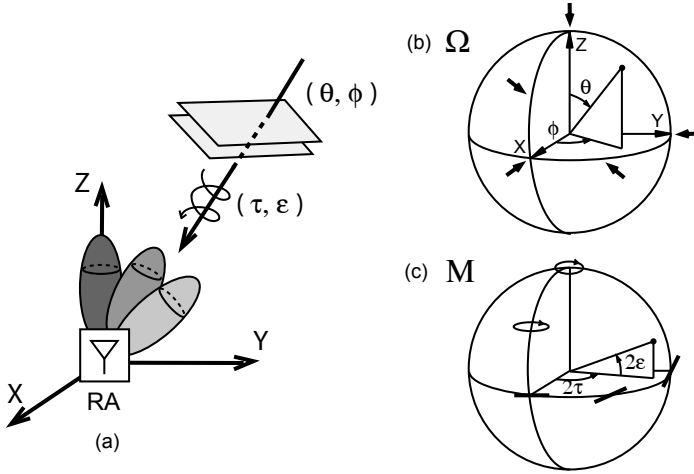
Fig. 6.1: (a) General scenario where the RA receives a plane wave with a specific direction-of-arrival and a polarization. The angular direction of arrival and polarization are respectively represented over (b) the spherical coordinate system Ω and (c) the Poincaré sphere M.

the maximum achievable gain for each set of parameters of the incoming wave can be written as follows,

$$g_{R,\max}(\theta, \phi, \tau, \epsilon) = \max_{i=1..N} G_R^i(\theta, \phi) \ |\hat{e}^i(\theta, \phi) \cdot \hat{e}^*(\theta, \phi, \tau, \epsilon)|^2 \qquad (6.1)$$

where (θ, ϕ) represent the incoming wave direction, (τ, ϵ) are the polarization tilt angle and eccentricity, $\hat{e}$ is the polarization vector and $\{\hat{e}^i\}$ is the polarization of each RA configuration. The tilt angle is defined respect to an arbitrarily chosen reference vector $\hat{e}_{\mathrm{ref}}$ at each direction (θ, ϕ). In the case of continuously tunable antennas the maximum gain would be evaluated over a continuous range instead of a discrete space, preserving the validity of all properties and derivations presented in this paper.

Due to the practical scope of this formulation, mismatch losses have been included by considering realized gains. The notation used in this paper follows the standard [1], where G_R and g_R represent realized gain and partial realized gain respectively.

The natural figure-of-merit of a RA regarding the gain/link budget in a line-of-sight scenario is the average of the maximum gain for all angular directions and possible polarizations of the incoming wave. The average maximum gain is represented by $\overline{g}_{R,\max}$ and can be computed with the following expression

$$\overline{g}_{R,\max} = \iint_{\Omega \times M} g_{R,\max}(\theta, \phi, \tau, \epsilon) \, P_{\Omega \times M}(\theta, \phi, \tau, \epsilon) \, \mathrm{d}\Omega \, \mathrm{d}M \qquad (6.2)$$

where Ω and M represent the solid angles over the spatial angular directions and the Poincaré sphere respectively.

The differentials $\mathrm{d}\Omega$ and $\mathrm{d}M$ are computed as follows

$$\mathrm{d}\Omega = \sin\theta \, \mathrm{d}\theta \, \mathrm{d}\phi, \qquad \mathrm{d}M = 4\cos 2\epsilon \, \mathrm{d}\tau \, \mathrm{d}\epsilon \qquad (6.3)$$

where $0 \leq \theta \leq \pi, \; 0 \leq \phi \leq 2\pi, \; -\pi/4 \leq \epsilon \leq \pi/4, \; 0 \leq \tau \leq \pi$.

$P_{\Omega \times M}$ is a weighting function representing the direction-polarization statistics of the incoming wave (or equivalently, the statistics of the relative position/orientation between the two antennas) which satisfies the following normalization equation

$$\iint_{\Omega \times M} P_{\Omega \times M}(\theta, \phi, \tau, \epsilon) \, \mathrm{d}\Omega \, \mathrm{d}M \; = \; 1 \tag{6.4}$$

The definition of $\overline{g}_{R,\max}$ has certain similarities with the Mean Effective Gain (MEG) used to characterize antennas in mobile radio environments [138, 139]. However, these two concepts are essentially different: the latter evaluates non-reconfigurable antennas in a multipath environment, while the former characterizes radiation reconfigurable antennas in a variable line-of-sight scenario.

A common scenario to illustrate the modeling of the incoming wave statistics using the weighting function $P_{\Omega \times M}$ is depicted in Fig. 6.2. In it the RA is located in a room corner and receives a signal from a movable fully-rotatable linearly polarized device. For this configuration only the region $x, y \geq 0$ and $z \leq 0$ of the Ω-sphere of $P_{\Omega \times M}$ is non-zero, since it corresponds to the only possible locations for the transmitter. Similarly, due to the linear polarization of the transmitter and taking into account its free rotation, only the equator of the M-sphere is non-zero, as shown in the colored regions in Fig. 6.2. Therefore, the weighting function for this scenario would be

$$P_{\Omega \times M}(\theta, \phi, \tau, \epsilon) = \begin{cases} \frac{1}{2\pi^2} \, \delta(\epsilon) & \pi/2 \leq \theta, \; 0 \leq \phi \leq \pi/2 \\ 0 & \text{elsewhere} \end{cases} \tag{6.5}$$

and the corresponding average gain

$$\overline{g}_{R,\max} = \int\limits_{0}^{\pi} \int\limits_{0}^{\pi/2} \int\limits_{\pi/2}^{\pi} g_{R,\max}(\theta, \phi, 0, \tau) \, \tfrac{2}{\pi^2} \sin\theta \, \mathrm{d}\theta \, \mathrm{d}\phi \, \mathrm{d}\tau \tag{6.6}$$

Although the average gain $\overline{g}_{R,\max}$ provides the most fundamental information about the RA performance, in some cases it is desired to obtain a richer statistical information, for instance the variability of $g_{R,\max}$. This information is provided by its higher order statistical moments such as the standard deviation

$$\sigma^2_{g_{R,\max}} = \iint_{\Omega \times M} \left(g_{R,\max} - \overline{g}_{R,\max} \right)^2 P_{\Omega \times M} \, \mathrm{d}\Omega \, \mathrm{d}M \tag{6.7}$$

Nevertheless, the analysis of the higher order moments is out of the scope of this paper, which will focus on the first order moment of the maximum realized gain, that is the average gain $\overline{g}_{R,\max}$.

6.1.2 Formulation for pattern reconfigurability

The average maximum gain given by (6.2) is a general formulation valid for both pattern and polarization RAs. The previous expression can be simplified for the most
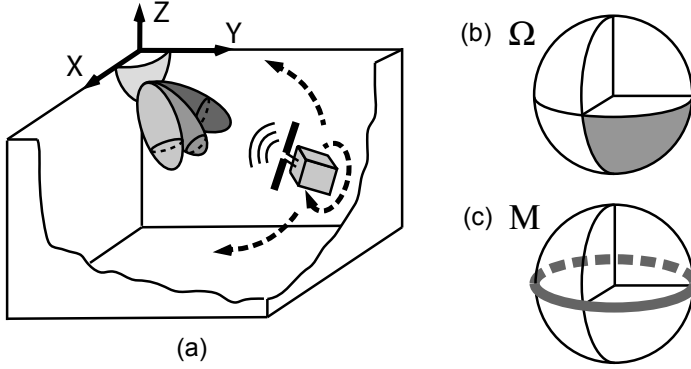
Fig. 6.2: (a) Scenario with a RA located in a room corner and a linearly polarized transmit-
ter with random position and orientation. The corresponding $P_{\Omega \times M}$ is represented
over (b) the spherical coordinate system Ω and (c) the Poincaré sphere M.

common scenarios when only radiation pattern reconfiguration is considered. In this
case and taking into account the definition of pattern reconfigurability, the polarization
of the RA is the same for every configuration

$$\hat{e}^i(\theta, \phi) = \hat{e}_{RA}(\theta, \phi), \quad i = 1 \ldots N \tag{6.8}$$

Additionally, the spatial and polarization components of the incoming wave statistics
are independent for many of the scenarios considered in beam-switching applications.
This is true for the three scenarios presented in Fig. 6.3, that will be detailed later
in this section and that cover a significant portion of the scenario casuistic. And it
is also a common assumption in direction-of-arrival and polarization estimation [140].
The spatial-polarization separability is expressed as

$$P_{\Omega \times M}(\theta, \phi, \tau, \epsilon) \;=\; P_{\Omega}(\theta, \phi)\, P_M(\tau, \epsilon) \tag{6.9}$$

where P_{Ω} and P_M satisfy the following normalization

$$\iint_{\Omega} P_{\Omega}(\theta, \phi)\, \mathrm{d}\Omega \;=\; \iint_{M} P_M(\tau, \epsilon)\, \mathrm{d}M \;=\; 1 \tag{6.10}$$

It must be noted that separability depends not only on the scenario but also on the
reference vector $\hat{e}_{\mathrm{ref}}(\theta, \phi)$ polarization that defines the polarization tilt angle. There-
fore, this vector has to be chosen appropriately so the weighting function can be
separated into spatial and polarization components.

Applying (6.8) and (6.9), the average maximum gain can be expressed as follows

$$\overline{g}_{R,\max} = \iint_{\Omega} \left[\max_{i=1..N} G_R^i(\theta, \phi) \right] P_{\Omega}(\theta, \phi)\, \eta_p(\theta, \phi)\, \mathrm{d}\Omega \tag{6.11}$$

where

$$\eta_p(\theta, \phi) = \iint_{M} |\hat{e}_{RA}(\theta, \phi) \cdot \hat{e}^*(\tau, \epsilon)|^2\, P_M(\tau, \epsilon)\, \mathrm{d}M \tag{6.12}$$

(a) Scenario A:
Zero tilt and constant eccentricity

(b) Scenario B:
Random tilt and constant eccentricity

(c) Scenario C:
Random tilt and random eccentricity
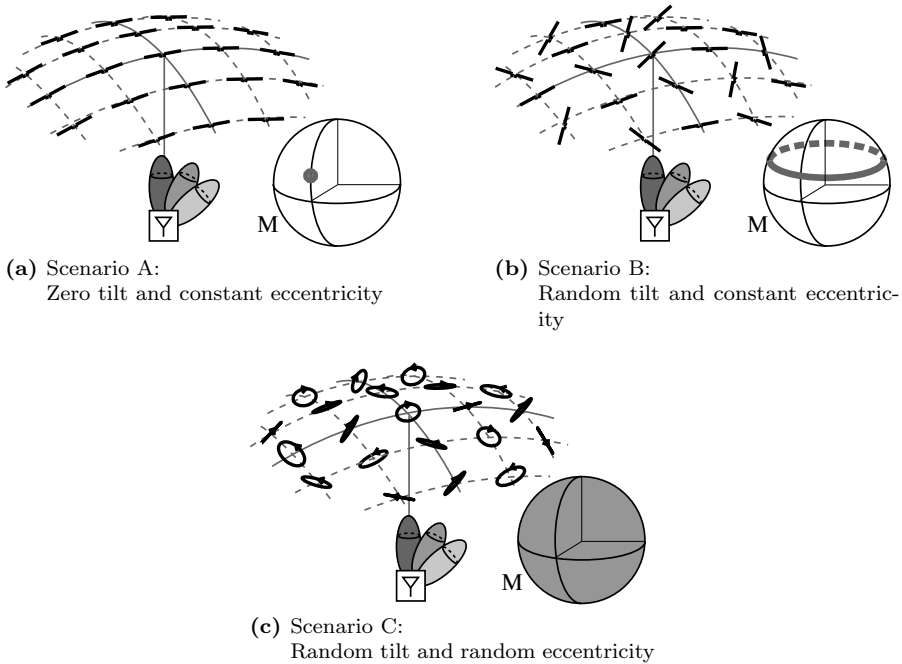
Fig. 6.3: Polarization statistics for the usual beam-switching scenarios and representation of the corresponding $P_M(\tau, \epsilon)$ over the Poincaré sphere.

The parameter η_p represents the average polarization efficiency for each direction. Equation (6.11) for the average maximum gain is simpler than the former in the sense that replaces a spatial-polarization double averaging by a single spatial averaging weighted by an additional factor representing the polarization efficiency.

The typical scenarios regarding the polarization statistics are depicted in Fig. 6.3. Scenario A describes situations where the polarization of the transmitting antenna is known and its orientation is preserved regardless of the direction. For instance, this is the case of a vertical dipole moving in the same horizontal plane where the RA lies or a terrestrial base-station tracking a non-geostationary satellite [141]. In these situations the RA polarization is aligned with the transmitting antenna polarization, which can be described as a single point over the Poincaré sphere. Scenario B includes similar situations where the polarization of the transmitting antenna is known but it can be randomly rotated. This rotation induces a random tilt angle over the incoming wave polarization which can be represented as a horizontal circumference over the Poincaré sphere. This could be the case of a mobile device receiving from a linearly polarized access point of a wireless personal area network (WPAN) [142]. Finally, scenario C encompasses situations which lack any *a priori* knowledge about the polarization of the transmitting antenna and therefore it is assumed to be equiprobable over the whole Poincaré sphere. This is the case of WPAN access point receiving from mobile devices with unknown polarizations.

In all these scenarios the weighting function $P_{\Omega \times M}$ is separable and the polarization statistics can be respectively described with the following expressions for scenarios a), b), c)

$$P_{M,a}(\tau, \epsilon) = \frac{1}{4 \cos 2\epsilon_0} \, \delta(\epsilon - \epsilon_0) \, \delta(\tau) \tag{6.13a}$$

$$P_{M,b}(\tau, \epsilon) = \frac{1}{4\pi \cos 2\epsilon_0} \, \delta(\epsilon - \epsilon_0) \tag{6.13b}$$

$$P_{M,c}(\tau, \epsilon) = \frac{1}{4\pi} \tag{6.13c}$$

Taking into account that the polarization mismatch between two antennas can be computed as follows

$$|\vec{e}_1 \cdot \vec{e}_2^*|^2 = \cos^2(\psi/2) = \tfrac{1}{2}(1 + \cos \psi) =$$
$$= \tfrac{1}{2}\left[1 + \sin 2\epsilon_1 \sin 2\epsilon_2 + \cos 2\epsilon_1 \cos 2\epsilon_2 \cos(2\,\Delta\tau)\right] \tag{6.14}$$

where ψ is the arc determined by their polarization states over the Poincaré sphere [143], the resulting average polarization efficiencies are

$$\eta_{p,a}(\theta, \phi) = \cos^2(\epsilon_{\mathrm{RA}} - \epsilon_0) \tag{6.15a}$$

$$\eta_{p,b}(\theta, \phi) = (1 + \sin 2\epsilon_{\mathrm{RA}} \, \sin 2\epsilon_0)/2 \tag{6.15b}$$

$$\eta_{p,c}(\theta, \phi) = 1/2 \tag{6.15c}$$

It can be observed that in the usual case where the eccentricity of the RA polarization (ϵ_{RA}) is not direction dependant, the polarization efficiency is constant. As expected, for linear and circular polarizations this efficiency is either 0, $\frac{1}{2}$ or 1 depending on the casuistic.

In these cases where the polarization efficiency is constant, the expression for the average maximum gain can be further simplified,

$$\overline{g}_{R,\max} = \eta_p \iint_\Omega \max_{i=1..N} G_R^i(\theta, \phi) \; P_\Omega(\theta, \phi) \, \mathrm{d}\Omega \tag{6.16}$$

As noted before, the validity of equation (6.16) requires that the RA and the scenario satisfy the three following conditions

c1) The polarization of all RA configurations $\{\hat{e}^i(\theta, \phi)\}$ has to be the same for each direction.

c2) The weighting function $P_{\Omega \times M}$ has to be separable into spatial and polarization components.

c3) The polarization efficiency $\eta_p(\theta, \phi)$ has to be constant for all directions.

The fulfillment of the previous conditions for every (θ, ϕ)-directions may be too restrictive in some situations. However, if they are satisfied for the main directions of radiation of the RA, equation (6.16) can still be used.

Since (c1) is naturally implied by the definition of pattern reconfigurability and since (c2) and (c3) are satisfied for usual scenarios, the average partial realized gain of the RA can be expressed as

$$\overline{g}_{R,\max} = \eta_p \, \overline{G}_{R,\max} \tag{6.17}$$

where $\overline{G}_{R,\max}$ is the average realized gain

$$\overline{G}_{R,\max} = \iint_{\Omega} \max_{i=1..N} G_R^i(\theta,\phi) \, P_{\Omega}(\theta,\phi) \, \mathrm{d}\Omega \tag{6.18}$$

6.2 FIGURE-OF-MERIT: EQUIVALENT NUMBER OF CON-FIGURATIONS

6.2.1 Figure-of-Merit definition and interpretation

The purpose of this section is to provide a figure-of-merit to quantify the reconfiguration capabilities of a RA. This figure-of-merit is based on the average gains discussed in the previous section. In order to obtain a general and objective figure-of-merit, all directions of arrival have to be considered to occur with the same probability

$$P_{\Omega}(\theta,\phi) = \tfrac{1}{4\pi} \tag{6.19}$$

This weighting function corresponds to the scenario with highest uncertainty regarding the direction of arrival of the incoming wave (P_{Ω} with maximum differential entropy). Following this consideration the proposed figure-of-merit of the RA consists in the average realized gain ($\overline{G}_{R,\max}$) for a uniformly distributed direction of arrival

$$N_{\mathrm{eq}} = \tfrac{1}{4\pi} \iint_{\Omega} \max_{i=1..N} G_R^i(\theta,\phi) \, \mathrm{d}\Omega \tag{6.20}$$

As will be subsequently evidenced, this figure-of-merit can be interpreted as an equivalent number of configurations and for this reason is denoted by N_{eq}.

For a non-reconfigurable antenna, the value of N_{eq} is less or equal than the unity, achieving the equality for perfectly-matched lossless antennas

$$N_{\mathrm{eq}} = \tfrac{1}{4\pi} \iint_{\Omega} G(\theta,\phi) \, \mathrm{d}\Omega \leq \tfrac{1}{4\pi} \iint_{\Omega} D(\theta,\phi) \, \mathrm{d}\Omega = 1 \tag{6.21}$$

On the other hand, for a reconfigurable antenna it can be observed that N_{eq} is bounded by the number of configurations (N)

$$
\begin{aligned}
N_{\mathrm{eq}} \;\;\leq\;\; & \tfrac{1}{4\pi} \iint_{\Omega} \max_{i=1..N} D^i(\theta,\phi) \, \mathrm{d}\Omega \\
\leq\;\; & \tfrac{1}{4\pi} \iint_{\Omega} \sum_{i=1..N} D^i(\theta,\phi) \, \mathrm{d}\Omega \;=\; N
\end{aligned}
\tag{6.22}
$$
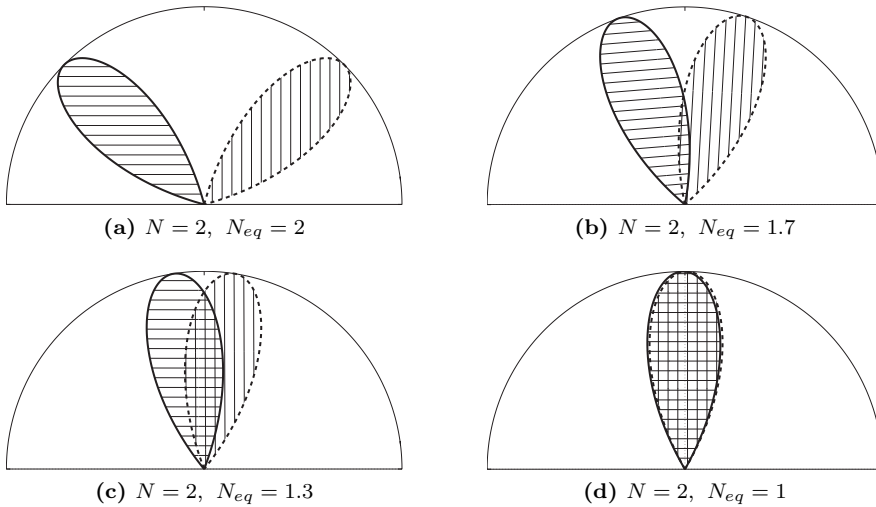
Fig. 6.4: Equivalent number of configurations of a RA with N=2 configurations depending
on the degree of overlapping between its radiation patterns. The radiation patterns
in this example are $\cos^n$-type with $n = 8$ and the angular distance between the
beams is 90°, 40°, 15° and 0° respectively.

Even more interesting than the previous inequality are the conditions that lead to
equality. This condition is that for every direction the maximum of all directivities
equals their addition, which basically means that the patterns of all configurations
must not overlap. As a consequence, the average realized gain can be interpreted
as the *equivalent number of configurations with non-overlapping radiation patterns*. It
should be noted that the number of configurations N of a RA is not a good measure of
its reconfiguration capabilities because it does not evaluate how different the produced
patterns are. On the other hand, as is shown in Fig. 6.4, this property is properly
captured by N_{eq}, which quantifies the degree of overlapping between the different
patterns.

Notice that N_{eq} evaluates global spherical distributions of radiation but is robust
respect to local variations. Therefore, capabilities not related with the gain/link bud-
get, such as null-creation, have to be evaluated with different figures-of-merit.

6.2.2   Figure-of-Merit upperbounds

In a similar way that the antenna bandwidth and gain are limited by the antenna
electric size, fundamental limitations also apply to the pattern reconfiguration capa-
bilities of a RA. Since the maximum gain of an antenna is limited by its size, so is the
equivalent number of configurations.

$$N_{\text{eq}} \leq \tfrac{1}{4\pi} \iint_{\Omega} G_{\text{max}} \, \mathrm{d}\Omega = G_{\text{max}} \tag{6.23}$$

Therefore, the equivalent number of configurations has the same upper bounds as

Tab. 6.1: Minimum size for a specific pattern reconfigurability.

$\overline{G}_R$	0 dB	5 dB	10 dB	15 dB	20 dB
N_{eq}	1	3.2	10	32	100
d	$< \lambda$	$< \lambda$	$\approx 1\lambda$	1.5λ	3λ

(a) $N_{eq} = 6$ **(b)** $N_{eq} = 12$ **(c)** $N_{eq} = 34$
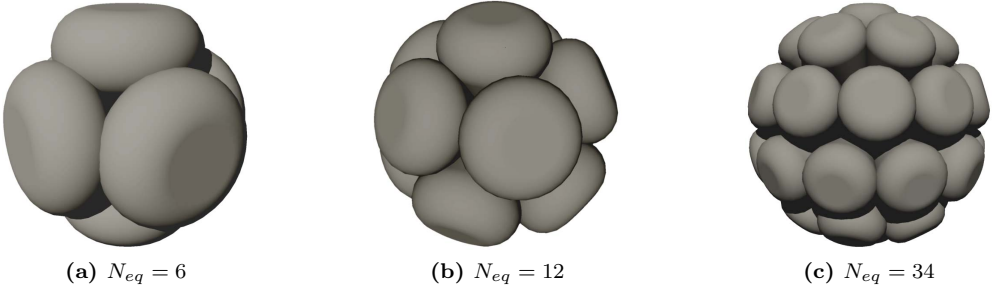
Fig. 6.5: Conceptual representation of the multiple radiation patterns of reconfigurable antennas with different equivalent number of configurations.

the antenna gain [105]

$$N_{\text{eq}} \leq N_{\text{sph}}^2 + 2N_{\text{sph}} \tag{6.24}$$

where N_{sph} is the number of spherical modes in the expansion of the antenna patterns. For small and large antennas the previous expression becomes

$$N_{\text{eq}} \leq 3 \qquad \text{(small antennas)} \tag{6.25a}$$

$$N_{\text{eq}} \leq (\pi d/\lambda)^2 + 2\pi d/\lambda \qquad \text{(large antennas)} \tag{6.25b}$$

where d is the diameter of the RA.

Table 6.1 provides the minimum required size for some representative values of the average realized gain.

The size dependance of the pattern reconfigurability of an antenna admits a clear intuitive interpretation. When the number of equivalent configurations is increased, their corresponding patterns have to be more closely packed over the sphere, as observed in Fig. 6.5. Therefore the beamwidth of each individual pattern has to be narrower and accordingly, the antenna will require a larger size.

The upper bounds in (6.25) can be theoretically reached respectively by a Huygens source and a uniformly illuminated circular aperture with full rotation capabilities respectively. However the implementation of RAs covering the complete sphere of incoming directions poses severe practical difficulties and the equivalent number of configurations for usual RAs is well below the theoretical upper bound. This is the case of one-dimensional pattern reconfigurability where the antenna beam is tilted in only one direction. In this case, tighter upper bounds can be obtained for large antennas

$$\Delta\theta_{\text{eq}} \simeq \Omega_{\text{eq}}^{1/2} = \frac{2\lambda}{\sqrt{\pi}d} \tag{6.26}$$
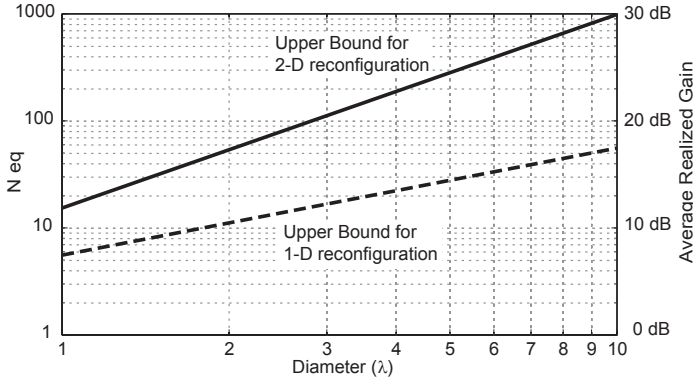
Fig. 6.6: Upper bound for the equivalent number of configurations of a pattern reconfigurable antenna.

$$N_{\text{eq}} \leq \frac{1}{4\pi} \int_0^{2\pi} \int_{-\Delta\theta_{\text{eq}}/2}^{\Delta\theta_{\text{eq}}/2} \left(\frac{\pi d}{\lambda}\right)^2 \mathrm{d}\theta \, \mathrm{d}\phi \simeq \pi^{3/2}\frac{d}{\lambda} \tag{6.27}$$

where $\Delta\theta_{\text{eq}}$ is the antenna minimum beamwidth and Ω_{eq} is the beam solid angle. It can be observed that for 1D beam-switching, the equivalent number of configurations increases linearly with the antenna diameter instead of quadratically. This upper bound can be reached by a uniform aperture with 1D-rotation capabilities. The maximum equivalent number of configurations as a function of the antenna size is represented in Fig. 6.6 for 1D and 2D pattern reconfigurable antennas.

6.2.3 Equivalent number of configurations of typical reconfigurable antenna architectures

In this section the equivalent number of configurations is computed for some specific antenna designs following different pattern reconfiguration techniques. The purpose of this comparison is not to provide an exhaustive assessment of pattern reconfigurable antennas, but to show that the proposed figure-of-merit N_{eq} properly quantifies pattern reconfigurability for the main RA architectures.

The different reconfigurable antennas analyzed are depicted in Fig. 6.7 and their equivalent number of configurations is represented in Fig. 6.8. The value of N_{eq} has been computed applying its definition in (6.20) considering the simulated radiation patterns of each antenna design using the available data in each reference.

The first considered case is a multi-antenna system with two printed Yagi antennas facing opposite directions, fed through a single-pole double-throw (SPDT) switch [61]. Since the Yagi antennas have directive patterns with low back-radiation, the two patterns present almost no overlapping and the equivalent number of configurations is 1.74, which is almost equal to the number of configurations.

The next RA design is a movable Vee antenna with mechanically-actuated arms that enable the rotation of its radiation pattern [49]. The rotation angle ranges from −45º to 45º and the E-plane beamwidth is 30º, therefore it is expected a N_{eq} close

(a) Antenna switching (from ref. [61])

(b) Rotatable antenna (from ref. [49])

(c) Switched parasitics (from ref. [75])

(d) Movable parasitics (from ref. [144])

(e) Pixel antenna (from ref. [145])

(f) Phased array
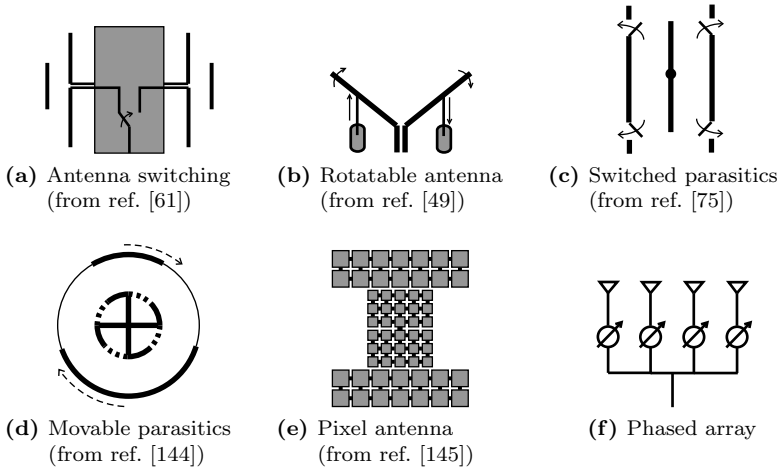
Fig. 6.7: Different pattern reconfigurable antennas considered for comparison according to their equivalent number of configurations.
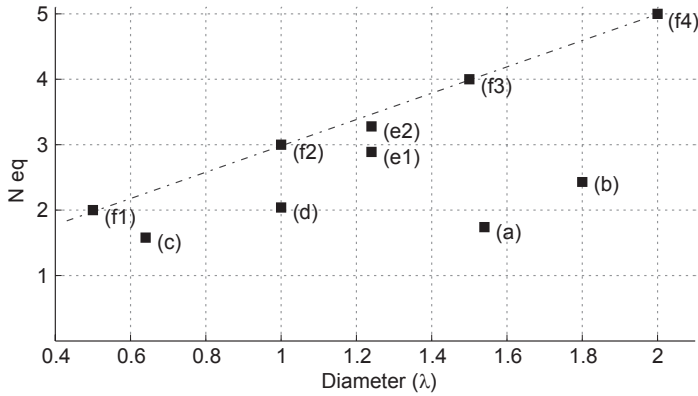
Fig. 6.8: Equivalent number of configurations of different pattern reconfigurable antennas.
(a) Switched antenna (ref. [61])
(b) Rotatable antenna (ref. [49])
(c) Antenna with switched parasitics (ref. [75])
(d) Antenna with movable parasitics (ref. [144])
(e) Pixel antenna with 8 and 16 beams (ref. [145])
(f) Phased-array with 2, 3, 4, 5 antennas and $\lambda/2$ spacing.
(g) Phased-array with 3, 4, 5, 6, 7, 8 antennas and $\lambda/4$ spacing.

to three. The simulated equivalent number of configurations is 2.41, which is smaller than the expected value because of the additional pattern overlapping introduced by the high side-lobes.

The equivalent number of configurations has been computed also for a parasitic array composed of switched parasitics with tunable reflector/director behavior [75].

The antenna has three configurations and the equivalent number of configurations is 1.58. The reason of this low value is the large beamwidth of the antenna patterns which produce a strong overlapping between them. In fact, its low N_{eq} is justified by the small dimensions of the antenna.

A similar situation occurs with other parasitic-based design composed of a circular Yagi structure with liquid metal parasitics [144]. The beamwidth of this antenna is also wide and the configurations present high overlapping, however since the pattern can be rotated over 360°, the equivalent number of configurations increases up to 2.04.

One of the antenna architectures with highest pattern reconfiguration capabilities are pixel apertures, which are composed of small metallic patches interconnected by switches. The considered antenna is a multi-size pixel dipole [145] synthesizing 8 or 16 beams over a 360° range, which leads to values of $N_{eq} = 2.89$ and $N_{eq} = 3.28$ respectively. As expected, the equivalent number of configurations is higher than in the previous designs, which is consistent with the higher complexity of the structure.

A final and particularly interesting case is the phased array with half-wavelength spaced isotropic elements and uniform feeding. For this antenna array the maximum gain achieved in each direction is equal to the number of array elements regardless of the direction considered. Therefore, the equivalent number of configurations of the phased array is equal to its number of elements. Minor degradations below 5% are observed when isotropic elements are replaced by realistic antennas. Since pixel designs are the only ones that approach the previous values, the phased array can serve as a realistic upper-bound for the equivalent number of configurations of practical RA designs. As a final comment, it should be noticed that the half-wavelength spaced array introduces grating lobes for end-fire configurations. Therefore, the array performance can be slightly improved by reducing the array spacing to a quarter-wavelength. In this case, the equivalent number of configurations increases in 0.5 and can not be further improved by additional spacing reductions.

6.3 PERFORMANCE EVALUATION FOR SUB-OPTIMAL RECONFIGURATION

As the number of configurations increases, the selection of the optimal configuration at each time constitutes a much challenging problem. The exhaustive testing of all configurations leads to unpractical training times. The common approach in this case uses a heuristic reconfiguration algorithm which operates much faster at the expense of selecting suboptimal configurations. The typical algorithms used in antenna reconfiguration were described in section 3.2.3 and include random walk, genetic algorithms and particle swarm optimization among others. The evaluation of the antenna performance can not be done in this case using the figure-of-merit presented in the previous section. In fact, the final antenna performance in this case is determined by two factors: the antenna pattern diversity and the performance of the reconfiguration algorithm. In this section we derive a useful formulation and figure-of-merit to evaluate the performance of reconfigurable antennas with a large number of configurations using a sub-optimal configuration selection. In particular, this is the usual case for most pixel antenna designs.

6.3.1 Formulation for the sub-optimal selection of configurations

In this formulation the same scenario described in the previous section (Fig. 6.1) is considered. The main difference between this case and the previous is the sub-optimal selection of configurations due to the large size of the configuration space. As a result, the antenna performance can be evaluated by replacing the maximum gain in (6.16) by the antenna gain provided by configuration selected by the optimization algorithm $(i_{\text{opt}}(\theta, \phi))$

$$\overline{G} = \iint_{\Omega} \left[\max_{i=1..N} G^i(\theta, \phi) \right] \; P_{\Omega}(\theta, \phi) \, \mathrm{d}\Omega \qquad \text{Optimal selection} \qquad (6.28a)$$

$$\overline{G} = \iint_{\Omega} G^{i_{\text{opt}}(\theta, \phi)}(\theta, \phi) \; P_{\Omega}(\theta, \phi) \, \mathrm{d}\Omega \qquad \text{Sub-optimal selection} \qquad (6.28b)$$

In order to characterize $G^{i_{\text{opt}}}(\theta, \phi)$ this formulations follows an statistical approach. Due to the very large number of configurations, the gain $G^i(\theta, \phi)$ for a fixed angular direction and a variable configuration can be modeled as a continuous random variable.

Let μ_G and σ_G be the realized gain average and standard deviation over all possible configurations for each angular direction

$$\mu_G(\theta, \phi) \;\; = \;\; \tfrac{1}{N} \sum_{i=1}^{N} G^i(\theta, \phi) \qquad (6.29)$$

$$\sigma_G(\theta, \phi) \;\; = \;\; \left[\tfrac{1}{N} \sum_{i=1}^{N} \left(G^i(\theta, \phi) - \mu_G(\theta, \phi) \right)^2 \right]^{1/2} \qquad (6.30)$$

Although the values of $\mu_G(\theta, \phi)$ and $\sigma_G(\theta, \phi)$ are direction-dependant, it can be assumed that the probability distribution of the following normalized gain

$$\left\{ \frac{G^i - \mu_G(\theta, \phi)}{\sigma_G(\theta, \phi)} \right\}_i \qquad (6.31)$$

is identical for all the different directions (θ, ϕ). This assumption will be validated in section 6.3.3 using the experimental data obtained from the pixel antenna prototypes presented in chapter 5. This assumption basically means that the antenna possible gains in each direction are identically distributed random variables except linear transformations. Therefore, given a certain optimization algorithm it is expected that the gain of optimized configuration in each direction $(G^{i_{opt}(\theta, \phi)})$ is the same for all directions after performing the normalization in (6.31).

$$\frac{G^{i_{opt}(\theta, \phi)} - \mu_G(\theta, \phi)}{\sigma_G(\theta, \phi)} = k_\sigma \qquad (6.32)$$

The parameter k_σ is a descriptor of the performance of the optimization algorithm used and does not depend on the angular direction (θ, ϕ).

Therefore, the expected gain of the optimized configuration in each direction can be written as follows

$$G^{i_{opt}(\theta,\phi)}(\theta,\phi) = \mu_G(\theta,\phi) + k_\sigma \sigma_G(\theta,\phi) \tag{6.33}$$

The performance of the reconfigurable antenna for the case of suboptimal selection of configurations results from equations (6.28b) and (6.33)

$$
\begin{aligned}
\overline{G} &= \iint_\Omega G^{i_{opt}(\theta,\phi)}(\theta,\phi) \ P_\Omega(\theta,\phi) \ \mathrm{d}\Omega \\
&= \iint_\Omega \left[\mu_G(\theta,\phi) + k_\sigma \, \sigma_G(\theta,\phi) \right] \ P_\Omega(\theta,\phi) \, \mathrm{d}\Omega
\end{aligned}
\tag{6.34}
$$

6.3.2   Figure-of-merit definitions and interpretation

Identically to the optimal selection case, in order to obtain a general and objective figure-of-merit, all directions of arrival have to be considered to occur with the same probability. Therefore the FoM is obtained by using $P_\Omega(\theta,\phi) = \frac{1}{4\pi}$ in equation (6.34)

$$\overline{G} = \frac{1}{4\pi} \iint_\Omega \left[\mu_G(\theta,\phi) + k_\sigma \, \sigma_G(\theta,\phi) \right] \ \mathrm{d}\Omega \tag{6.35}$$

The previous equation can be simplified taking into account that

$$\frac{1}{4\pi} \iint_\Omega \mu_G(\theta,\phi) \ \mathrm{d}\Omega \ = \ \frac{1}{4\pi} \iint_\Omega \frac{1}{N} \sum_{i=1}^{N} G^i(\theta,\phi) \ \mathrm{d}\Omega \ = \tag{6.36}$$

$$= \ \frac{1}{N} \sum_{i=1}^{N} \frac{1}{4\pi} \iint_\Omega G^i(\theta,\phi) \ \mathrm{d}\Omega \ = \ \overline{\mu}_G \tag{6.37}$$

where $\overline{\mu}_G$ is equal to 1 in the case of lossless perfectly matched antennas. Otherwise $\overline{\mu}_G$ is basically the average radiation efficiency (considering radiation losses and impedance mismatch).

Therefore, the average gain provided by the antenna can be simplified as

$$\overline{G} \ = \ \overline{\mu}_G + k_\sigma \overline{\sigma}_G \ = \ \underbrace{1}_{\substack{\text{lossless} \\ \text{well-matched}}} \ + \ \underbrace{k_\sigma}_{\substack{\text{optimization} \\ \text{algorithm}}} \ \underbrace{\overline{\sigma}_G}_{\substack{\text{pattern re-} \\ \text{configuration}}} \tag{6.38}$$

where

$$\overline{\sigma}_G = \frac{1}{4\pi} \iint_\Omega \sigma_G(\theta,\phi) \ \mathrm{d}\Omega \tag{6.39}$$

This result splits the performance of the reconfigurable antenna in two factors: $\overline{\sigma}_G$ and k_σ. The first depends only on the reconfigurable antenna and evaluates how different are the generated patterns, while the second measures the performance of the optimization algorithm. This formulation is specially elegant because it clearly reflects that the overall performance of the reconfigurable antenna depends on one hand on

(a) Pixel layer d=3mm

(b) Pixel layer d=8mm
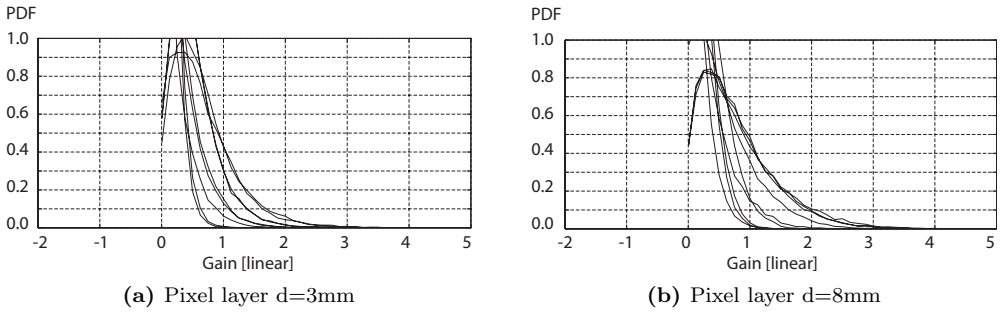
Fig. 6.9: Probability density function corresponding to the measured realized gain of pixel layer antenna. The frequency of operation is $2.7\,\mathrm{GHz}$ and the curves correspond to the following angular directions $\phi = \{0^{\mathrm{o}}, 90^{\mathrm{o}}, 180^{\mathrm{o}}, 270^{\mathrm{o}}\}, \ \ \theta = \{0^{\mathrm{o}}, 30^{\mathrm{o}}, 60^{\mathrm{o}}\}$.

the antenna pattern reconfigurability ($\overline{\sigma}_G$) and on the other hand on the optimization algorithm performance (k_σ).

In fact, equation (6.39) defines two figures-of-merit. k_σ is a figure-of-merit for the optimization algorithm and quantifies the capability of the algorithm to detect high-gain configurations. $\overline{\sigma}_G$ is the figure-of-merit for the pattern reconfigurability of real-time optimized antennas. From a intuitive perspective, this FoM is clearly a measure of pattern diversity. $\overline{\sigma}_G$ is basically an averaging over the 4π solid angle of the gain standard deviation. A high standard deviation of the gain implies that the antenna configurations provide very different gains and this only occurs when the radiation patterns corresponding to these configurations are very different from each other.

6.3.3   Figure-of-merit for the optimization algorithm (k_σ)

The value of the optimization algorithm figure-of-merit (k_σ) depends on two factors, the first is the optimization algorithms itself and the second is the statistics of the antenna normalized-gain defined by equation (6.31). In this section the statistics of the normalized-gain of pixel antennas are analyzed and the value of k_σ is evaluated for the random walk optimization algorithm.

The only additional assumption made in the formulation for sub-optimal reconfiguration, besides the conditions listed in section 6.1.2, is that the statistics of the normalized gain given by equation (6.31) is not directional-dependant. To validate this assumption the statistics of the antenna gain for different angular directions has been analyzed for different pixel antennas. In Fig. 6.9 it is represented the probability density function of the antenna gain (without normalization) corresponding to parasitic pixel layer antenna described in section 5.2. As expected the density functions corresponding to different angular directions have a different mean and standard deviation values. Actually, what occurs is that a high mean indicates directions with strong radiation, while a high standard deviation indicates directions with high reconfigurability.

(a) Pixel layer d=3mm

(b) Pixel layer d=8mm
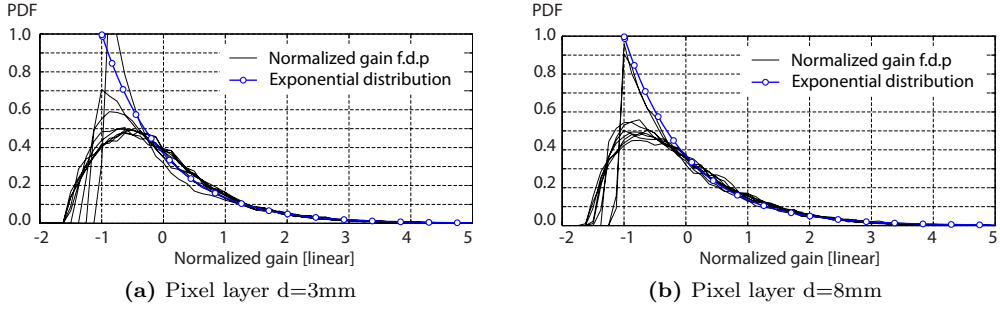
Fig. 6.10: Probability density function corresponding to the normalized measured gain $((G - \mu_G)/\sigma_G)$ of pixel layer antenna. The frequency of operation is 2.7 GHz and the curves correspond to the following angular directions: $\phi = \{0^\circ, 90^\circ, 180^\circ, 270^\circ\}$, $\theta = \{0^\circ, 30^\circ, 60^\circ\}$.

(a) Multi-size monopole $f = 2$ GHz

(b) Multi-size monopole $f = 3$ GHz
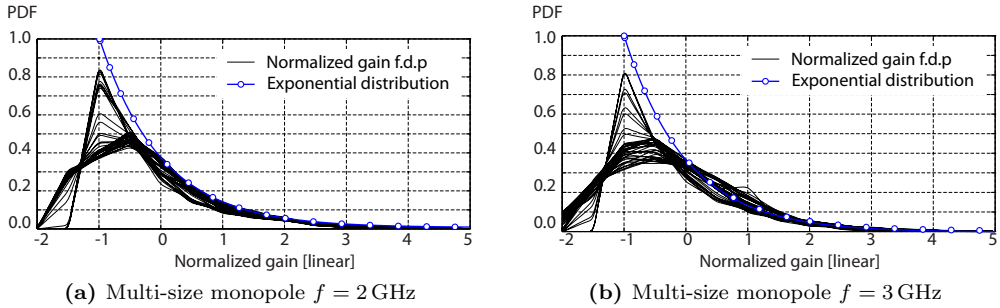
Fig. 6.11: Probability density function corresponding to the normalized measured gain $((G - \mu_G)/\sigma_G)$ of multi-size pixel antenna. The curves correspond to the following angular directions: $\phi = 0^\circ$, $\theta = \{-90^\circ, -85^\circ, -80^\circ, \ldots 90^\circ\}$.

The same probability density functions are represented in Fig. 6.10 after performing the gain normalization defined by equation (6.31). In this case, it is clearly observed that the right tails of these curves are almost overlapping. Since the optimization algorithm maximizes the antenna gain, it operates over the right tail of these density functions. Therefore, these results validate the original assumptions and allow to conclude that the value k_σ is not directional-dependant. More evidence that k_σ is not directional-dependant is provided in Fig. 6.11, where it is again observed the overlapping between the right tails of the normalized gain, this time for the multi-size pixel monopole described in section 5.2.

An additional important observation is that not only the right tails of the density functions is the same for all angular directions, but also for all these pixel antennas their right tails are exponentially-shaped. In Fig. 6.10 and Fig. 6.11 it is also represented the density function of an exponential distribution with zero-mean and standard deviation equal to one. It is clearly observed that the exponential distribution is a very accurate
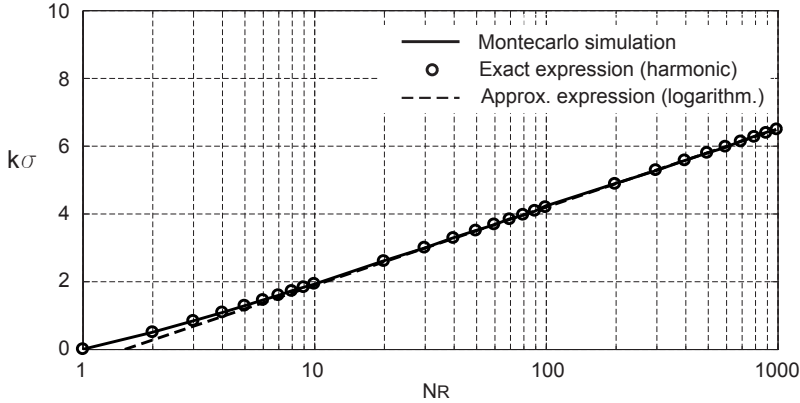
Fig. 6.12: Figure-of-merit of the Random-Walk optimization algorithm applied to an exponential distribution computed using Montecarlo simulation, exact and approximate analytical expressions.

approximation of the normalized-gain density functions. This is an important finding because the statistical distribution of the normalized-gain affects the performance of the optimization algorithm.

Having determined the statistical distribution of the normalized gain for pixel, we now evaluate the performance of the Random Walk (RW) optimization algorithm to provide some realistic values of k_σ. Let N_R be the population explored by the RW algorithm during the optimization of the antenna configuration. It is well-known that as a result of the memory-less property of the exponential distribution, the random variable corresponding to the maximum of N_R independent identically distributed exponential distributions is equal to the addition of N_R exponential distributions with rates equal to $1, 2, \ldots, N_R$. Therefore the value of k_σ is equal to the mean of the previous addition of exponential distribution minus one. Since the mean value of an exponential distribution is the inverse of its rate, k_σ takes the value of the harmonic numbers

$$k_\sigma = \sum_{n=2}^{N_R} \frac{1}{n} \tag{6.40}$$

The harmonic numbers have been deeply studied in analysis and number theory and they have been demonstrated to have a logarithmic grow

$$k_\sigma \approx \ln(N_R) - \gamma - 1 \tag{6.41}$$

where $\gamma = 0.577\ldots$ is the Euler-Mascheroni constant.

In Fig. 6.12 it is represented the figure-of-merit of the Random Walk algorithm computed using different methods. It can be observed that the Montecarlo simulations and the exact analytical expression agree perfectly well. The approximate logarithmic equation is an excellent approximation even for very low values of N_R.

The value of k_σ for different optimization algorithms such as genetic algorithm (GA) or particle swarm optimization (PSO), can also be computed. However, unlike

the random walk optimization, the performance of these algorithms depends on the particular structure of the configurations space. For this reason the value of k_σ will depend on the specific antenna being optimized. In this case, k_σ is still an excellent figure-of-merit of the optimization algorithm and measures the performance of the optimization algorithm for the reconfigurable antenna being optimized. This figure-of-merit would be useful to determine which are best optimization algorithms for each reconfigurable antenna architecture.

6.3.4   Figure-of-merit for pattern reconfigurability ($\overline{\sigma}_G$)

The performance of a dynamically optimized antenna is expressed by equation (6.38) as the combination of the performance of the reconfiguration algorithm (k_σ) and the antenna reconfigurability ($\overline{\sigma}_G$). In this section we analyze the properties of the figure-of-merit for pattern reconfigurability ($\overline{\sigma}_G$). This figure-of-merit is defined by equation (6.39) as the normalized-gain standard deviation averaged over the 4π solid angle

$$\overline{\sigma}_G = \frac{1}{4\pi} \iint_\Omega \sigma_G(\theta, \phi)\, \mathrm{d}\Omega$$

As was previously mentioned, a high standard deviation of the normalized-gain is clearly linked to a high variability of the antenna radiation pattern, and for this reason it captures the intuitive notion of pattern reconfigurability. It is important to study which is the maximum pattern reconfigurability achievable by a reconfigurable antenna and under which circumstances this maximum is achieved.

The first step to derive an upper-bound for $\overline{\sigma}_G$ consists on computing explicitly the value of $\sigma_G(\theta, \phi)$ depending on the radiation pattern G^i of each configuration

$$
\begin{aligned}
\sigma_G^2 &= \frac{1}{N} \sum_{i=1}^{N} \left[\frac{N-1}{N} G_i - \sum_{j \neq i} \frac{1}{N}(G^j) \right]^2 \\
&= \frac{1}{N^3} \sum_{i=1}^{N} \left[(N-1)^2 G_i^2 + \sum_{j \neq i} G_j^2 - 2(N-1)G_i \sum_{j \neq i} G_j + \sum_{j \neq i} \sum_{\substack{k \neq i \\ k \neq j}} G_j G_k \right] \\
&= \frac{1}{N^3} \left[(N-1)^2 \sum_{i=1}^{N} G_i^2 + (N-1) \sum_{i=1}^{N} G_i^2 - 2(N-1) \sum_{\substack{i,j \\ j \neq i}} G_i G_j + (N-2) \sum_{\substack{i,j \\ j \neq i}} G_i G_j \right] \\
&= \frac{N-1}{N^2} \left[\sum_{i=1}^{N} G_i^2 - \frac{1}{N-1} \sum_{\substack{i,j \\ j \neq i}} G_i G_j \right]
\end{aligned}
\tag{6.42}
$$

The previous expression makes easier to find an upperbound for σ_G

$$\sigma_G^2 \leq \frac{N-1}{N^2} \left[\sum_{i=1}^{N} G_i^2 + 2 \sum_{\substack{i,j \\ j \neq i}} G_i G_j \right] = \frac{N-1}{N^2} \left[\sum_{i=1}^{N} G_i \right]^2 \tag{6.43}$$

As a result,

$$\sigma_G \leq \frac{\sqrt{N-1}}{N} \sum_{i=1}^{N} G^i \tag{6.44}$$

and

$$\overline{\sigma}_G \ \leq \ \overline{\mu}_G \sqrt{N-1} \ \leq \ \sqrt{N-1} \tag{6.45}$$

$$\overline{G} \leq 1 + k_\sigma \sqrt{N-1} \tag{6.46}$$

This is an interesting result because the maximum growth of the average gain with the number of configurations is $O(\sqrt{N})$. Notice that this value is much lower than the average gain achieved under optimal reconfiguration which is equal to $O(N)$ 6.22. This phenomenon has a clear intuitive interpretation: given a certain optimization algorithm with limited time and computational resources, the selection of the optimal configuration becomes harder as the number of configurations increases. As a result, the antenna can not exploit all its pattern reconfiguration capabilities due to the limitations imposed by the suboptimal optimization algorithm.

We can also study which are conditions to achieve maximum pattern reconfigurability. By comparing equations (6.42) and (6.43) it is clear that maximum reconfigurability is obtain when the cross-products $G_i G_j$ are equal to zero, that is when the radiation patterns present no overlapping. Notice that even though the average gain obtained by optimal and sub-optimal reconfiguration is different, the conditions to achieve maximum reconfigurability remains the same: the radiation patterns of different configuration present no overlapping. It is worth mentioning that equations (6.42) and (6.43) clearly quantify the how much pattern diversity is lost due to the pattern overlapping between the different configurations. This loss of pattern reconfigurability is quantified by the two-by-two products of the different radiation patterns.

From a practical perspective it must be mentioned that in the case of antennas with a large number of configurations the evaluation of σ_G is much faster that evaluation of N_{eq}. While the latter requires an exhaustive exploration of all the configurations, the former can be easily estimated by exploring a smaller sample of configurations. The estimation of the gain standard deviation can be performed using the typical estimator of the standard deviation ($\sigma_{G,s}$) applied over a reduced sample (N_s)

$$\sigma_{G,s} = \sqrt{\frac{1}{N_s} \sum_{i=1}^{N_s} (G^i - \mu_{G,s})^2} \tag{6.47}$$

where

$$\mu_{G,s} = \frac{1}{N_s} \sum_{i=1}^{N_s} G^i \tag{6.48}$$

The statistical distribution of the sample standard deviation estimator has been extensively studied [146], and the standard deviation of this estimation is given by

$$\text{stdev}(\sigma_{G,s}) = \sigma_G \sqrt{1 - \frac{1}{N_S} - \frac{2\,\Gamma(N_S/2)}{N_S\,\Gamma((N_S-1)/2)}} \approx \frac{\sigma_G}{\sqrt{2N_S}} \tag{6.49}$$

Therefore, a relative error of 5% can be obtained by estimating $\sigma_{G,s}$ using a random sample of 200 configurations. However, to obtain a relative error of 1% the number of configurations to be measured is 5000.

CONCLUSIONS AND DISCUSSION

7.1 CONCLUSIONS

Pixel antennas are one of the most promising antenna architectures for the next generation of reconfigurable antennas where compacity, multi-functionality and multi-parameter reconfiguration are the main requirements. Pixel antennas provide a new level of reconfigurability thanks to the huge flexibility of their switched pixel surface, which provides simultaneously tunability of impedance and radiation parameters covering wide frequency ranges, steering the beam over large angular ranges and switching between multiple polarizations.

Despite the high reconfiguration capabilities of pixel antennas, their development has not yet achieved the maturity level required for their implementation in current wireless communication systems. The main barrier is the huge complexity required by existing pixel antennas, which typically use more than one hundred RF-switches impacting severely the antenna efficiency and cost. The second barrier is the lack of performance figures to quantify the system level benefits of pixel and reconfigurable antennas over their non-reconfigurable counterparts.

This doctoral dissertation has focused on the previous aspects and has contributed to approach pixel antennas to commercial wireless applications. The contributions and the main conclusions of this work are listed hereafter.

It has been shown that the pixel antenna complexity can be significantly reduced by using **multiple sized pixels** instead of uniform pixel surfaces. It has been observed that the near-port pixel have a higher effect over the antenna impedance properties and for this reason a fine grid of small pixels is required. Instead, the pixel located far from the RF-port have a lower influence over the antenna impedance and a higher influence over the radiation properties, and as a result larger pixels can be used in this region leading to an important reduction in the number of required switches. Additionally, it has been observed that not all switches contribute equally to the antenna reconfigurability and it is convenient to replace those switches with a lower contribution with wires and gaps. Pixel antennas with a number of switches as low as twelve have been designed, fabricated and characterized following these ideas. Even using a number of switches one order of magnitude lower than that of common pixel an-

tennas, the multi-size pixel antenna provide high reconfigurability over frequency and radiation properties, covering a 1:6 frequency range with up to five different radiation pattern at each frequency.

A new conceptual architecture consisting on using the pixel surface as a **parasitic layer** has been proposed, which contrasts with the active/driven behavior of common designs. The parasitic nature of the pixel layer has important advantages advantages regarding the switch biasing, power handling requirements and integration possibilities. Additionally it allows to reuse existing non-reconfigurable antennas and provide externally reconfiguration capabilities by adding a parasitic pixel layer. A fully operational prototype based in microstrip technology incorporating a 6×6 pixel layer with 60 switches has been fabricated and characterized proving the simultaneous reconfiguration of its frequency of operation, radiation pattern and polarization. It has been observed that the distance between the active antenna and the pixel layer determines the balance between frequency and radiation reconfigurability. Short distances, below a twentieth of a wavelength, favor frequency reconfigurability, which achieves up to a 25% of tuning range preserving the original instantaneous bandwidth of the driven antenna. On the other hand, large distances favor radiation reconfigurability and the pixel layer is able to steer the radiation beam up to 30° in the E and H planes preserving the pattern integrity over the whole frequency range of operation. The polarization can switch between four different polarizations (horizontal, vertical, LHCP and RHCP) with polarization mismatch losses of only 0.5 dB for the circular polarizations and 1 dB for the transpolarized linear polarization.

For the first time the full multi-parameter reconfiguration capabilities of pixel antennas have been explored. While in the previous literature on pixel antennas only partial explorations of the antenna reconfigurability were presented, in this work the **full reconfigurability** achieved by the multi-size pixel antenna and the parasitic pixel layer antenna has been **characterized**. The maximum achievable reconfiguration ranges (frequency range, beam-steering angular range and polarization modes) as well as the linkage between the different parameter under reconfiguration have been studied. This new information is very useful for future works and from a design perspective it would allow to decide if a pixel antenna may suit certain specific system requirements.

Microfluidic technology has been proposed as a new technology for pixel antennas which would allow effectively create and remove liquid metal pixels rather than interconnecting them. This pixel activation capability would enable higher performance pixel antennas thanks to the avoidance of the switch loss together with the complete removal of disconnected pixels. Although a pixel prototype has not been fabricated, a microfluidic prototype based in a Yagi-Uda architecture has been designed and fabricated to validate the capabilities of liquid metal microfluidics in reconfigurable antennas. This prototype uses liquid metal parasitic actuated by a continuous-flow system based in a micropump, achieving beam-steering capabilities thanks to the variable position of the parasitics.

Finally, the performance of pixel and reconfigurable antennas in beam-steering applications has been analyzed. **Figures-of-merit** have been derived to quantify radiation pattern reconfigurability for two case: RA with a low number of configurations

operating under optimal reconfiguration and RA with a large number of configuration operating under dynamical sub-optimal reconfiguration. These two figures-of-merit are directly related to the antenna performance since they evaluate the average gain provided by the RA. The figure-of-merit under optimal reconfiguration can be interpreted as the number of non-overlapped radiation patterns that the RA can synthesize. The RA performance under dynamical sub-optimal reconfiguration depends on two independent factors, the reconfiguration algorithm performance and the variability of the antenna radiation patterns. These figures-of-merit are excellent tools to evaluate and compare reconfigurable antenna designs, pixel antennas and reconfiguration algorithms.

7.2   FUTURE WORK

The use of pixel surfaces can be extended to other electromagnetic structures such as RF-repeater and electromagnetic reflective surfaces to provide them with reconfiguration capabilities. This is the case of a reconfigurable iso-frequency repeater where a pixel surface can located between the receiving and transmitting antennas to provide a high-isolation for a tunable frequency of operation [CA1]. Also tunable reflective surfaces can be synthesized by using pixel surfaces which would provide them with the capability of adjusting the operating frequency, reflectivity and the polarization of the reflected wave.

Another future line is the design and fabrication of a pixel antenna using microfluidic technology. The work here presented paves the way for development of such a prototype, which would require additional research on electrowetting techniques to displace a liquid metal from a reservoir to the pixel surface as well as non-distortive biasing methods. It is expected that the reconfiguration capability of microfluidic pixel antennas overcomes that of switched pixel antennas, a fact that requires a corroboration by comparing simulations and measurements of microfluidic and switched pixel designs.

The figures-of-merit here presented can be used as a tool to evaluate and compare the performance of different reconfigurable antennas. This tool can be used to assess the influence of the pixel antenna geometry over the antenna reconfigurability. This would allow to determine optimal pixel size, gap size, overall dimensions and number of switches. This analysis can be performed in a time-efficient way by simulating the pixel antennas using the port-loading technique.

Finally, one of the most important continuations of this work is the study of the system level benefits derived from the use of pixel antennas in communication systems. This is important not only for pixel antennas, but also for reconfigurable antennas in general. Indeed, the definitive evidence to determine if the additional performance provided by pixel reconfigurable antennas overcomes their additional cost and complexity will be provided by system level tests exploring the improvement of the system capabilities in terms of coverage, data/error rates, power consumption, number of simultaneous users and reliability.

BIBLIOGRAPHY

[1] "IEEE standard definitions of terms for antennas," 1993, IEEE Std 145-1993.

[2] J. T. Bernhard, *Reconfigurable Antennas*, ser. Synthesis Lectures on Antennas. Morgan & Claypool Publishers, 2007.

[3] G. H. Huff and J. T. Bernhard, "Reconfigurable antennas," in *Modern Antenna Handbook*, C. A. Balanis, Ed. John Wiley & Sons, Inc., 2008, pp. 369–398.

[4] A. Goldsmith, "Apparatus for wave changing in radiosignaling," USA Patent 1 571 405, Feb., 1926.

[5] E. Werndl, "Antenna tunable in its length," USA Patent 2 278 601, Apr., 1942.

[6] L. Van Atta and S. Silver, "Contributions to the antenna field during World War II," *Proceedings of the IRE*, vol. 50, no. 5, pp. 692–697, 1962.

[7] W. Rotman and A. Maestri, "An electromechanically scannable trough waveguide array," in *IRE international convention record*, vol. 8. IEEE, 1960, pp. 67–83.

[8] J. Maloney, M. Kesler, L. Lust, L. Pringle, T. Fountain, P. Harms, and G. Smith, "Switched fragmented aperture antennas," in *Antennas and Propagation Society International Symposium, 2000. IEEE*, vol. 1, 2000, pp. 310–313 vol.1.

[9] L. Pringle *et al.*, "GTRI reconfigurable aperture design," in *Antennas and Propagation Society International Symposium, 2002. IEEE*, vol. 1, 2002, pp. 473–476 vol.1.

[10] Y. Erdemli, R. Gilbert, and J. Volakis, "A reconfigurable slot aperture design over a broad-band substrate/feed structure," *IEEE Trans. Antennas Propag.*, vol. 52, no. 11, pp. 2860 – 2870, nov. 2004.

[11] A. Grau, J. Romeu, L. Jofre, and F. De Flaviis, "A software defined MEMS-reconfigurable PIXEL-antenna for narrowband MIMO systems," in *Adaptive Hardware and Systems, 2008. AHS '08. NASA/ESA Conference on*, June 2008, pp. 141–146.

[12] L. Pringle *et al.*, "A reconfigurable aperture antenna based on switched links between electrically small metallic patches," *IEEE Trans. Antennas Propag.*, vol. 52, no. 6, pp. 1434–1445, June 2004.

[13] J. Ross, E. Rothwell, and S. Preschutti, "A complementary self-structuring antenna for use in a vehicle environment," in *Antennas and Propagation Society International Symposium, 2004. IEEE*, vol. 3, 20-25 2004, pp. 2321 – 2324 Vol.3.

[14] B. Perry, E. Rothwell, and L. Nagy, "Analysis of switch failures in a self-structuring antenna system," *IEEE Antennas Wireless Propag. Lett.*, vol. 4, pp. 68 – 70, 2005.

[15] L. Greetis, R. Ouedraogo, B. Greetis, and E. Rothwell, "A self-structuring patch antenna: Simulation and prototype," *IEEE Antennas Propag. Mag.*, vol. 52, no. 1, pp. 114 –123, feb. 2010.

[16] R. Mehmood and J. Wallace, "Diminishing returns with increasing complexity in reconfigurable aperture antennas," *IEEE Antennas Wireless Propag. Lett.*, vol. 9, pp. 299 –302, 2010.

[17] D. Linden, "A system for evolving antennas in-situ," in *Evolvable Hardware, 2001. Proceedings. The Third NASA/DoD Workshop on*, 2001, pp. 249 –255.

[18] S. Nikolaou, N. D. Kingsley, G. E. Ponchak, J. Papapolymerou, and M. M. Tentzeris, "UWB elliptical monopoles with a reconfigurable band notch using MEMS switches actuated without bias lines," *IEEE Trans. Antennas Propag.*, vol. 57, no. 8, pp. 2242–2251, 2009.

[19] A. van Bezooijen, M. A. de Jongh, C. Chanlo, L. Ruijs, F. van Straten, R. Mahmoudi, and A. van Roermund, "A GSM/EDGE/WCDMA adaptive series-LC matching network using RF-MEMS switches," *IEEE J. Solid-State Circuits*, vol. 43, no. 10, pp. 2259–2268, 2008.

[20] A. Grau and F. De Flaviis, "A distributed antenna tuning unit using a frequency reconfigurable pixel-antenna," in *Antennas and Propagation (EuCAP), 2010 Proceedings of the Fourth European Conference on*, april 2010, pp. 1 –5.

[21] I. Akyildiz, W. Lee, M. Vuran, and S. Mohanty, "Next generation/dynamic spectrum access/cognitive radio wireless networks: a survey," *Computer Networks*, vol. 50, no. 13, pp. 2127–2159, 2006.

[22] Y. Cai, Y. Guo, and T. Bird, "A frequency reconfigurable printed yagi-uda dipole antenna for cognitive radio applications," *IEEE Trans. Antennas Propag.*, vol. 60, no. 6, pp. 2905 –2912, june 2012.

[23] A. Alexiou and M. Haardt, "Smart antenna technologies for future wireless systems: trends and challenges," *Communications Magazine, IEEE*, vol. 42, no. 9, pp. 90–97, 2004.

[24] R. Mehmood and J. W. Wallace, "Interference suppression using parasitic reconfigurable aperture (recap) antennas," in *Proc. Int Antenna Technology (iWAT) Workshop*, 2011, pp. 82–85.

[25] B. A. Cetiner, H. Jafarkhani, J.-Y. Qian, H. J. Yoo, A. Grau, and F. De Flaviis, "Multifunctional reconfigurable MEMS integrated antennas for adaptive MIMO systems," *IEEE Commun. Mag.*, vol. 42, no. 12, pp. 62–70, 2004.

[26] F. Fazel, A. Grau, H. Jafarkhani, and F. Flaviis, "Space-time-state block coded mimo communication systems using reconfigurable antennas," *IEEE Trans. Wireless Commun.*, vol. 8, no. 12, pp. 6019 –6029, december 2009.

[27] D. Piazza, N. Kirsch, A. Forenza, R. Heath, and K. Dandekar, "Design and evaluation of a reconfigurable antenna array for MIMO systems," *IEEE Trans. Antennas Propag.*, vol. 56, no. 3, pp. 869–881, 2008.

[28] A. Maltsev, E. Perahia, R. Maslennikov, A. Sevastyanov, A. Lomayev, and A. Khoryaev, "Impact of polarization characteristics on 60-GHz indoor radio communication systems," *IEEE Antennas Wireless Propag. Lett.*, vol. 9, pp. 413–416, 2010.

[29] A. Grau, J. Romeu, M.-J. Lee, S. Blanch, L. Jofre, and F. De Flaviis, "A dual-linearly-polarized MEMS-reconfigurable antenna for narrowband MIMO communication systems," *IEEE Trans. Antennas Propag.*, vol. 58, no. 1, pp. 4–17, 2010.

[30] B. Cetiner, E. Akay, E. Sengul, and E. Ayanoglu, "A MIMO system with multifunctional reconfigurable antennas," *IEEE Antennas Wireless Propag. Lett.*, vol. 5, no. 1, pp. 463–466, Dec. 2006.

[31] J. Perruisseau-Carrier, "Versatile reconfiguration of radiation patterns, frequency and polarization: A discussion on the potential of controllable reflectarrays for software-defined and cognitive radio systems," in *RF Front-ends for Software Defined and Cognitive Radio Solutions (IMWS), 2010 IEEE International Microwave Workshop Series on*, feb. 2010, pp. 1 –4.

[32] E. Brown, "RF-MEMS switches for reconfigurable integrated circuits," *IEEE Trans. Microw. Theory Tech.*, vol. 46, no. 11, pp. 1868 –1880, nov 1998.

[33] G. Jin, D. Zhang, and R. Li, "Optically controlled reconfigurable antenna for cognitive radio applications," *Electronics Letters*, vol. 47, no. 17, pp. 948 –950, 18 2011.

[34] C. Panagamuwa, A. Chauraya, and J. Vardaxoglou, "Frequency and beam reconfigurable antenna using photoconducting switches," *IEEE Trans. Antennas Propag.*, vol. 54, no. 2, pp. 449 – 454, feb. 2006.

[35] C. Wu, T. Wang, A. Ren, and D. Michelson, "Implementation of reconfigurable patch antennas using reed switches," *IEEE Antennas Wireless Propag. Lett.*, vol. 10, pp. 1023 –1026, 2011.

[36] D. M. Pozar and V. Sanchez, "Magnetic tuning of a microstrip antenna on a ferrite substrate," *Electronics Letters*, vol. 24, no. 12, pp. 729–731, 1988.

[37] R. K. Mishra, S. S. Pattnaik, and N. Das, "Tuning of microstrip antenna on ferrite substrate," *IEEE Trans. Antennas Propag.*, vol. 41, no. 2, pp. 230–233, 1993.

[38] A. D. Brown, J. L. Volakis, L. C. Kempel, and Y. Botros, "Patch antennas on ferromagnetic substrates," *IEEE Trans. Antennas Propag.*, vol. 47, no. 1, pp. 26–32, 1999.

[39] A. Tagantsev, V. Sherman, K. Astafiev, J. Venkatesh, and N. Setter, "Ferroelectric materials for microwave tunable applications," *Journal of Electroceramics*, vol. 11, no. 1, pp. 5–66, 2003.

[40] Y. Yashchyshyn and J. Modelski, "Rigorous analysis and investigations of the scan antennas on a ferroelectric substrate," *IEEE Trans. Microw. Theory Tech.*, vol. 53, no. 2, pp. 427–438, 2005.

[41] N. Martin, P. Laurent, C. Person, P. Gelin, and F. Huret, "Patch antenna adjustable in frequency using liquid crystal," in *Proc. 33rd European Microwave Conf*, vol. 2, 2003, pp. 699–702.

[42] L. Liu and R. Langley, "Liquid crystal tunable microstrip patch antenna," *Electronics Letters*, vol. 44, no. 20, pp. 1179–1180, 2008.

[43] J. Huang and J. A. Encinar, *Reflectarray antennas.* John Wiley & Sons, Inc., 2008.

[44] A. Gaebler *et al.*, "Liquid crystal-reconfigurable antenna concepts for space applications at microwave and millimeter waves," *Int. J. Antennas and Propag.*, vol. 2009, 2009.

[45] W. Hu, R. Cahill, J. Encinar, R. Dickie, H. Gamble, V. Fusco, and N. Grant, "Design and measurement of reconfigurable millimeter wave reflectarray cells with nematic liquid crystal," *IEEE Trans. Antennas Propag.*, vol. 56, no. 10, pp. 3112–3117, 2008.

[46] N. Ehteshami and V. Sathi, "New optically controlled frequency-agile microstrip antenna," *J. Electron. Mater.*, pp. 1–6, 2012.

[47] F. Carrique, F. Arroyo, M. Jiménez, and A. Delgado, "Dielectric response of concentrated colloidal suspensions," *The Journal of chemical physics*, vol. 118, p. 1945, 2003.

[48] S. Long and G. Huff, "A fluidic loading mechanism for phase reconfigurable reflectarray elements," *IEEE Antennas Wireless Propag. Lett.*, vol. 10, pp. 876–879, 2011.

[49] J.-C. Chiao, Y. Fu, I. M. Chio, M. DeLisio, and L.-Y. Lin, "MEMS reconfigurable vee antenna," in *Proc. IEEE MTT-S Int. Microwave Symp. Digest*, vol. 4, 1999, pp. 1515–1518.

[50] K. Daheshpour *et al.*, "Pattern reconfigurable antenna based on moving v-shaped parasitic elements actuated by dielectric elastomer," *Electronics Letters*, vol. 46, no. 13, pp. 886–888, 2010.

[51] Y. Tawk, J. Costantine, K. Avery, and C. Christodoulou, "Implementation of a cognitive radio front-end using rotatable controlled reconfigurable antennas," *IEEE Trans. Antennas Propag.*, vol. 59, no. 5, pp. 1773 –1778, may 2011.

[52] R. Al-Dahleh, C. Shafai, and L. Shafai, "Frequency-agile microstrip patch antenna using a reconfigurable MEMS ground plane," *Microwave and Optical Technology Letters*, vol. 43, pp. 64–67, 2004.

[53] J.-C. Langer, J. Zou, C. Liu, and J. Bernhard, "Micromachined reconfigurable out-of-plane microstrip patch antenna using plastic deformation magnetic actuation," *IEEE Microw. Wireless Compon. Lett.*, vol. 13, no. 3, pp. 120–122, Mar 2003.

[54] J. M. Zendejas, J. P. Gianvittorio, Y. Rahmat-Samii, and J. W. Judy, "Magnetic MEMS reconfigurable frequency-selective surfaces," *J. Microelectromech. Syst.*, vol. 15, no. 3, pp. 613–623, 2006.

[55] Y. Kim, N.-G. Kim, J.-M. Kim, S. H. Lee, Y. Kwon, and Y.-K. Kim, "60-ghz full mems antenna platform mechanically driven by magnetic actuator," *IEEE Trans. Ind. Electron.*, vol. 58, no. 10, pp. 4830 –4836, oct. 2011.

[56] S. Cheng, Z. Wu, P. Hallbjorner, K. Hjort, and A. Rydberg, "Foldable and stretchable liquid metal planar inverted cone antenna," *IEEE Trans. Antennas Propag.*, vol. 57, no. 12, pp. 3765–3771, 2009.

[57] S. Cheng, A. Rydberg, K. Hjort, and Z. Wu, "Liquid metal stretchable unbalanced loop antenna," *Appl. Physics Lett.*, vol. 94, no. 14, p. 144103, 2009.

[58] H.-T. Kim, S. Jung, K. Kang, J.-H. Park, Y.-K. Kim, and Y. Kwon, "Low-loss analog and digital micromachined impedance tuners at the Ka-band," *IEEE Trans. Microw. Theory Tech.*, vol. 49, no. 12, pp. 2394–2400, 2001.

[59] J. Papapolymerou, K. L. Lange, C. L. Goldsmith, A. Malczewski, and J. Kleber, "Reconfigurable double-stub tuners using MEMS switches for intelligent rf front-ends," *IEEE Trans. Microw. Theory Tech.*, vol. 51, no. 1, pp. 271–278, 2003.

[60] T. Wu *et al.*, "Switchable quad-band antennas for cognitive radio base station applications," *IEEE Trans. Antennas Propag.*, vol. 58, no. 5, pp. 1468–1476, 2010.

[61] S. Cheng, P. Rantakari, R. Malmqvist, C. Samuelsson, T. Vaha-Heikkila, A. Rydberg, and J. Varis, "Switched beam antenna based on RF MEMS SPDT switch on quartz substrate," *IEEE Antennas Wireless Propag. Lett.*, vol. 8, pp. 383–386, 2009.

[62] B. A. Cetiner, L. Jofre, J. Qian, S. Liu, G. P. Li, and F. De Flaviis, "A compact broadband MEMS-integrated diversity system," *IEEE Trans. Veh. Technol.*, vol. 56, no. 2, pp. 436–444, 2007.

[63] Y.-F. Wu, C.-H. Wu, D.-Y. Lai, and F.-C. Chen, "A reconfigurable quadri-polarization diversity aperture-coupled patch antenna," *IEEE Trans. Antennas Propag.*, vol. 55, no. 3, pp. 1009–1012, 2007.

[64] R. Hansen, *Phased array antennas.* Wiley-Interscience, 2009, vol. 213.

[65] R. Mailloux, *Phased array antenna handbook.* Artech House Boston, 2005.

[66] D. Peroulis, K. Sarabandi, and L. Katehi, "Design of reconfigurable slot antennas," *IEEE Trans. Antennas Propag.*, vol. 53, no. 2, pp. 645 –654, feb. 2005.

[67] K. Van Caekenberghe and K. Sarabandi, "A 2-bit Ka-band RF MEMS frequency tunable slot antenna," *IEEE Antennas Wireless Propag. Lett.*, vol. 7, pp. 179–182, 2008.

[68] B. A. Cetiner, G. R. Crusats, L. Jofre, and N. Biyikli, "RF-MEMS integrated frequency reconfigurable annular slot antenna," *IEEE Trans. Antennas Propag.*, vol. 58, no. 3, pp. 626–632, 2010.

[69] N. Kingsley, D. E. Anagnostou, M. Tentzeris, and J. Papapolymerou, "RF MEMS sequentially reconfigurable sierpinski antenna on a flexible organic substrate with novel dc-biasing technique," *J. Microelectromech. Syst.*, vol. 16, no. 5, pp. 1185–1192, 2007.

[70] S. G. O'Keefe and S. P. Kingsley, "Tunability of liquid dielectric resonator antennas," *IEEE Antennas Wireless Propag. Lett.*, vol. 6, pp. 533–536, 2007.

[71] E. Erdil, K. Topalli, M. Unlu, O. Civi, and T. Akin, "Frequency tunable microstrip patch antenna using RF MEMS technology," *IEEE Trans. Antennas Propag.*, vol. 55, no. 4, pp. 1193–1196, April 2007.

[72] C. W. Jung, Y. J. Kim, Y. E. Kim, and F. De Flaviis, "Macro-micro frequency tuning antenna for reconfigurable wireless communication systems," *Electronics Letters*, vol. 43, no. 4, pp. 201–202, 2007.

[73] R. Vaughan, "Switched parasitic elements for antenna diversity," *IEEE Trans. Antennas Propag.*, vol. 47, no. 2, pp. 399–405, 1999.

[74] M. D. Migliore, D. Pinchera, and F. Schettino, "A simple and robust adaptive parasitic antenna," *IEEE Trans. Antennas Propag.*, vol. 53, no. 10, pp. 3262–3272, 2005.

[75] S. Zhang, G. Huff, J. Feng, and J. Bernhard, "A pattern reconfigurable microstrip parasitic array," *IEEE Trans. Antennas Propag.*, vol. 52, no. 10, pp. 2773–2776, Oct. 2004.

[76] X.-S. Yang, B.-Z. Wang, and W. Wu, "Pattern reconfigurable patch antenna with two orthogonal quasi-yagi arrays," in *Antennas and Propagation Society International Symposium, 2005 IEEE*, vol. 2B, July 2005, pp. 617–620 vol. 2B.

[77] M. Donelli, R. Azaro, L. Fimognari, and A. Massa, "A planar electronically reconfigurable Wi-Fi band antenna based on a parasitic microstrip structure," *IEEE Antennas Wireless Propag. Lett.*, vol. 6, pp. 623–626, 2007.

[78] L. Petit, L. Dussopt, and J.-M. Laheurte, "MEMS-switched parasitic-antenna array for radiation pattern diversity," *IEEE Trans. Antennas Propag.*, vol. 54, no. 9, pp. 2624–2631, 2006.

[79] R. Harrington, "Reactively controlled directive arrays," *IEEE Trans. Antennas Propag.*, vol. 26, no. 3, pp. 390–395, 1978.

[80] R. Mehmood and J. Wallace, "Mimo capacity enhancement using parasitic reconfigurable aperture antennas (recaps)," *IEEE Trans. Antennas Propag.*, vol. 60, no. 2, pp. 665–673, 2012.

[81] J. P. Gianvittorio and Y. Rahmat-Samii, "Reconfigurable patch antennas for steerable reflectarray applications," *IEEE Trans. Antennas Propag.*, vol. 54, no. 5, pp. 1388–1392, 2006.

[82] S. Hum, M. Okoniewski, and R. Davies, "Modeling and design of electronically tunable reflectarrays," *IEEE Trans. Antennas Propag.*, vol. 55, no. 8, pp. 2200 –2210, aug. 2007.

[83] S. Hum, M. Okoniewski, and R. Davies, "Realizing an electronically tunable reflectarray using varactor diode-tuned elements," *Microwave and Wireless Components Letters, IEEE*, vol. 15, no. 6, pp. 422 – 424, june 2005.

[84] J. Perruisseau-Carrier and A. K. Skrivervik, "Monolithic MEMS-based reflectarray cell digitally reconfigurable over a 360° phase range," *IEEE Antennas Wireless Propag. Lett.*, vol. 7, pp. 138–141, 2008.

[85] C.-C. Cheng, B. Lakshminarayanan, and A. Abbaspour-Tamijani, "A programmable lens-array antenna with monolithically integrated MEMS switches," *IEEE Trans. Microw. Theory Tech.*, vol. 57, no. 8, pp. 1874–1884, 2009.

[86] C. won Jung, M. jer Lee, G. Li, and F. De Flaviis, "Reconfigurable scan-beam single-arm spiral antenna integrated with RF-MEMS switches," *IEEE Trans. Antennas Propag.*, vol. 54, no. 2, pp. 455–463, Feb. 2006.

[87] S. Lim, C. Caloz, and T. Itoh, "Metamaterial-based electronically controlled transmission-line structure as a novel leaky-wave antenna with tunable radiation angle and beamwidth," *IEEE Trans. Microw. Theory Tech.*, vol. 52, no. 12, pp. 2678 – 2690, dec. 2004.

[88] D. Piazza, D. Michele, and K. Dandekar, "Two port reconfigurable crlh leaky wave antenna with improved impedance matching and beam tuning," in *Antennas and Propagation, 2009. EuCAP 2009. 3rd European Conference on*, march 2009, pp. 2046 –2049.

[89] R. N. Simons, D. Chun, and L. P. B. Katehi, "Polarization reconfigurable patch antenna using microelectromechanical systems (MEMS) actuators," in *Proc. IEEE Antennas and Propagation Society Int. Symp*, vol. 2, 2002, pp. 6–9.

[90] J. Balcells, Y. Damgaci, B. A. Cetiner, J. Romeu, and L. Jofre, "Polarization reconfigurable MEMS-CPW antenna for mm-wave applications," in *Proc. Fourth European Conf. Antennas and Propagation (EuCAP)*, 2010, pp. 1–5.

[91] X.-S. Yang, B.-Z. Wang, W. Wu, and S. Xiao, "Yagi patch antenna with dual-band and pattern reconfigurable characteristics," *IEEE Antennas Wireless Propag. Lett.*, vol. 6, pp. 168–171, 2007.

[92] S. Nikolaou *et al.*, "Pattern and frequency reconfigurable annular slot antenna using PIN diodes," *IEEE Trans. Antennas Propag.*, vol. 54, no. 2, pp. 439–448, 2006.

[93] J.-S. Row and C.-J. Shih, "Polarization-diversity ring slot antenna with frequency agility," *IEEE Trans. Antennas Propag.*, vol. 60, no. 8, pp. 3953 –3957, aug. 2012.

[94] G. H. Huff, J. Feng, S. Zhang, and J. T. Bernhard, "A novel radiation pattern and frequency reconfigurable single turn square spiral microstrip antenna," *IEEE Microw. Wireless Compon. Lett.*, vol. 13, no. 2, pp. 57–59, 2003.

[95] J. Perruisseau-Carrier, "Dual-polarized and polarization-flexible reflective cells with dynamic phase control," *IEEE Trans. Antennas Propag.*, vol. 58, no. 5, pp. 1494 –1502, may 2010.

[96] E. Carrasco, J. A. Encinar, and J. Perruisseau-Carrier, "Evaluation of a reflectarray with independent scanning of two linearly-polarized beams," in *Proc. 6th European Conf. Antennas and Propagation (EUCAP)*, 2012, pp. 2967–2970.

[97] J. Perruisseau-Carrier, "Optimal cell topology constraint for monolayer dual-polarized beamscanning reflectarrays," *IEEE Antennas Wireless Propag. Lett.*, vol. 11, pp. 434–437, 2012.

[98] E. Carrasco, J. A. Encinar, M. Barba, R. Vincenti, and R. Sorrentino, "Dual-polarization reflectarray elements for ku-band tx/rx portable terminal antenna," in *Proc. Fourth European Conf. Antennas and Propagation (EuCAP)*, 2010, pp. 1–5.

[99] C. Guclu, J. Perruisseau-Carrier, and O. Civi, "Proof of concept of a dual-band circularly-polarized RF MEMS beam-switching reflectarray," *IEEE Trans. Antennas Propag.*, vol. 60, no. 11, pp. 5451–5455, 2012.

[100] J. Maloney, M. Kesler, P. Harms, T. Fountain, and G. Smith, "The fragmented aperture antenna: Fdtd analysis and measurement," in *Millennium Conference on Antennas and Propagation (AP 2000)*, April 2000.

[101] J. Maloney, M. Kesler, P. Harms, and G. Smith, "Fragmented aperture antennas and broadband antenna ground planes," Nov. 27 2001, USA Patent 6,323,809.

[102] E. Brown, "On the gain of a reconfigurable-aperture antenna," *IEEE Trans. Antennas Propag.*, vol. 49, no. 10, pp. 1357 –1362, oct 2001.

[103] A. Grau and F. De Flaviis, "A multifunctional reconfigurable pixeled antenna using MEMS technology on printed circuit board," *IEEE Trans. Antennas Propag.*, vol. 59, no. 12, pp. 4413–4424, dec. 2011.

[104] R. Williams, *The geometrical foundation of natural structure: A source book of design.* Dover Publications, 1979.

[105] R. Harrington, "On the gain and beamwidth of directional antennas," *IRE Trans. Antennas Propag.*, vol. 6, no. 3, pp. 219 –225, july 1958.

[106] M. Yousefbeiki and J. Perruisseau-Carrier, "A practical technique for accurately modeling reconfigurable lumped components in commercial full-wave solvers," *IEEE Antennas Propag. Mag.*, vol. 54, no. 5, pp. 298–303, 2012.

[107] C. Coleman, E. Rothwell, and J. Ross, "Investigation of simulated annealing, ant-colony optimization, and genetic algorithms for self-structuring antennas," *IEEE Trans. Antennas Propag.*, vol. 52, no. 4, pp. 1007–1014, April 2004.

[108] Y. Rahmat-Samii and E. Michielssen, *Electromagnetic Optimization by Genetic Algorithms.* New York, NY, USA: John Wiley & Sons, Inc., 1999.

[109] J. Perruisseau-Carrier, F. Bongard, R. Golubovic-Niciforovic, R. Torres-Sanchez, and J. Mosig, "Contributions to the modeling and design of reconfigurable reflecting cells embedding discrete control elements," *IEEE Trans. Microw. Theory Tech.*, vol. 58, no. 6, pp. 1621 –1628, june 2010.

[110] *Synthetic Quartz Glass Substrates*, Shin-Etsu Chemical Co., 6-1 Ohtemachi 2-chome, Chiyoda-ku, Tokyo, Japan.

[111] N. Biyikli, Y. Damgaci, and B. Cetiner, "Low-voltage small-size double-arm MEMS actuator," *Electronics Letters*, vol. 45, no. 7, pp. 354–356, 26 2009.

[112] J. Heikenfeld *et al.*, "Electrofluidic displays using young–laplace transposition of brilliant pigment dispersions," *Nature Photonics*, vol. 3, no. 5, pp. 292–296, 2009.

[113] J. Lee and C.-J. Kim, "Surface-tension-driven microactuation based on continuous electrowetting," *J. Microelectromech. Syst.*, vol. 9, no. 2, pp. 171–180, 2000.

[114] Z. Wan, H. Zeng, and A. Feinerman, "Reversible electrowetting of liquid-metal droplet," *J. Fluids Eng.*, vol. 129, no. 4, pp. 388–394, 2007.

[115] G. H. Huff, D. L. Rolando, P. Walters, and J. McDonald, "A frequency reconfigurable dielectric resonator antenna using colloidal dispersions," *IEEE Antennas Wireless Propag. Lett.*, vol. 9, pp. 288–290, 2010.

[116] S. A. Long and G. H. Huff, "A substrate integrated fluidic compensation mechanism for deformable antennas," in *Proc. NASA/ESA Conf. Adaptive Hardware and Systems AHS 2009*, 2009, pp. 247–251.

[117] J.-H. So, J. Thelen, A. Qusba, G. J. Hayes, G. Lazzi, and M. D. Dickey, "Reversibly deformable and mechanically tunable fluidic antennas," *Adv. Funct. Mater.*, vol. 19, no. 22, pp. 3632–3637, 2009.

[118] M. Li, B. Yu, and N. Behdad, "Liquid-tunable frequency selective surfaces," *IEEE Microw. Wireless Compon. Lett.*, vol. 20, no. 8, pp. 423–425, 2010.

[119] K. J. Morton, K. Loutherback, D. W. Inglis, O. K. Tsui, J. C. Sturm, S. Y. Chou, and R. H. Austin, "Hydrodynamic metamaterials: microfabricated arrays to steer, refract, and focus streams of biomaterials," *Proc. Natl. Acad. Sci. U. S. A.*, vol. 105, no. 21, pp. 7434–8, May 2008.

[120] T. S. Kasirga, Y. N. Ertas, and M. Bayindir, "Microfluidics for reconfigurable electromagnetic metamaterials," *Appl. Physics Lett.*, vol. 95, no. 21, p. 214102, 2009.

[121] A. Alford and A. G. Kandoian, "Ultrahigh-frequency loop antennas," *Trans. of the Amer. Institute of Elect. Engineers*, vol. 59, no. 12, pp. 843–848, 1940.

[122] C.-C. Lin, L.-C. Kuo, and H.-R. Chuang, "A horizontally polarized omnidirectional printed antenna for WLAN applications," *IEEE Trans. Antennas Propag.*, vol. 54, no. 11, pp. 3551–3556, 2006.

[123] N. J. McEwan, R. A. Abd-Alhameed, E. M. Ibrahim, P. S. Excell, and J. G. Gardiner, "A new design of horizontally polarized and dual-polarized uniplanar conical beam antennas for HIPERLAN," *IEEE Trans. Antennas Propag.*, vol. 51, no. 2, pp. 229–237, 2003.

[124] B. Q. Wu and K.-M. Luk, "A wideband, low-profile, conical-beam antenna with horizontal polarization for indoor wireless communications," *IEEE Antennas Wireless Propag. Lett.*, vol. 8, pp. 634–636, 2009.

[125] E. Verpoorte and N. F. De Rooij, "Microfluidics meets MEMS," *Proc. IEEE*, vol. 91, no. 6, pp. 930–953, 2003.

[126] J. M. Bustillo, R. T. Howe, and R. S. Muller, "Surface micromachining for microelectromechanical systems," *Proc. IEEE*, vol. 86, no. 8, pp. 1552–1574, 1998.

[127] K. V. Puglia, "Electromagnetic simulation of some common balun structures," *IEEE Microw. Mag.*, vol. 3, no. 3, pp. 56–61, 2002.

[128] M. Gans, D. Kajfez, and V. H. Rumsey, "Frequency independent baluns," *Proc. IEEE*, vol. 53, no. 6, pp. 647–648, 1965.

[129] R. E. Collin, "The optimum tapered transmission line matching section," *Proceedings of the IRE*, vol. 44, no. 4, pp. 539–548, 1956.

[130] A. R. V. Hippel, *Dielectric Materials and Applications*. Technology Press of M.I.T. And John Wiley & Sons, New York, 1954.

[131] S. K. Cho, H. Moon, and C.-J. Kim, "Creating, transporting, cutting, and merging liquid droplets by electrowetting-based actuation for digital microfluidic circuits," *J. Microelectromech. Syst.*, vol. 12, no. 1, pp. 70–80, 2003.

[132] J. G. Andrews, "Interference cancellation for cellular systems: a contemporary overview," *IEEE Wireless Commun. Mag.*, vol. 12, no. 2, pp. 19–29, 2005.

[133] R. L. Riegler and J. Compton, R. T., "An adaptive array for interference rejection," *Proc. IEEE*, vol. 61, no. 6, pp. 748–758, 1973.

[134] *BAP64-02 Silicon PIN Diode*, NXP Semiconductors, January 2008, rev. 06.

[135] H. Wheeler, "The radiansphere around a small antenna," *Proceedings of the IRE*, vol. 47, no. 8, pp. 1325–1331, aug. 1959.

[136] F. Croq and D. Pozar, "Millimeter-wave design of wide-band aperture-coupled stacked microstrip antennas," *IEEE Trans. Antennas Propag.*, vol. 39, no. 12, pp. 1770–1776, dec 1991.

[137] R. Garg, "Broadbanding of microstrip antennas," in *Microstrip Antenna Design Handbook*. Artech House, 2001, pp. 533–590.

[138] T. Taga, "Analysis for mean effective gain of mobile antennas in land mobile radio environments," *IEEE Trans. Veh. Technol.*, vol. 39, no. 2, pp. 117–131, 1990.

[139] A. Glazunov, A. Molisch, and F. Tufvesson, "Mean effective gain of antennas in a wireless channel," *Microwaves, Antennas & Propagation, IET*, vol. 3, no. 2, pp. 214–227, 2009.

[140] J. Li and R. Compton Jr, "Angle and polarization estimation using ESPRIT with a polarization sensitive array," *IEEE Trans. Antennas Propag.*, vol. 39, no. 9, pp. 1376–1383, 1991.

[141] W. A. Imbriale, "Earth station antennas," in *Antenna Engineering Handbook*, 4th ed., J. L. Volakis, Ed.   McGraw-Hill, 2007.

[142] W. Lee, J. Kim, C. S. Cho, and Y. J. Yoon, "Beamforming lens antenna on a high resistivity silicon wafer for 60 GHz WPAN," *IEEE Trans. Antennas Propag.*, vol. 58, no. 3, pp. 706–713, 2010.

[143] J. D. Kraus, *Antennas*, 2nd ed.   McGraw-Hill, 1988.

[144] D. Rodrigo, L. Jofre, and B. A. Cetiner, "Circular beam-steering reconfigurable antenna with liquid metal parasitics," *IEEE Trans. Antennas Propag.*, vol. 60, no. 4, pp. 1796 – 1802, april 2012.

[145] H. Eslami, C. P. Sukumar, D. Rodrigo, S. Mopidevi, A. M. Eltawil, L. Jofre, and B. A. Cetiner, "Reduced overhead training for multi reconfigurable antennas with beam-tilting capability," *IEEE Trans. Wireless Commun.*, vol. 9, no. 12, pp. 3810–3821, 2010.

[146] J. Kenney and E. Keeping, *Mathematics of Statistics*, 2nd ed.   Princeton, NJ: Van Nostrand, 1951, ch. The Distribution of the Standard Deviation, pp. 170–173.

AUTHOR PUBLICATIONS

JOURNALS ARTICLES

[JA1] **D. Rodrigo**, B. A. Cetiner, and L. Jofre, "Frequency, radiation pattern and polarization reconfigurable antenna using a parasitic pixel layer," *IEEE Trans. Antennas Propag.*, submitted.

[JA2] **D. Rodrigo**, L. Jofre, and J. Perruisseau-Carrier, "Unit cell for frequency-tunable beamscanning reflectarrays," *IEEE Trans. Antennas Propag.*, submitted.

[JA3] **D. Rodrigo**, J. Romeu, S. Capdevila, and L. Jofre, "A figure-of-merit for pattern reconfigurable antennas," *IEEE Trans. Antennas Propag.*, vol. 61, no. 3, pp. 1448–1453, 2013.

[JA4] B. Cetiner, Z. Li, **D. Rodrigo**, and L. Jofre, "A new class of antenna array with a reconfigurable element factor," *IEEE Trans. Antennas Propag.*, 2013, in press.

[JA5] A. Zohur, H. Mopidevi, **D. Rodrigo**, M. Unlu, L. Jofre, and B. Cetiner, "RF MEMS reconfigurable two-band antenna," *IEEE Antennas Wireless Propag. Lett.*, vol. 12, pp. 72–75, 2013.

[JA6] **D. Rodrigo**, L. Jofre, and B. A. Cetiner, "Circular beam-steering reconfigurable antenna with liquid metal parasitics," *IEEE Trans. Antennas Propag.*, vol. 60, no. 4, pp. 1796 –1802, april 2012.

[JA7] **D. Rodrigo** and L. Jofre, "Frequency and radiation pattern reconfigurability of a multi-size pixel antenna," *IEEE Trans. Antennas Propag.*, vol. 60, no. 5, pp. 2219 –2225, may 2012.

[JA8] X. Yuan, Z. Li, **D. Rodrigo**, H. S. Mopidevi, O. Kaynar, L. Jofre, and B. A. Cetiner, "A parasitic layer-based reconfigurable antenna design by multi-objective optimization," *IEEE Trans. Antennas Propag.*, vol. 60, no. 6, pp. 2690–2701, june 2012.

[JA9] H. Mopidevi, **D. Rodrigo**, O. Kaynar, L. Jofre, and B. A. Cetiner, "Compact and broadband antenna for LTE and public safety applications," *IEEE Antennas Wireless Propag. Lett.*, vol. 10, pp. 1224–1227, 2011.

[JA10] H. Eslami, C. P. Sukumar, **D. Rodrigo**, S. Mopidevi, A. M. Eltawil, L. Jofre, and B. A. Cetiner, "Reduced overhead training for multi reconfigurable antennas with beam-tilting capability," *IEEE Trans. Wireless Commun.*, vol. 9, no. 12, pp. 3810–3821, 2010.

CONFERENCE ARTICLES

[CA1] **D. Rodrigo**, E. Diaz, J. Romeu, and L. Jofre, "Frequency-agile on-channel repeater using a reconfigurable pixel layer," in *Proc. Seventh European Conf. Antennas and Propagation (EuCAP)*, 2013, pp. 1–4.

[CA2] **D. Rodrigo**, L. Jofre, and J. Perruisseau-Carrier, "A frequency reconfigurable cell for beam-scanning reflectarrays," in *Proc. IEEE Antennas and Propagation Society Int. Symp. (APSURSI)*, 2013, pp. 1–4.

[CA3] E. Nova, **D. Rodrigo**, J. Romeu, and L. Jofre, "94 GHz cassegrain reflector antenna performance characterization," in *Proc. Sixth European Conf. Antennas and Propagation (EuCAP)*, march 2012, pp. 3442 –3445.

[CA4] **D. Rodrigo**, J. Romeu, and L. Jofre, "Interference rejection using frequency and pattern reconfigurable antennas," in *Proc. IEEE Antennas and Propagation Society Int. Symp. (APSURSI)*, july 2012, pp. 1 –2.

[CA5] **D. Rodrigo**, Y. Damgaci, M. Unlu, B. A. Cetiner, J. Romeu, and L. Jofre, "Antenna reconfigurability based on a novel parasitic pixel layer," in *Proc. Fifth European Conf. Antennas and Propagation (EuCAP)*, 2011, pp. 3497–3500.

[CA6] **D. Rodrigo**, L. Jofre, M. Unlu, Y. Damgaci, B. A. Cetiner, and J. Romeu, "Genetic reconfigurability of a multi-size pixelled antenna," in *Proc. IEEE Int Wireless Information Technology and Systems (ICWITS) Conf*, 2010, pp. 1–4.

[CA7] A. Khoshniat, H. Mopidevi, Y. Damgaci, **Rodrigo, D.**, L. Jofre, and B. A. Cetiner, "MEMS integrated reconfigurable antenna for cognitive public safety radios," in *Proc. Fourth European Conf. Antennas and Propagation (EuCAP)*, 2010, pp. 1–3.

[CA8] **D. Rodrigo** and L. Jofre, "MEMS-reconfigurable antenna based on a multi-size pixelled geometry," in *Proc. Fourth European Conf. Antennas and Propagation (EuCAP)*, 2010, pp. 1–4.

[CA9] **D. Rodrigo**, Y. Damgaci, M. Unlu, L. Jofre, and B. A. Cetiner, "Small pixelled antenna with MEMS-reconfigurable radiation pattern," in *Proc. IEEE Antennas and Propagation Society Int. Symp. (APSURSI)*, 2010, pp. 1–4.

[CA10] **D. Rodrigo**, Y. Damgaci, N. Biyikli, B. A. Cetiner, J. Romeu, and L. Jofre, "Genetic impedance and radiation reconfigurability of a NEMS bi-clustered pixelled antenna," in *RF MEMS and RF Microsystems, 2009. The 10th International Symposium on*, July 2009, pp. 139–142.

BOOK CHAPTERS

[BA1] **D. Rodrigo**, L. Jofre, and J. Romeu, *Handbook of RF-MEMS for wireless and mobile applications.* Woodhead Publishing Ltd., 2013, ch. RF-MEMS antennas for wireless applications.

PATENTS

[PA1] "Broadband antenna systems and methods," US Patent 61/558,976, 2011.

[PA2] "Reconfigurable antennas utilizing liquid metal elements," US Patent 61/568,041, 2011.

[PA3] "Reconfigurable antennas utilizing a parasitic layer," US Patent 61/584,546, 2012.

ACRONYMS

ACO   Ant-Colony Optimization

CNF   Cornell Nanoscale Science and Technology Facilities

CPW   CoPlanar Waveguide

CR   Cognitive Radio

CST   Computer Simulation Technology

DC   Direct Current

DOA   Direction-Of-Arrival

DRA   Dielectric Resonator Antennas

EM   Electro-Magnetic

EWOD   Electro-Wetting on Dielectric

FDTD   Finite-Difference Time-Domain

FEM   Finite Element Method

FET   Field Effect Transistor

FoM   Figure of Merit

GA   Genetic Algorithm

GPS   Global Positioning System

GSM   Global System for Mobile Communications

HFSS   High Frequency Structure Simulator

IEEE   Institute of Electrical and Electronics Engineers

LHCP   Left-Hand Circular Polarization

LOS   Line-Of-Sight

MEMS   Micro Electro-Mechanical Systems

MoM   Method of Moments

PCB   Printed Circuit Board

PR   Photo-Resist

PSO   Particle Swarm Optimization

RA   Reconfigurable Antenna

RECAP   REConfigurable APerture

RF   Radio Frequency

RHCP	Right-Hand Circular Polarization
RW	Random Walk
SA	Simulated Annealing
SAR	Specific Absorption Rate
SEM	Scanning Electron Microscope
SIR	Signal-to-Interference Ratio
UMTS	Universal Mobile Telecommunications System
UPC	Universitat Politècnica de Catalunya
USU	Utah State University
VBS	Visual Basic Script
VNA	Vector Network Analyzer
WLAN	Wireless Local Area Network
WPAN	Wireless Personal Area Network